

MASS 57, 59 URCA COOLING IN SUPERBURSTING SYSTEMS

By

Kirby Hermansen

A DISSERTATION

Submitted to
Michigan State University
in partial fulfillment of the requirements
for the degree of

Ph.D. - Physics and Astronomy

2023

ABSTRACT

Current astrophysical models cannot explain the observations of anomalous extended X-ray bursts—called “superbursts”. An as yet unknown heat source was postulated as the mechanism driving these superbursts in the outer layers of the crusts of neutron stars in these X-ray transients. Urca cooling—a nuclear process by which repeated electron capture and β^- -decay removes energy from the system in the form of neutrinos—may occur in the outer crust as well and further exacerbates the problem by removing heat deposited by any new heating mechanism..

Estimates of the ground state to ground state β -decay transition strengths that determine the Urca cooling strength rely heavily on theoretical QRPA predictions for nuclei far from stability which have little to no experimental data available. Moreover, the limited existing experimental data are susceptible to the Pandemonium effect due to the large Q -values of the nuclei and the limited energies of the proposed level schemes.

This work seeks to experimentally determine the ground state to ground state transition strength for the β -decay parents of three prominent Urca coolers in superbursting systems: ^{57}Ti , ^{57}Sc , and ^{59}Ti . Nuclei were produced by projectile fragmentation and implanted into a detector system at the National Superconducting Cyclotron Laboratory (NSCL). Transition strengths were determined from the detected β -delayed γ -ray emission using the total absorption spectrometer SuN and the β -delayed neutron emission using the neutron long counter NERO. The determined ground state to ground state transition strength of 3(2)% ($\log ft = 5.88(18)$) for the ^{57}Ti β -decay to ^{57}V is far below the previous experimental estimate of 54(3)% from an experiment using high-resolution HPGe detectors. The ground state to ground state transition strengths for the β -decays of ^{57}Sc and ^{59}Ti are 1(1)% ($\log ft = 6.02(89)$) and 3(2)% ($\log ft = 5.80(39)$), respectively—well below the QRPA pre-

dicted transition strengths, corresponding to $\log ft$ values of 4.9 and 4.9. The new results lead to drastically reduced Urca cooling from these pairs, reducing the total cooling of each by 74%, 88%, and 82% respectively. The results also provide new nuclear structure information for nuclei very far from stability, with expanded level schemes for ^{57}V and ^{57}Ti , and the first proposed level scheme for ^{59}V .

Copyright by
KIRBY HERMANSEN
2023

TABLE OF CONTENTS

LIST OF TABLES	vi
LIST OF FIGURES	viii
Chapter 1 Background and Introduction	1
1.1 Astrophysics Motivation	1
1.2 Nuclear Physics Background	5
1.3 Goal of This Work	14
1.4 Experimental Approach	14
1.5 Overview of Thesis	17
Chapter 2 Experimental Methods	19
2.1 Experimental Overview	20
2.2 Detector Setup	23
2.3 Electronics Setup	31
Chapter 3 Simulation Methods	39
3.1 GEANT4 Simulations	39
3.2 RAINIER Simulations	45
3.3 Methods for Estimating Feeding Uncertainty	49
Chapter 4 Data Analysis	52
4.1 Calibrations	52
4.2 Particle Identification	65
4.3 Correlations	66
4.4 P_n Calculation	75
4.5 Daughter Feeding	79
Chapter 5 Results	82
5.1 P_n Values	82
5.2 Decay Curves	83
5.3 Gamma Analysis	87
Chapter 6 Discussion	115
6.1 Nuclear Physics	115
6.2 Nuclear Astrophysics	119
Chapter 7 Conclusion	122
BIBLIOGRAPHY	124

LIST OF TABLES

Table 1.1: Table showing the selection rules which define the “allowedness” of a given β -decay.	12
Table 2.1: Table showing the DDAS filter settings for the BCS detectors. Note that the thresholds varied widely by channel, thus an approximate value is shown here.	35
Table 2.2: Table showing the DDAS filter settings for the NERO detectors. The thresholds varied widely by tube, thus an approximate value is shown here.	36
Table 2.3: Table showing the DDAS filter settings for the SuN detectors. Note that the thresholds vary widely by channel, thus an approximate value is shown here.	37
Table 4.1: Table showing the original isotopic composition of the ^{252}Cf source, along with the 2014 calculated composition based on the activity, and finally the extrapolated composition on the day of the calibration for this experiment. Table updated from [1].	60
Table 4.2: Table showing the observed source, background, and background subtracted source neutron rates, and the overall efficiency calculated using the extrapolated ^{252}Cf neutron activity from Tab. 4.1	60
Table 4.3: Table showing the total implants and correlated decays for the isotopes of interest. The correlator for ^{57}Sc , ^{60}Ti and ^{62}V for the SuN portion used a 3×3 spatial window, which accounts for the significantly increased relative number of correlated decays to implants over the other isotopes that used a 1×1 window.	73
Table 5.1: Table showing the observed β decay and β -n decay events for both forward- and reverse-time correlated events, as well as the determined P_n value for the isotopes studied. Additionally, for the isotopes with a determined $P_n > 6\%$, the neutron-gated decay curve half-life is shown. Upper limits are given at a confidence level of 95%.	83

Table 5.2:	Table showing previously measured half-lives, in comparison with the half-lives determined during the BCS and SuN portions of the experiment. Also shown are the total parent particles observed, estimated by integrating the fit decay curve from the half-life. ^{56}Sc was determined in [2] to beta decay from the ground state as well as a high-spin isomeric state to ^{56}Ti . Thus two half-lives were measured in [2, 3]. Here, the two states were fit to a single half-life. As the resolution of SuN was insufficient to distinguish the different ~ 1150 keV γ -rays.	86
Table 5.3:	Table showing previously measured half-lives used for fitting daughter and granddaughter decay curves.	86
Table 5.4:	Table showing the previously and currently measured intensities, along with $\log ft$ values, to the various energy levels in the decay of ^{57}Ti to ^{57}V	92
Table 5.5:	Table showing the previously and currently measured intensities of individual γ -rays in the decay of ^{57}Ti to ^{57}V	96
Table 5.6:	Table showing the currently measured intensities, along with $\log ft$ values, to the various energy levels in the decay of ^{57}Sc to ^{57}Ti . $\log ft$ values are calculated by reweighting the intensities to only include transitions to the β -daughter.	105
Table 5.7:	Table showing the previously and currently measured intensities of individual γ -rays in the decay of ^{57}Ti to ^{57}V	106
Table 5.8:	Table showing the currently measured intensities, along with $\log ft$ values, to the various energy levels in the decay of ^{59}Ti to ^{59}V	112
Table 5.9:	Table showing the previously and currently measured intensities of individual γ -rays in the decay of ^{59}Ti to ^{59}V	113

LIST OF FIGURES

Figure 1.1:	Effect of a nonzero temperature on the allowed electron phase space in the Fermi gas surrounding the nuclei of the neutron star crust. Particularly note the region of coexisting species of nuclei where Urca cooling can exist, in contrast to the sharp boundary in the zero temperature limit [1].	7
Figure 1.2:	State of ground state spins and ground state to ground state transitions for $A = 57, 59$ mass chains. These run from the neutron-rich nuclei expected to contribute to Urca cooling back to stability.	15
Figure 1.3:	Comparison of theoretical, ideal γ -ray spectra from a high-purity Ge detector and a high-efficiency TAS detector, for a hypothetical decay involving feeding to two individual states, reproduced from [4]. Since all decays to the second excited state involve emission of both γ_1 and γ_2 , the TAS shows a peak at the summed $E_{\gamma_1} + E_{\gamma_2}$. Therefore the TAS spectrum shows directly the feeding intensity of the excited states in the daughter nucleus while the Ge spectrum would rely on coincidence data to correctly identify that γ_1 results from only feeding to the summed energy level. In reality, where the TAS summing is not 100%, an additional, smaller peak at E_{γ_1} would exist for incompletely summed decays.	18
Figure 2.1:	Schematic of the CCF and A1900 at the NSCL, figure reproduced from [5]. Particularly of note is the wedge degrader at Image 2, which was used to further separate beam components by momentum. Immediately downstream of the degrader is a scintillator (not pictured) with two photomultiplier tubes used as a time-of-flight trigger for particle identification [5, 6].	21
Figure 2.2:	Schematic of the wedge-shaped energy degrader in the A1900 separator [5, 6] at the Image 2 position. Also seen here is the scintillator, which acted as the stop gate on the time-of-flight calculation for particle identification. Figure reproduced from [5].	21
Figure 2.3:	LISE ⁺⁺ simulated yield vs. X at Image 1 (top) and at the focal plane (bottom) in the A1900. The dashed black lines indicate the slits selecting on X position at Image 1 (± 100 mm), and at the focal plane (± 5 mm). Only the particles of interest and the sample contaminant ^{46}Ar are shown.	22
Figure 2.4:	A schematic of the BCS inside the NERO array. Note that NERO is arranged such that the BCS DSSD is at the center of the NERO detectors to maximize neutron detection efficiency. Figure reproduced from [7].	26

Figure 2.5:	Neutron moderation time in the NERO matrix reproduced from [7]. The inner (red squares), middle (blue triangles) and outer (pink empty circles) ring moderation times are shown, as well as the combined total for the detector (black filled circles).	27
Figure 2.6:	Schematics of the SuN detector as a whole (Fig.2.6a) as well as a cross section showing the direction of the incoming beam (Fig.2.6b). Note that the SuN DSSD is positioned halfway through the length of the detector, and stopped the beam there. Figures reproduced from [8].	29
Figure 2.7:	Overlaid comparison of the two main spectra observed by SuN in the ^{60}Co decay: the sum of individual segments (red), and the total absorption (blue). Visible are the two separate individual γ -ray peaks in the sum of segments, as well as the clear sum peak in the total absorption. Inset is the multiplicity distribution, from 1 to 5 distinct segments.	30
Figure 2.8:	Same as Fig. 2.7 but now only including events with an exact multiplicity of two segments. The inset multiplicity distribution demonstrates this cut.	31
Figure 2.9:	DDAS filter settings for signal processing in the Pixie-16 modules, figure reproduced from [9]. (a) shows the raw preamplified signal from the detector; (b) shows the digital constant fraction discriminator (CFD) and trigger-filter response to the signal in (a); and (c) shows the energy filter algorithm response.	33
Figure 3.1:	Histograms of the SuN TAS and SS for an observed (blue) and simulated (red) ^{60}Co source. All are filtered to only include events with multiplicity ≥ 2	41
Figure 3.2:	Generic example of the increase in the nuclear level density from discrete states (roughly 0 – 1.5 MeV) to a quasi-continuum (roughly > 1.5 MeV). Figure is reproduced from [10].	43
Figure 3.3:	Background- and daughter-subtracted TAS for ^{57}Ti correlated decays. Red lines indicate the gates applied to select the level at 2036 keV. The black dashed line shows the cutoff, $E_{\text{crit}} = 2550$ keV, at which the discrete level region ends and the quasi-continuum begins.	45
Figure 3.4:	Proposed ^{57}V level scheme from [11] for the β decay of ^{57}Ti to ^{57}V	46
Figure 3.5:	Templates showing the three potential different γ -ray cascade paths from the 2036 keV level to the ground state of ^{57}V	47

Figure 3.6:	Background- and daughter-subtracted SS and multiplicity for ^{57}Ti correlated decays, gated on the 2036 keV level in the TAS. The fit of the composing γ -ray cascades from the level is shown in orange.	48
Figure 3.7:	Comparative distributions of fit intensities of the MOEA/D-DE (blue) and Monte Carlo (orange) error estimations for the decay of ^{57}Ti . The vertical dashed red lines give the lower and upper bounds of the feeding uncertainty for a given level. The vertical solid red line gives the feeding intensity which minimizes the summed χ^2 obtained from the fit. The blue dashed curve is the Gaussian fit to the MOEA/D-DE distribution, and the orange dashed curve is the fit to the Monte Carlo distribution. . . .	51
Figure 4.1:	Spectra of a sample strip from the ^{241}Am and ^{90}Sr joint source run. Visible is the noise peak below the threshold (red line) at ~ 1950 ADC units which transitions into the ^{90}Sr electron β -decay spectrum. The ^{241}Am α -decay at ~ 20000 ADC units is used to gain-match the energies of each SSSD strip.	53
Figure 4.2:	Energy spectrum for a sample strip from the ^{228}Th calibration run. Note that the gain from the preamplifier was such that the higher-energy α particle at 8.785 MeV was not visible.	54
Figure 4.3:	Residuals of the linear fit of the back side strips of the BCS DSSD to the calibration α particles from ^{228}Th decay. Note that the gain from the preamplifier was such that none of the spectra included the higher-energy α particle at 8.785 MeV.	55
Figure 4.4:	Residuals of the linear fit of the front side strips of the BCS DSSD to the calibration α particles from ^{228}Th decay. Note that the resolutions of the first nine strips were insufficient to distinguish the two lowest energy α particles at 5.423 and 5.685 MeV, and so only the higher energy particles were incorporated to the fit. As in Fig. 4.3, the gain for several of the strips was such that the higher-energy α particle at 8.785 MeV was not included and was thus not included in the fit.	56
Figure 4.5:	Energy spectrum for a sample strip from the ^{90}Sr calibration run. The software threshold for the sample strip is shown by the red line.	57
Figure 4.6:	Energy spectrum for the BCS scintillator light-particle veto for the entire BCS portion of the beam time. The software threshold for the sample strip is shown by the red line. A decay event requires that the signal in the scintillator is < 3650 ADC units or else is rejected as a light-particle event. Note that this spectrum only shows non-zero scintillator signals.	58

Figure 4.7: Sample spectra for the NERO neutron counting tubes. Fig. 4.7a shows a ^3He counter and Fig. 4.7b shows a BF_3 counter. Visible in both spectra is the low energy noise peak, along with the designated upper and lower limits (red vertical lines) of a neutron signal for these tubes. Only signals within the red bounds were considered neutron events, and the bounds are set for each tube individually.	61
Figure 4.8: Histograms of the individual PMTs in SuN for a background run. A vertical line is drawn through the ^{40}K γ -ray peak—around 1100 ADC units—to which all of the PMTs are gain matched.	62
Figure 4.9: Residuals of the linear fit of the eight SuN segments to the calibration γ -rays from ^{241}Am , ^{137}Cs , and ^{60}Co	63
Figure 4.10: Residuals of the post-experiment calibration using the pre-experiment linear fit of the eight SuN segments to the calibration γ -rays from ^{241}Am , ^{137}Cs and ^{60}Co	63
Figure 4.11: Residuals of the linear calibration of the SuN DSSD strips to the ^{228}Th source data.	64
Figure 4.12: Energy spectrum for a sample strip from the ^{228}Th calibration run.	65
Figure 4.13: Particle ID (δE -TOF) plots for the BCS-NERO portion. Left shows all the beam particles that passed through the upstream PINs, right is the same but cut to only the particles successfully implanted in the DSSD.	66
Figure 4.14: Particle ID (δE -TOF) plots for the BCS-NERO portion, cut on isotopes of interest. From left to right, top to bottom: ^{62}V , ^{61}V , ^{60}V , ^{59}V , ^{60}Ti , ^{59}Ti , ^{58}Ti , ^{57}Ti , ^{57}Sc , ^{56}Sc , ^{55}Sc	67
Figure 4.15: Particle ID (δE -TOF) plots for the SuN portion. Left shows all the beam particles that passed through the upstream PINs, right is the same but cut to only the particles successfully implanted in the DSSD. The visible “shadow” between some isotopes is due to trigger thresholds in the I2 scintillator. Particle cuts are applied in order to reduce the contribution from these events.	68
Figure 4.16: Particle ID (δE -TOF) plots for the SuN portion, cut on isotopes of interest. From left to right, top to bottom: ^{62}V , ^{61}V , ^{60}V , ^{59}V , ^{60}Ti , ^{59}Ti , ^{58}Ti , ^{57}Ti , ^{57}Sc , ^{56}Sc , ^{55}Sc	69
Figure 4.17: Decay time plot including parent, background, and all daughter decay curves from ^{57}Ti correlated decays. Neutron-daughter decays are not included here as the P_n was determined to be negligible.	76

Figure 4.18: Neutron-gated decay time plot for ^{61}V . Only the parent and a flat background is included in this fit.	77
Figure 4.19: Comparison of time between implant and decay for forward and reverse correlated decays for ^{57}Sc decays in the SuN portion.	79
Figure 5.1: Neutron-gated decay curves for the (a) ^{57}Sc , (b) ^{60}V , (c) ^{61}V , and (d) ^{62}V isotopes.	84
Figure 5.2: Decay curves for the ^{56}Sc isotopes for both the BCS-NERO (left) and SuN (right) portions. Legends are identical for both.	85
Figure 5.3: Decay curves for the ^{57}Sc isotopes for both the BCS-NERO (left) and SuN (right) portions. Legends are identical for both.	85
Figure 5.4: Decay curves for the ^{57}Ti isotopes for both the BCS-NERO (left) and SuN (right) portions. Legends are identical for both. In this 500 ms window, only the parent ^{57}Ti and daughter ^{57}V decays appear in appreciable amounts.	87
Figure 5.5: Decay curves for the ^{58}Ti isotopes for both the BCS-NERO (left) and SuN (right) portions. Legends are identical for both.	87
Figure 5.6: Decay curves for the ^{59}Ti isotopes for both the BCS-NERO (left) and SuN (right) portions. Legends are identical for both.	88
Figure 5.7: Decay curves for the ^{60}Ti isotopes for both the BCS-NERO (left) and SuN (right) portions. Legends are identical for both.	88
Figure 5.8: Decay curves for the ^{59}V isotopes for both the BCS-NERO (left) and SuN (right) portions. Legends are identical for both.	89
Figure 5.9: Decay curves for the ^{60}V isotopes for both the BCS-NERO (left) and SuN (right) portions. Legends are identical for both.	89
Figure 5.10: Decay curves for the ^{61}V isotopes for both the BCS-NERO (left) and SuN (right) portions. Legends are identical for both.	90
Figure 5.11: Decay curves for the ^{62}V isotopes for both the BCS-NERO (left) and SuN (right) portions. Legends are identical for both.	90
Figure 5.12: Raw, forward-correlated TAS (blue) and reverse-correlated background TAS (red) for the ^{57}Ti decay. Both are cut to only include decays in the first 3.00×10^2 ms after implantation.	92

Figure 5.13: Background-subtracted TAS for $t < 3.00 \times 10^2$ ms after implantation (blue) and the region $600 < t < 1.200 \times 10^3$ ms (red) for the ^{57}Ti decay. Note the two levels at 2.68×10^2 keV and 6.92×10^2 keV which are due to the β -daughter decay of ^{57}V	93
Figure 5.14: Final, background- and daughter-subtracted TAS for the ^{57}Ti decay. Note the two levels from ^{57}V are now removed. Closed triangles show the previously proposed levels [11], while the open triangles indicate proposed levels from this work.	93
Figure 5.15: Background-subtracted SS for $t < 3.00 \times 10^2$ ms after implantation (blue) and the region $600 < t < 1.200 \times 10^3$ ms (red) for the ^{57}Ti decay. Note the two γ -rays at 2.68×10^2 keV and 6.92×10^2 keV which are due to the β -daughter decay of ^{57}V	94
Figure 5.16: Final, background- and daughter-subtracted SS for the ^{57}Ti decay. Note the two levels from ^{57}V are now removed. Closed triangles show the previously identified γ -rays [11], while the open triangles indicate proposed levels from this work. The peak at 5.11×10^2 keV is due to electron pair production.	94
Figure 5.17: Revised ^{57}V level scheme for the β decay of ^{57}Ti to ^{57}V	95
Figure 5.18: TAS for the ^{57}Ti decay.	95
Figure 5.19: SS for the ^{57}Ti decay, the multiplicity fit is inset	96
Figure 5.20: Log-scaled SS for the ^{57}Ti decay, including higher energy γ -rays	97
Figure 5.21: Results of the MOEA/D algorithm fit of the templates to the observed spectra (blue histogram) overlaid with the results of the Monte Carlo variation on the observed spectra (green histogram) for the β decay of ^{57}Ti to ^{57}V . Only the seven identified discrete levels are shown, with the summed feedings to the quasi-continuum levels shown in the eighth panel. The solid red line indicates the intensity given by the composite fit, and the dashed red lines indicate the upper and lower bounds for each template using the combined MOEA/D and Monte Carlo error estimation.	98
Figure 5.22: ^{57}Ti level scheme for the β decay of ^{57}Sc to ^{57}Ti	101
Figure 5.23: Reverse-time background subtracted TAS of the correlated decays within the first 100 ms following ^{57}Sc implants (blue), with the reverse-time background subtracted and scaled TAS of the correlated decays within the first 10 ms following ^{57}Ti implants (red).	102

Figure 5.24: Final, background- and daughter-subtracted TAS for the ^{57}Sc decay. Closed triangles show the previously proposed levels [3], while the open triangles indicate proposed levels from this work.	102
Figure 5.25: Reverse-time background subtracted SS of the correlated decays within the first 100 ms following ^{57}Sc implants (blue), with the reverse-time background subtracted and scaled SS of the correlated decays within the first 10 ms following ^{57}Ti implants (red).	103
Figure 5.26: Final, background- and daughter-subtracted SS for the ^{57}Sc decay. Closed triangles show the previously identified γ -rays [3], while the open triangles indicate proposed γ -rays from this work.	103
Figure 5.27: TAS for the ^{57}Sc decay	104
Figure 5.28: SS for the ^{57}Sc decay, the multiplicity fit is inset	104
Figure 5.29: Log-scaled SS for the ^{57}Sc decay, including higher energy γ -rays	105
Figure 5.30: Results of the MOEA/D algorithm fit of the templates to the observed spectra (blue histogram) overlaid with the results of the Monte Carlo variation on the observed spectra (green histogram) for the β decay of ^{57}Sc to ^{57}Ti . Only the ten identified discrete levels are shown, with the summed feedings to the quasi-continuum levels shown in the eleventh panel. Four neutron-daughter feeding levels are also shown. The solid red line indicates the intensity given by the composite fit, and the dashed red lines indicate the upper and lower bounds for each template from the combined MOEA/D and Monte Carlo error estimation.	106
Figure 5.31: ^{59}V level scheme for the β decay of ^{59}Ti to ^{59}V	108
Figure 5.32: Reverse-time background subtracted TAS of the correlated decays within the first 1.20×10^2 ms following ^{59}Ti implants (blue), with the reverse-time background subtracted and scaled TAS of the correlated decays within the first 7 ms following ^{59}V implants (red).	109
Figure 5.33: Final, background- and daughter-subtracted TAS for the ^{59}Ti decay. Open triangles indicate proposed levels from this work.	110
Figure 5.34: Reverse-time background subtracted SS of the correlated decays within the first 1.20×10^2 ms following ^{59}Ti implants (blue), with the reverse-time background subtracted and scaled SS of the correlated decays within the first 7 ms following ^{59}V implants (red).	110

Figure 5.35: Final, background- and daughter-subtracted SS for the ^{59}Ti decay. Open triangles indicate proposed levels from this work. As with ^{57}Ti , the small peak at 5.11×10^2 keV is due to pair production in the detector from high-energy γ -rays. The peak around 2.10×10^2 keV is not labeled as no coincidences were established, nor is a specific TAS level clear. It is likely due to incomplete daughter subtraction.	111
Figure 5.36: TAS for the ^{59}Ti decay	111
Figure 5.37: SS for the ^{59}Ti decay, the multiplicity fit is inset	112
Figure 5.38: Log-scaled SS for the ^{59}Ti decay, including higher energy γ -rays	113
Figure 5.39: Results of the MOEA/D algorithm fit of the templates to the observed spectra (blue histogram) overlaid with the results of the Monte Carlo variation on the observed spectra (green histogram) for the β decay of ^{59}Ti to ^{59}V . Only the eight identified discrete levels are shown, with the summed feedings to the quasi-continuum levels shown in the ninth panel. Two neutron daughter levels are also included. The solid red line indicates the intensity given by the composite fit, and the dashed red lines indicate the upper and lower bounds for each template from the combined MOEA/D and Monte Carlo error estimation.	114
Figure 6.1: Comparison of QRPA predicted (dashed red) and experimentally observed (black, with gray shaded errors) $B(\text{GT})$ transition strengths for the decay of ^{57}Ti to ^{57}V . S_n of ^{57}V is at 6.33 MeV	116
Figure 6.2: Comparison of QRPA predicted (dashed red) and experimentally observed (black, with gray shaded errors) $B(\text{GT})$ transition strengths for the decay of ^{57}Sc to ^{57}Ti . S_n of ^{57}Ti is at 2.67 MeV	117
Figure 6.3: Comparison of QRPA predicted (dashed red) and experimentally observed (black, with gray shaded errors) $B(\text{GT})$ transition strengths for the decay of ^{59}Ti to ^{59}V . S_n of ^{57}V is at 5.55 MeV	118
Figure 6.4: Comparison of the estimated Urca luminosity by Urca β -parent. The red dashed line links the results from the previously predicted g.s.-to-g.s. intensities, to the results using the newly constrained values introduced here. The gray shaded region indicates the error bars on the updated values.	120

Figure 6.5: Comparison of the evolution of total energy during the simulation using the predicted (blue) and updated (orange) transition values. The vertical red dashed lines are to guide the eye to points in time where the various Urca coolers release energy. The lines are labeled by the β^- parent of the Urca pair. The impact of the change in ^{59}Ti cooling is overshadowed by the much larger ^{61}V cooling, which occurs simultaneously. 121

Chapter 1

Background and Introduction

1.1 Astrophysics Motivation

1.1.1 Neutron Stars

Neutron stars are dense astrophysical objects that result from the core-collapse supernova of a supergiant star. A massive star undergoes core-collapse when the nuclear fuel in its core has burnt to Fe and can no longer release energy through nuclear fusion. Once there is no longer any source of energy to counteract the gravitational pull towards the center of the star, the layers rapidly contract, until either the core collapses entirely into a black hole (for larger core masses), or the material of the core is compressed to nuclear densities, where neutron degeneracy pressure and repulsive nuclear forces are enough to stop the infalling material. The infall then bounces off the rigid core and radiates outward as an energetic shockwave, compressing and heating the envelope and ejecting it into space. The remnant of the core is a neutron star: a compact stellar object with a diameter on the order of 10 km and a typical mass between $1.4\text{--}2 M_{\odot}$.

A neutron star consists of several layers of different material, from the outer atmosphere down to the degenerate core. These layers are demarcated by their composition and densities. The thin, ultra-low density ($\rho \sim 10^{-4}\text{--}10^3 \text{ g cm}^{-3}$) atmosphere consists of “normal” gaseous or liquid atomic plasma. Below the atmosphere is the denser ($\rho \sim 10^3\text{--}10^6 \text{ g cm}^{-3}$) liquid

plasma of electrons and ionized nuclei of the neutron star ocean, and then the very dense, solid, and crystallized ($\rho \sim 10^6\text{--}10^{12} \text{ g cm}^{-3}$) lattices of electrons, neutron-rich nuclei and neutrons comprising the outer and inner crust [12]. Below the inner crust lies even more dense layers of matter, commonly called “nuclear pasta”, in the mantle of the neutron star. Finally, as densities reach and exceed nuclear density ($\rho \gtrsim 10^{14} \text{ g cm}^{-3}$) in the core of the neutron star, nuclei break down into free neutrons and protons, potentially forming exotic phases in the very center.

Due to these extreme characteristics, neutron stars make excellent laboratories for observing the behavior of dense matter, and mergers between neutron stars are one of the key theorized sites for the nucleosynthesis of many heavy elements via the r -process [13, 14] and as a source of gravitational waves [15].

1.1.2 Type I X-ray Bursts

Type I X-ray bursts are an astrophysical phenomena that takes place in a binary system consisting of a neutron star with a main sequence or giant companion star. As the companion star ages, the outer envelope of H and He expands outward and eventually overflows its Roche lobe, causing the material to become gravitationally bound to the neutron star, where it begins to infall and—due to its angular momentum—form an accretion disk. As the H and He accretes, it is compressed by the accreting material above it and forms a dense layer that begins to heat up. During this process, stable burning via the CNO cycle can occur, but once the temperature rises beyond $\sim 10^8 \text{ K}$ the accelerated reaction rates result in a thermonuclear runaway which burns away most of the accreted material within a few seconds [16]. This runaway powers a flash of X-ray emission from the heated neutron star photosphere that is visible to space-based X-ray telescopes, hence the name X-ray burst.

The runaway quickly burns through all the accreted material in a few seconds, exhausting its fuel source [16]. The burning stops, and the ashes of the burnt material are buried beneath the continually accreting H and He which continues to ignite in turn with a typical recurrence time of $\sim 1\text{--}10$ h [16]. Over time, as the buried material is compressed more and more, it is incorporated into and passes through the layers of the neutron star. As the surrounding layers become more neutron-rich, so too do the burnt ashes, forming heavy nuclei up to the neutron-drip line in the neutron star crust.

1.1.3 Quasi-Persistent Transients

For reasons that are not fully understood, low-mass X-ray binaries—systems consisting of a neutron star accreting matter from a low-mass companion—are known to alternate between extended periods with no accretion (quiescence) and active periods of X-ray activity (outbursts). The duration of these periods vary by system, with periodic outbursts sometimes lasting up to several years before entering quiescence. Systems whose quiescent phase lasts several years are known as “quasi-persistent transients”.

As outbursts continue, the original layers of the neutron star from its birth in a supernova are replaced with the ashes of the ongoing X-ray bursts. The infalling material compresses the burnt ashes beneath it, inducing nuclear reactions—including electron captures and pycnonuclear fusion—which heat the surrounding layer. Once a quasi-persistent transient enters quiescence, observations show the system cooling via thermal radiation and heat conduction toward the core [17]. Specifically for quasi-persistent transients, the long outburst period is comparable with the heat diffusion timescale of the crust layer and so the crust is heated over the course of the outburst [18]. In some cases electron captures can alternate with β -decays creating an Urca process that cools the crust and competes with the heat

sources to limit the temperature the crust can be heated to in an outburst [19].

During quiescence, observations provide insights into the physics of the neutron star layers: after the outer atmosphere and ocean cools, they become transparent to radiation from deeper in the neutron star, and the cooling from the crust becomes observable. Thus, longer quiescent phases allow observations to probe deeper into the neutron star. While heating stops when the transient enters quiescence, the Urca cooling can continue.

1.1.4 Superbursts

In 1999, a “remarkable” X-ray burst was observed from the low-mass X-ray binary 4U 1820-30 which challenged the known explanations and processes of X-ray burst physics [20]. This anomalous burst lasted ~ 3 h, more than 500 times the duration, and with an observed X-ray fluence ~ 1000 times more energetic than that of a He burst typical for this binary system [21]. Clearly, some modification to existing theory was necessary to account for this uncharacteristic “superburst”. The contemporaneous explanation was to ascribe the superburst to C burning in the C-rich ocean of the neutron star of the X-ray binary system. This explanation carried with it implications for the recurrence time of the burst based on the assumed conditions—notably the depth and temperature—of the ignition site. However, the recurrence time of superbursts is observed to be much shorter (0.3–2 yr [22]) than predicted. A proposed solution to this problem required the existence of additional heating sources in the neutron star crust.

Constraints on the location of this heat source have developed over time, as the presence of significant abundances of neutron-rich material of mass range $A = 50$ – 70 have been theorized to exist among the ashes of previous burning. Urca shell cooling can exist within this layer of material, which—depending on the relevant nuclear physics—can thermally isolate the crust

of the neutron star from all the inner regions [19]. This decoupling effectively constrains the location of the as yet unknown heat source driving the recurrence of the superbursts to layers within the crust or above. Thus, understanding the nuclear physics parameters which dictate the strength of this cooling is paramount to furthering the understanding of the innards of neutron stars, and the mechanisms driving the observed superburst phenomena.

1.2 Nuclear Physics Background

1.2.1 Nuclear Processes in Neutron Stars

As the density following a fluid element accreted onto a neutron star, after undergoing H, He, and possibly C burning in X-ray bursts, increases due to ongoing accretion and the electron gas surrounding the nuclei becomes degenerate, with the Fermi energy (ϵ_F) increasing at greater depth. The probability a given energy state (ϵ) has of being occupied by electrons is described by Fermi-Dirac statistics:

$$f(\epsilon) = \frac{1}{\exp((\epsilon - \epsilon_F)/k_B T) + 1} \quad (1.1)$$

where k_B is the Boltzmann constant, and T is the temperature. The increasing Fermi energy causes the highest energy electrons to be captured onto nuclei as their energy begins to exceed the negative electron capture Q -value (Q_{EC}) of the neutron-rich nuclei. This process proceeds with increasing depth and eventually the neutron drip line is reached, where electron capture proceeds into neutron unbound states and is then accompanied by neutron emission. As the density increases, so too does the Fermi energy, until it exceeds the Q_{EC} -value of the nucleus and the nucleus undergoes electron capture to a new nucleus (${}^A_{Z-1}Y$). This electron capture

proceeds as



and thus emits an electron neutrino in exchange for the captured electron. The emitted neutrino has a low probability of interacting with any of the matter in the neutron star, and likely carries its energy away from the system, thus marginally cooling the neutron star. Under the simplistic assumptions made here, the nuclear material can only progress in one direction: to more neutron-rich material. The inverse reaction, β^- -decay (Eq. 1.3) is Pauli-blocked as the phase space is completely occupied by the degenerate electron gas. This is because the electron capture occurs as soon as the Fermi energy reaches or exceeds the threshold.



However, if the zero temperature assumption is removed, the Fermi-Dirac distribution defining the Fermi level of the degenerate electron gas is now no longer a sharply defined step at the Fermi energy. Rather there is now an energy band phase space in which electrons can exist between the two defined states (Fig. 1.1). This band allows electrons to be captured from the high energy tail that exceed the electron capture threshold, and then re-emitted back into the electron gas via β^- -decay (hereafter simply β -decay unless specified) into the not fully occupied energy states just below the electron capture threshold. As both reactions are energetically possible and have open phase space, they occur in a cycle:

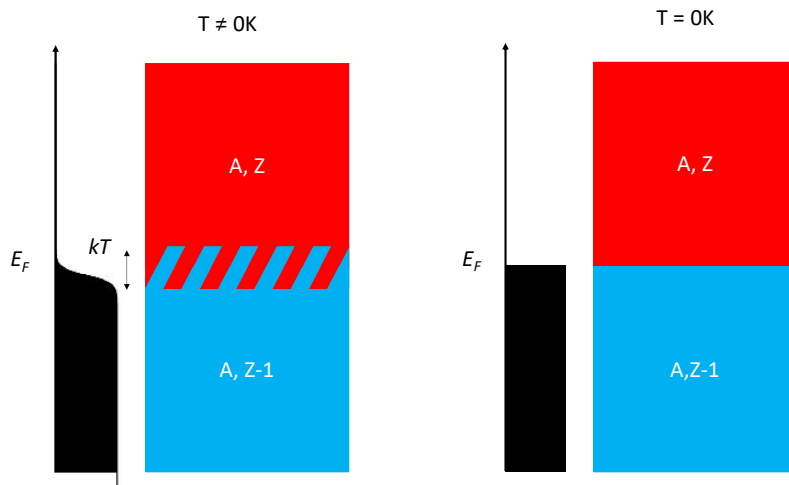


Figure 1.1: Effect of a nonzero temperature on the allowed electron phase space in the Fermi gas surrounding the nuclei of the neutron star crust. Particularly note the region of coexisting species of nuclei where Urca cooling can exist, in contrast to the sharp boundary in the zero temperature limit [1].



This cycle is known as the nuclear Urca¹ process, and results in the emission of two neutrinos per cycle, and can recycle many times over on the same nucleus. This results in significant cooling in certain narrow layers in neutron star crusts, where the electron Fermi energy is near an electron capture threshold.

Notably, the band of allowed electron energies emitted in β -decay is dependent on the

¹UnRecordable Cooling Agent, named for the Cassino da Urca in Rio de Janeiro, Brazil, where George Gamow and Mário Schenberg coined the term.

temperature of the region. A higher temperature will allow a larger range of electron energies, and thus more cooling in a wider layer as a result. The temperature dependence of Urca cooling is known to scale as T^5 , with the total luminosity of Urca cooling approximated as

$$L_\nu \approx L_{34} \times 10^{34} \text{ergs/s} \times XT_9^5 \left(\frac{g_{14}}{2}\right)^{-1} R_{10}^2 \quad (1.5)$$

where T_9 is the temperature in GK, g_{14} is the surface gravity in 10^{14}cm^{-2} , R_{10} is the neutron star radius in 10km, X is the mass fraction of the particular nuclear isotope undergoing the Urca process whose nuclear properties are given by L_{34}

$$L_{34} = 0.87 \left(\frac{10^6 \text{s}}{ft}\right) \left(\frac{56}{A}\right) \left(\frac{Q_{\text{EC}}}{4 \text{MeV}}\right) \left(\frac{\langle F \rangle^*}{0.5}\right) \quad (1.6)$$

where ft is the nuclear ft value, which gives the comparative half-life for a given nuclear weak transition, A is the nuclear mass number, Q_{EC} is the electron capture Q -value, and $\langle F \rangle^*$ is the Coulomb factor given by

$$\langle F \rangle^* = \frac{F^+ F^-}{F^+ + F^-} \quad (1.7)$$

with

$$\langle F \rangle^\pm = \frac{2\pi\alpha Z}{|1 - \exp(\mp 2\pi\alpha Z)|} \quad (1.8)$$

and α is the fine structure constant.

Thus the two most important nuclear physics quantities to define in order to evaluate the Urca cooling luminosity is then the mass fraction of the Urca cooler in the ashes, as well as the ft value of the decay. The abundance of the isotope is dictated by the physics of the preceding X-ray or superburst which created the ashes to be cooled, as well as the physics

of the neutron star environment it sinks into.

Of most importance to Urca cooling is the ft value from the ground state of the parent to the ground state (or very low-lying state) of the daughter. The phase space in which Urca cooling is allowed is very small. The limited phase space means that the β -decay must be from the ground state to the ground state, or very low-lying excited states (within $\sim kT$ of the ground state) in the daughter nucleus [19]. β -decays to higher excited states are disallowed as the electron must have an energy within kT of ϵ_F and because $\epsilon_F \sim Q$ since an electron capture must have occurred to produce the β -decaying nucleus. Similarly, electron capture must occur from ground state to ground state, as otherwise the electron Fermi energy would exceed the β -decay Q -value, blocking all β decay.

Moreover, the candidates for Urca cooling are further restricted to odd- A nuclei, as the odd-even mass stagger in even- A nuclei makes the possible conditions for Urca cooling very rare. Under normal neutron star crust conditions, $Q_{\text{EC}}(A, Z \rightarrow A, Z - 1) > Q'_{\text{EC}}(A, Z - 1 \rightarrow A, Z - 2)$ which means that once the first electron captures onto the even- A , even- Z nucleus, a second electron immediately captures onto the now even- A , odd- Z nucleus to again form an even- A , even- Z nucleus. This nucleus is precluded from β -decaying as the Q_{β^-} is smaller than the electron Fermi energy and so the electron is locked out of the phase space.

The prime candidates for Urca cooling pairs are then odd- A nuclei with strong ground state to ground state transitions and whose mass chains are produced in significant abundance during X-ray and superburst nucleosynthesis. Of particular interest to superburst mechanics are the mass chains $A = 57, 59$, which are known to exist in significant quantities in these ashes [23].

1.2.2 β -decays and ft values

β decays are an electroweak interaction between one nucleus and another. The three types of β -decays are β^+ , β^- and electron capture (EC) which take the form:

$$\begin{aligned}\beta^+ &: {}^A_Z X \rightarrow {}^A_{Z-1} Y + e^+ + \nu_e \\ \beta^- &: {}^A_Z X \rightarrow {}^A_{Z+1} Y + e^- + \bar{\nu}_e \\ \text{EC} &: {}^A_Z X + e^- \rightarrow {}^A_{Z-1} Y + \nu_e\end{aligned}\tag{1.9}$$

Each of these transitions involve the conversion of a neutron to a proton or a proton to a neutron. The reaction Q value, which—assuming the mass of the neutrino is zero, and the electron binding energy (~ 10 eV) is ignored—is evaluated as:

$$Q(\beta^-) = \text{BE}\left({}^A_Z X\right) - \text{BE}\left({}^A_{Z-1} Y\right) + \delta_{nH}\tag{1.10}$$

where the first two terms are the binding energies of the final and initial nuclei respectively, and the third term arises from the mass difference between a single neutron and the H atom:

$$\delta_{nH} = \Delta_n c^2 - \Delta_H c^2 = 0.782 \text{ MeV}\tag{1.11}$$

The energy released by a given β -decay is equivalent to the corresponding Q value. This energy is then split between the three products of the decay, namely: the recoiling nucleus, the electron, and the electron antineutrino for a β^- -decay. As the nucleus is far heavier than the electron and neutrino—and momentum is conserved—most of the energy is split between the two leptons. However, the decay may populate an excited state of the daughter nucleus, and thus decrease the energy available to the electron and neutrino. The available

kinetic energy is given by

$$K = K_e + K_{\bar{\nu}} = Q - E_x \quad (1.12)$$

where E_x is the excitation energy of the daughter nucleus. Because β -decay is a three-body process, the distribution of the kinetic energy between these particles is probabilistic rather than definite, and so an energy spectrum results. The electron kinetic energy is given by

$$N(K_e) = CF(Z, Q)|M_{fi}|^2(Q - K_e)^2(K_e + m_e c^2)\sqrt{K_e^2 + 2K_e m_e c^2}(K_e + m_e c^2) \quad (1.13)$$

where $F(Z, Q)$ is the Fermi function, M_{fi} is the nuclear matrix element for the interaction, and C is a constant [24].

As a quantum mechanical process, β -decays are dependent on quantum mechanical selection rules, which dictate the allowed differences in angular momentum between the parent and daughter nucleus. Generally, smaller differences in angular momentum are favorable to larger differences, as the electron angular momentum must account for the difference, and a large difference means the electron must be localized far from the parent nucleus. The difference in angular momentum and parity characterizes the “allowedness” of the decay (Tab. 1.1). “Allowed” decays are ones whose decay particles carry no angular momentum, i.e. $L = 0$. “Allowed” decays are then split into “superaligned”—where the electron and neutrino spins couple to total spin $S = 0$ —and simply “allowed”—where the electron and neutrino couple to total spin $S = 1$. Decays whose particles carry orbital angular momentum $L > 0$ are termed “forbidden” based on the angular momentum carried. Quantum mechanical selection rules then determine the allowed changes in parity ($\Delta\pi$) and total angular momentum (ΔJ) of the decay for a given forbiddenness.

Transition	L	ΔJ	$\Delta\pi$
Fermi (“superallowed”)	0	0	0
Gamow-Teller (“allowed”)	0	0,1	0
First-forbidden	1	0, 1, 2	1
Second-forbidden	2	1, 2, 3	0
Third-forbidden	3	2, 3, 4	1
Fourth-forbidden	4	3, 4, 5	0

Table 1.1: Table showing the selection rules which define the “allowedness” of a given β -decay.

The n -th “allowedness” of a decay has a direct impact on the rate at which the given decay occurs. This rate W_β has the form

$$W_\beta = \frac{|M_{fi}|^2 f}{C_n (\bar{\lambda}_{ce})^{2n}} \quad (1.14)$$

where M_{fi} is the nuclear matrix element interaction, C_n is a constant, $\bar{\lambda}_{ce}$ is the Compton wavelength of the electron, and f is the Fermi integral. This rate is rewritten using the total half-life of a nucleus, $T_{1/2}$ and:

$$W = \frac{\ln(2)}{T_{1/2}} \quad (1.15)$$

as

$$fT_{1/2} = \frac{\ln(2)C_n(\bar{\lambda}_{ce})^{2n}}{|M_{fi}|^2} \quad (1.16)$$

which is an expression commonly known as an ft value, giving the comparative half-life of a given transition. This value can take on a range of values over several orders of magnitude and so is usually reported as the $\log ft$ value. For a transition between the initial state of the parent and a particular state in the daughter, the $\log ft$ value is

$$\log ft = \log \left(f(Z, Q) \times \frac{T_{1/2}}{I_\beta} \right) \quad (1.17)$$

where I_β gives the intensity of transitions from the parent state, to a specific state in the daughter.

1.2.3 β -delayed emission

A β -decay can populate a number of excited states in the daughter nucleus. As a result this excitation will subsequently need to relax to the ground state unless it is an isomeric state with a sufficiently long lifetime to undergo another β -decay. This relaxation appears as the emission of an additional particle. Of particular relevance to this thesis are β -delayed γ -ray emission, and β -delayed neutron emission.

In β -delayed γ -ray emission, an excited quantum state is populated in the daughter nucleus, and a number of γ -rays are emitted which carry away the energy difference from the excited state to the ground state. Every nucleus has its own definite excited states at definite energies, known as a level scheme. As the excitation energy increases, the states become more densely packed and gradually begin to appear as more of a continuum than individual quanta. At these higher excited states, several γ -rays are often emitted as the nucleus relaxes to the ground state, resulting in a cascade of γ -rays of varying energies.

For nuclei which are so neutron-rich that the neutron separation energy of the daughter is below the Q_{β^-} of decay from the parent, an additional possible decay path is through β -delayed neutron emission, in which an excited state above the neutron separation energy is populated, and this state emits a neutron before relaxing. After the neutron is emitted the neutron-daughter can potentially also be populated in an excited state, which would relax via γ -ray emission characteristic of the neutron-daughter's level scheme.

1.3 Goal of This Work

The goal of this work is to advance the understanding of Urca cooling in accreting neutron stars that undergo superbursts by determining the relevant nuclear properties experimentally. The ground state to ground state transitions that are crucial to the strength of Urca cooling can be measured experimentally for extremely neutron-rich nuclei via β -decay observation at the National Superconducting Cyclotron Laboratory (NSCL). Superburst ashes are composed primarily of intermediate mass nuclei ($A \sim 50\text{--}70$) and Urca cooling is proposed to be strongest along mass chains $A = 57, 59, 61$ [1, 25].

The ground state to ground state transitions of mass chain $A = 57$ are known experimentally up to ^{57}Ti ($N = 35$), with significant cooling expected from the unconstrained ^{57}Sc and ^{57}Ca β -decays (Tab. 1.2). For $A = 59$, the transitions are constrained up to ^{59}Cr ($N = 35$), with significant expected cooling from ^{59}Ti and ^{59}Sc , but not ^{59}V due to the larger difference in spin between its ground state and the ground state of its daughter, ^{59}Cr . Finally, for $A = 61$ the forerunner to this experiment further constrained the ground state to ground state transition strength of ^{61}V , reducing its effective cooling [26]. Beyond ($N = 38$) only ^{61}Ti is expected to contribute significant cooling but is not accessible with current experimental beam rates.

1.4 Experimental Approach

The primary tools with which to better understand the nuclear mechanisms and properties of the crusts of neutron stars are theoretical calculations and experimental measurements of the electron capture and β^- -decay rates which constitute Urca processes. Theoretical models for these decays are extrapolated from known experimental results and currently understood

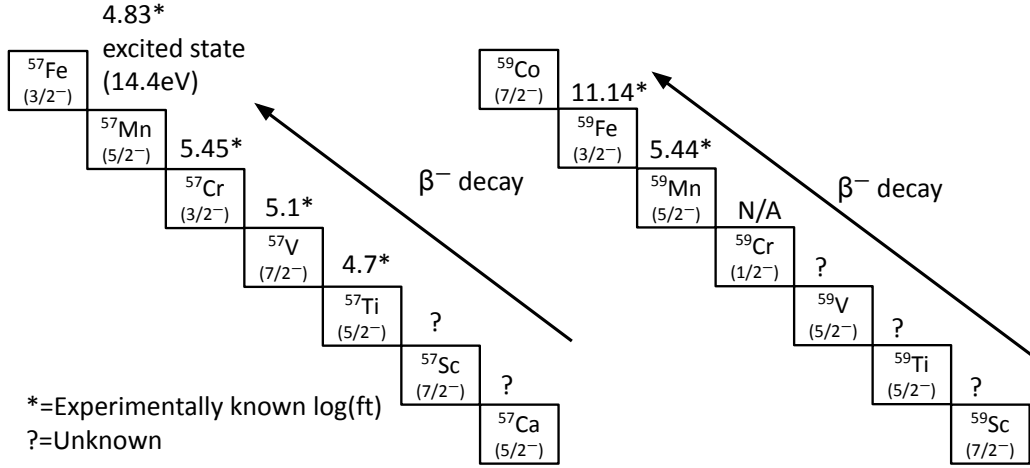


Figure 1.2: State of ground state spins and ground state to ground state transitions for $A = 57, 59$ mass chains. These run from the neutron-rich nuclei expected to contribute to Urca cooling back to stability.

physics, and remain untested in these exotic regimes. Thus, additional experimental results are necessary. However, experimental measurements of electron capture rates in the neutron-rich environments of neutron stars are difficult to obtain in lab environments due to the negative Q value for these transitions [27]. This leaves experimental β^- -decay studies as one of the primary avenues for understanding the workings of neutron star crusts.

As Urca processes are primarily concerned with ground-state transitions, measuring these transition strengths are the most important experimental target. However, as β -decays are a three-body process, with one of those bodies (the neutrino) evading detection, the ground-state transition cannot be measured directly. Instead, the ground-state transition can be inferred by observing all other transition strengths, with the remainder attributed to the ground-state. This method requires a high-efficiency γ -ray detector for observing all the β -delayed γ -ray emission as well as a neutron detector to measure the β -delayed neutron

emission rate.

Many of the past γ -ray spectroscopy measurements on the neutron-rich isotopes of interest have used high-purity Ge (HPGe) detectors, whose high resolutions allow for precisely determined γ -ray energies. Twelve γ -rays are found to decay through five energy levels in ^{57}Ti β -decay to ^{57}V [11]. Five γ -rays are identified with relative intensities—though only one level placed—in the β -decay of ^{57}Sc to ^{57}Ti [3]. Finally, no known γ -rays or levels have been identified in the β -decay of ^{59}Ti to ^{59}V [28, 29, 30]. However, the limited efficiency of these detectors can cause the measured transition strengths to be heavily skewed towards lower energy transitions, often missing significant feeding to higher excited states. This is known as the Pandemonium² effect, and has a particularly pronounced impact with higher multiplicity and higher energy γ -ray cascades [31]. Past measurements of the target decays ^{57}Ti , ^{57}Sc , and ^{59}Ti are only able to establish levels up to 2.5 MeV, 4×10^{-1} MeV and 0 MeV but have Q -values of 10.50(27) MeV, 12.92(133) MeV and 12.32(26) MeV [32]. Thus there is a very large window of unknown energy levels which makes these experiments susceptible to the Pandemonium effect, and high-efficiency detector measurements are required in order to evaluate the impact.

Total absorption spectroscopy (TAS) is a method of utilizing a (nearly) 4π solid angle detector, with high efficiency to γ -rays, in order to capture as much energy as possible from the γ -ray cascades following β -delayed γ emission. Ideally a TAS detector sums all γ -rays in a cascade and is therefore able to identify even weak transitions to highly excited states correctly. For example, a theoretical decay which populates only two excited states (Fig. 1.3), with the higher-energy state cascading through the lower-energy state, a HPGe detector would identify the single γ -ray energies from the cascades, but would rely on coincidence

²Referencing the capital city Pandemonium in J. Milton's *Paradise Lost*

data to correctly assemble the level scheme. Under the TAS method, the energies of the two γ -rays would clearly define a sum peak, correctly indicating the energies of the two levels.

TAS detector efficiencies are high, but not 100%, which does lead to incomplete summing of γ -rays, and potentially mistaking a cascading γ -ray as an individual from a distinct energy level. Accurate simulations of the detector physics can be used to reconstruct hypothetical decays, and properly reconstruct the level scheme. Moreover, as TAS detectors are commonly comprised of several individual segmented detectors, and as the kinematics of the decays favor emission of γ -rays in opposing directions, segment spectra can be used as lower-resolution, individual γ -ray spectra. While the resolution is not as precise as HPGe, these individual segment spectra are used in concert with the TAS in order to accurately identify the γ -rays corresponding to total energy peaks.

1.5 Overview of Thesis

With the primary goal of identifying the β -feeding strengths in neutron-rich isotopes of mass $A = 57, 59$ experimental methods and schema are presented in Ch. 2. These experimental methods are supported by various simulation techniques outlined in Ch. 3. Analytical methods used to interpret the experimental data, including detector calibrations, defined event correlations, and background subtraction are discussed in Ch. 4. The complete experimental results are presented in Ch. 5. These results are compared with existing theoretical nuclear physics calculations, and applied to current astrophysical models to estimate the total Urca cooling impact in Ch. 6. Finally, Ch. 7 summarizes the results and impact, and concludes with targets of future study.

HR gamma spectrum vs. TAS gamma spectrum

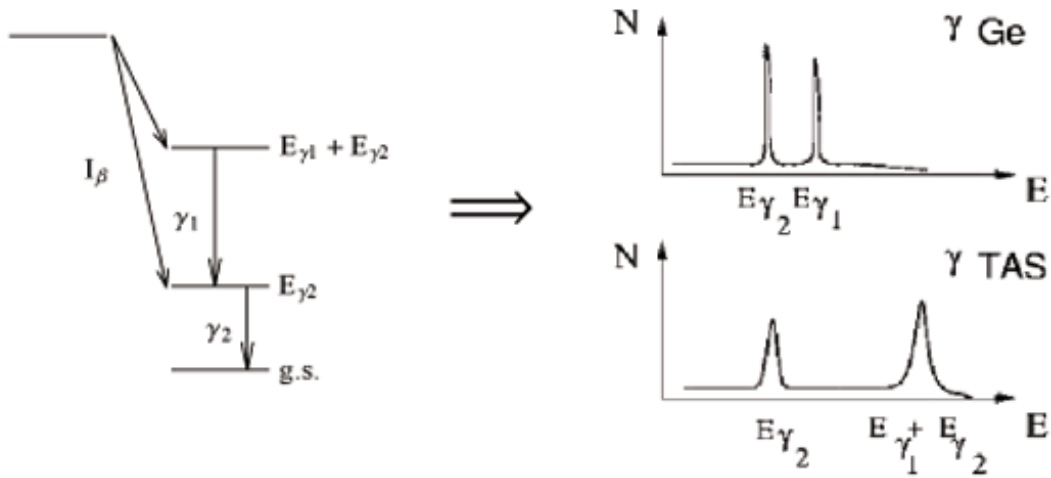


Figure 1.3: Comparison of theoretical, ideal γ -ray spectra from a high-purity Ge detector and a high-efficiency TAS detector, for a hypothetical decay involving feeding to two individual states, reproduced from [4]. Since all decays to the second excited state involve emission of both γ_1 and γ_2 , the TAS shows a peak at the summed $E_{\gamma_1} + E_{\gamma_2}$. Therefore the TAS spectrum shows directly the feeding intensity of the excited states in the daughter nucleus while the Ge spectrum would rely on coincidence data to correctly identify that γ_1 results from only feeding to the summed energy level. In reality, where the TAS summing is not 100%, an additional, smaller peak at E_{γ_1} would exist for incompletely summed decays.

Chapter 2

Experimental Methods

The experimental setup was constructed to study the β -decay properties of several neutron-rich isotopes in the mass range of $A = 55$ – 59 , with the ultimate goal of determining or constraining the ground-state to ground-state transition strength of the odd- A isotopes in this region. High-efficiency detectors were employed to measure the characteristics of these β -decays. As β -decays are a 3-body decay, and the neutrinos emitted during the decay escape detection entirely, the total energy of the decay cannot be detected directly, and therefore ground state decays cannot be directly identified. Instead, the ground state population has to be determined indirectly from the population of excited states that can be inferred from the detection of β -delayed γ -rays and β -delayed neutrons. Thus the probability of emission to the ground state is equal to the difference shown in Eq. 2.1 as used in [26]

$$P_{\text{g.s.}} = 1 - P_{\text{n}} - \sum_i P_{\gamma,i} \quad (2.1)$$

where P_{n} is the probability of emitting a neutron and decaying to the neutron-daughter nucleus, and $P_{\gamma,i}$ is the probability of decay to the i -th excited state (including continuum states) in the daughter nucleus.

The experimental setup was designed to detect both the β -delayed γ decays and the β -delayed neutron decays. Toward this goal, the experiment included two separate portions, one to measure the probability of neutron emission of the parent nuclei, and one to measure

the γ -ray cascades following decays to excited states in the daughter nuclei. The first portion utilized a combination of the Beta Counting System (BCS) [33] to detect implanted ions and their resultant β -decay electrons, and the Neutron Emission Ratio Observer (NERO) [7] to detect neutron events. The second portion used the Summing NaI(Tl) (SuN) [8] in conjunction with a small double-sided silicon strip detector (DSSD) to observe γ -rays from correlated implanted and subsequently decaying nuclei.

2.1 Experimental Overview

The two experimental end stations were set up in the S2 vault of the National Superconducting Cyclotron Laboratory (NSCL) from 26 March 2019 to 2 April 2019 for a total of 174 hours of beam time on target. Using the coupled cyclotron facility (CCF) a primary beam of ^{82}Se was accelerated and impinged on a Be target, producing a cocktail beam via fragmentation to be purified by the A1900 particle separator. A schematic of the production beam line up to the A1900 focal plane is seen in Fig. 2.1 [5, 6]. A purified beam of nuclei around ^{58}Ti was delivered to the decay station, first to the target position at the center of the BCS in NERO for a total of 27 hours, and then, following a rapid changeover, to the target position at the center of the SuN detector for another 147 hours.

2.1.1 Beam Production and A1900 Separator

Primary beam selection, A1900 specifications, as well as downstream degrader thicknesses, were chosen based on LISE⁺⁺ [34] simulations to maximize production and implantation of ^{55}Ca , ^{57}Sc , and ^{59}Ti . Per these simulations, $^{82}\text{Se}^{34+}$ was chosen as the primary beam at an energy of 140 MeV/u, and impinged on a Be target with a thickness of 493 mg cm⁻². A

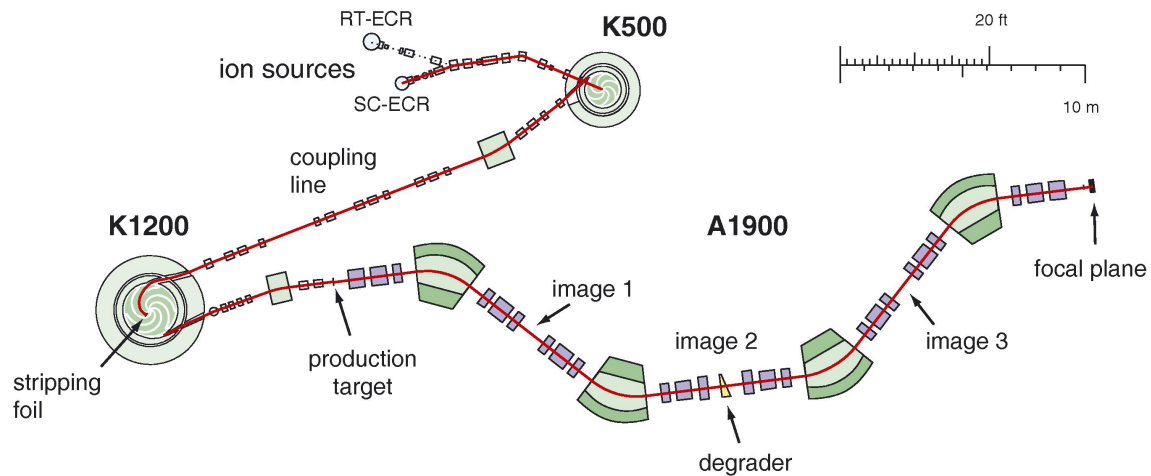


Figure 2.1: Schematic of the CCF and A1900 at the NSCL, figure reproduced from [5]. Particularly of note is the wedge degrader at Image 2, which was used to further separate beam components by momentum. Immediately downstream of the degrader is a scintillator (not pictured) with two photomultiplier tubes used as a time-of-flight trigger for particle identification [5, 6].

Image 2

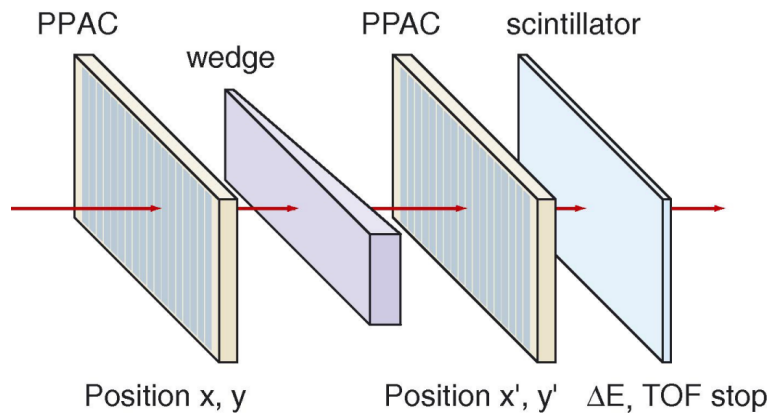


Figure 2.2: Schematic of the wedge-shaped energy degrader in the A1900 separator [5, 6] at the Image 2 position. Also seen here is the scintillator, which acted as the stop gate on the time-of-flight calculation for particle identification. Figure reproduced from [5].

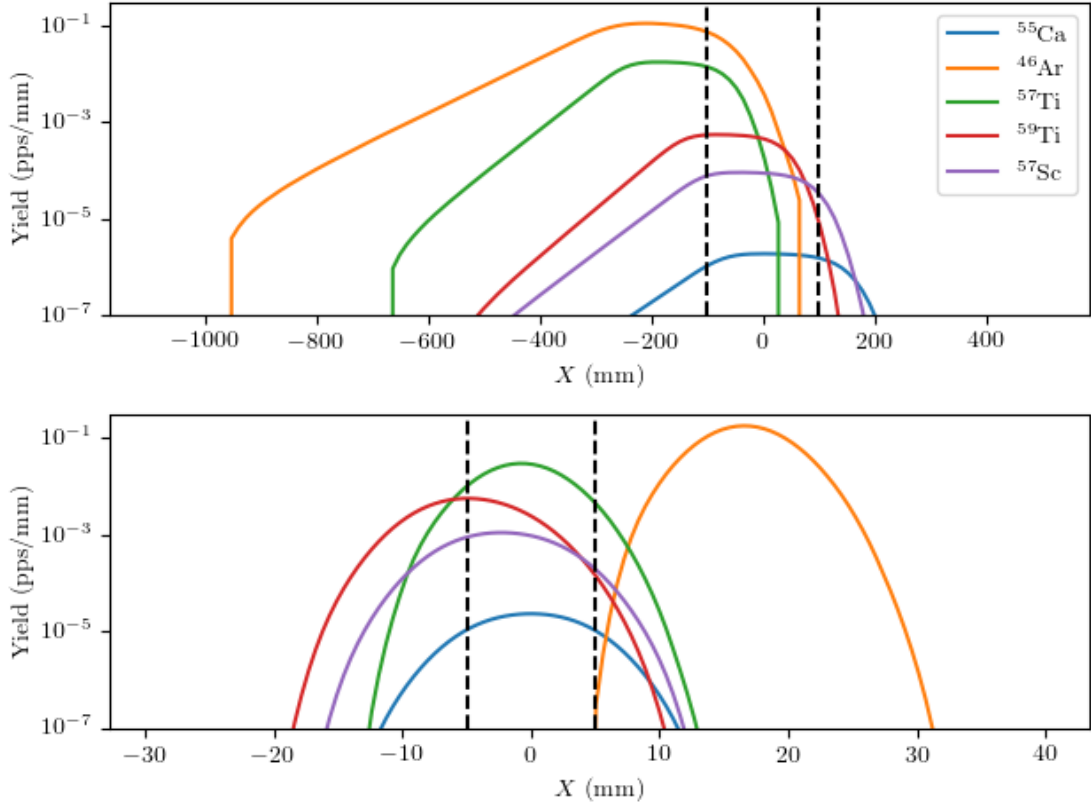


Figure 2.3: LISE⁺⁺ simulated yield vs. X at Image 1 (top) and at the focal plane (bottom) in the A1900. The dashed black lines indicate the slits selecting on X position at Image 1 (± 100 mm), and at the focal plane (± 5 mm). Only the particles of interest and the sample contaminant ^{46}Ar are shown.

20 mg cm^{-2} thick Kapton wedge-shaped degrader (Fig. 2.2) was used at the Image 2 (I2) position to further separate the beam composition by energy loss and subsequent energy dispersion.

The vast majority of secondary beam nuclei produced via projectile fragmentation from the Be target was irrelevant for this experiment. Thus the A1900 separator was employed to purify the secondary beam by mass, atomic charge, and nuclear charge via magnetic-rigidity analysis and energy-loss through degrader materials, in this case a Kapton wedge. The first half of the A1900 selected a specific magnetic rigidity, $B\rho = mv/q$ by inserting slits at the Image 1 (I1) and I2 positions. The top plot in Fig. 2.3 shows this first selection, as 88%

of the yield of the sample contaminant ^{46}Ar was removed via the I1 slits. The remaining beam then passes through the wedge-shaped energy degrader, generating a residual $B\rho$. The energy loss in the degrader follows the well-known Bethe formula [35] and for large ions at low velocities approximates to the relationship

$$\Delta E \propto \frac{\Delta x Z^2}{Av^2} \quad (2.2)$$

The very different manner in which the residual $B\rho$ relates to A , Z and v compared to the original $B\rho$ enables the second $B\rho$ selection stage of the A1900 to further purify the beam [36]. The final $B\rho$ selection was made at the focal plane (FP) at the end of the A1900 beamline, where additional position slits were inserted. The bottom plot of Fig. 2.3 shows the final selection, where effectively all of the remaining ^{46}Ar was removed. The slits were adjusted as needed throughout the course of the experiment, the I2 slits were set to $\Delta B\rho/B\rho = \Delta p/p = 3.75\%$ for the NERO portion, and shifted between $\Delta p/p = 1-2\%$ for the SuN portion.

The final result was a filtered secondary beam containing several isotopes of interest, notably $^{53-55}\text{Ca}$, $^{55-57}\text{Sc}$, and $^{57-59}\text{Ti}$. Despite the separation and selection achieved by the A1900, several contaminants were also present, including $^{59-61}\text{V}$ and $^{61-63}\text{Cr}$. The detector system was then used to identify incoming beam particles event by event.

2.2 Detector Setup

The entire detector system consisted of three main detectors: the BCS, NERO, and SuN with its DSSD. Additionally, a stack of two silicon PIN detectors were positioned just upstream of

the end station along with aluminum degraders. These PINs provided particle identification data for both the BCS/NERO and SuN detector systems.

2.2.1 Particle Identification

As discussed in Sec. 2.1.1, the secondary beam still contained over a dozen individual isotopes upon delivery to the detector station. Thus particle identification was critical to correlate individual implanted isotopes with observed decays. To this end, two silicon PIN detectors were placed at the entrance to the decay station. These PIN detectors acted as active degraders that recorded the energy loss as a signal to the data acquisition. This energy loss (δE) was then combined with a measurement of the time-of-flight (TOF) of the ions from the I2 position to the PIN detectors. Together this provided unique A vs. Z particle identification using the δE -TOF method [37].

The PIN detectors for the δE measurement—PIN01 and PIN02—had respective thicknesses of 503 μm and 1000 μm . Given the beam energy and composition, expected energy deposition in the PINs was ~ 250 MeV and ~ 570 MeV respectively. The TOF calculation was done using the signal in the PIN detectors as a start gate, stopped by the delayed upstream signal of the particles passing through the plastic scintillator at I2 (Fig. 2.1) in the A1900.

Following the energy deposition in the PIN detectors, an array of aluminum degraders were used to further slow the beam to ensure that the isotopes of interest were properly implanted in the downstream detectors. The necessary thicknesses of the degraders was estimated prior to the experiment by LISE⁺⁺ to be 3300 μm and 4800 μm for the BCS/NERO and SuN portions of the experiment respectively. The degraders, however, were mounted in the beam line on a rotating plate, which allowed for slight adjustments to be made to

the thicknesses without opening the system to air. Thus the precise thickness was tuned in order to maximize the implantation rate observed during the experiment.

2.2.2 BCS

Following the upstream PINs and degraders, the beam entered the main decay station. For the BCS/NERO portion, this was the BCS chamber. The BCS chamber [33] is a 22 cm diameter vacuum chamber containing four additional detectors, namely (in order from upstream to downstream): a third silicon PIN detector (referred to as PIN03, 1041 μm thickness), a double-sided silicon strip detector (BCS DSSD, 997 μm thickness), a single-sided silicon strip detector (SSSD), and a scintillator. These detectors worked in concert to 1) confirm beam transmission to the BCS from the upstream PINs, 2) detect DSSD implants and subsequent decays, 3) distinguish DSSD punchthrough events from true implants, 4) distinguish potential light beam particle signals from true decay events.

The BCS DSSD was the principal detector of this set, boasting an array of 40 1 mm strips on each side, oriented orthogonally for a grand total of 1600 individual pixels over a 4 cm \times 4 cm active face. These pixels provided localization and correlation in space of implantation and decay events.

2.2.3 NERO

Surrounding the BCS chamber was the NERO neutron counter, see Fig. 2.4, a matrix of gas-filled proportional counters distributed across concentric rings within a 60 cm \times 60 cm \times 80 cm high-density polyethylene matrix, whose long symmetry axis lies along the beamline [7]. The polyethylene matrix acts as a neutron moderator, slowing passing neutrons such that they

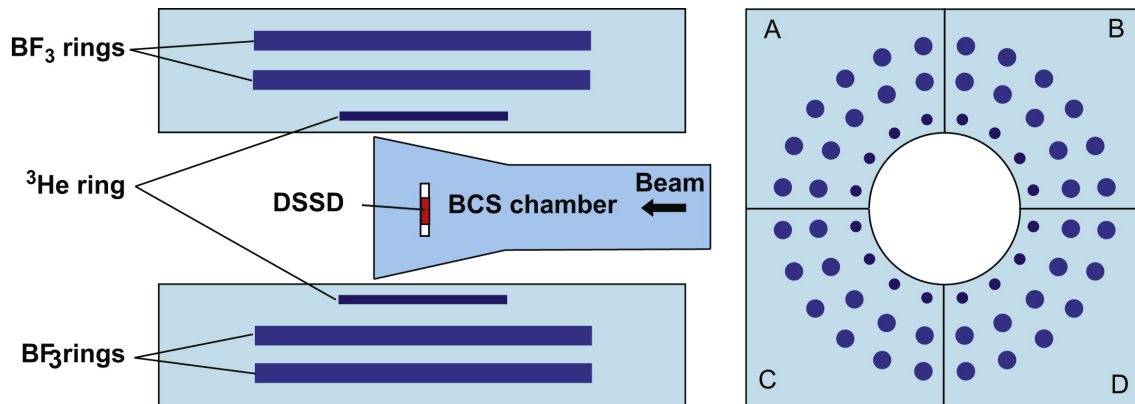


Figure 2.4: A schematic of the BCS inside the NERO array. Note that NERO is arranged such that the BCS DSSD is at the center of the NERO detectors to maximize neutron detection efficiency. Figure reproduced from [7].

have a higher cross-section for reacting with the proportional counters. These counters are filled with BF_3 and ^3He gases, which will capture neutrons per the reactions $^{10}\text{B}(n, \alpha)^7\text{Li}$ and $^3\text{He}(n, p)^3\text{H}$ respectively. The innermost rings are composed of the 16 ^3He tubes, with the 44 BF_3 tubes filling the outer rings. To each of the proportional counter tubes a high-voltage is applied, ensuring that, should a reaction occur, the produced charged particle is observed through electron cascades and “counted”.

The NERO array is designed to have a high and—importantly—flat efficiency for low energy ($<2\text{ MeV}$) neutrons. This is very important as it precludes the need for energy dependent corrections to be made in the observation of neutrons emitted via β -delayed neutron decay. While neutrons emitted under these decays follow an energy spectrum with a maximum theoretical value of $E_{\beta n} = Q_{\beta} - S_n$, their distributions are heavily skewed to much lower energies $<1\text{ MeV}$ [38]. High resolution spectroscopic studies of β -delayed neutron emitters via fission confirm that the neutron energies generally fall below 1 MeV [39, 40]. The unfortunate downside of using a long counter such as NERO, is that by moderating and absorbing the emitted neutrons, all original information on the energy of the neutrons is lost. However, the experimental goal is only to determine a P_n , which does not require

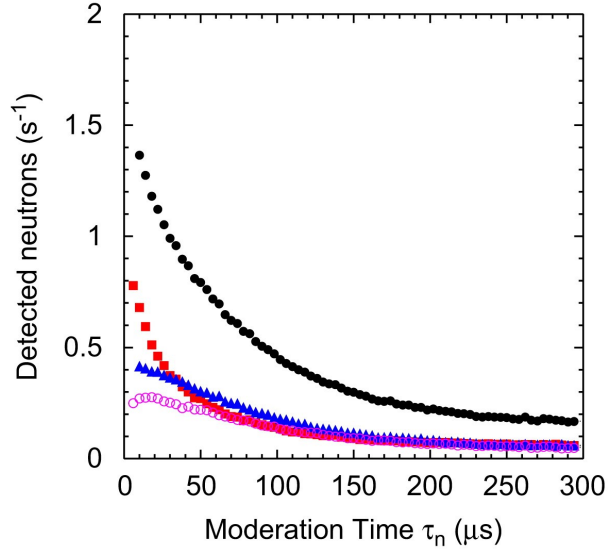


Figure 2.5: Neutron moderation time in the NERO matrix reproduced from [7]. The inner (red squares), middle (blue triangles) and outer (pink empty circles) ring moderation times are shown, as well as the combined total for the detector (black filled circles).

information on the neutron energies.

Of additional importance is the required moderation time of neutrons in the NERO matrix. The neutron capture cross-section increases as the neutron energy decreases, hence the need for the polyethylene matrix. However, the moderation is not instantaneous and follows a profile described in [1, 7] and shown in Fig. 2.5. Consequently, a longer time window of 200 μs is required following the registration of a decay event to properly correlate the decay with its emitted neutron.

2.2.4 SuN

The final detector in the overall system was the Summing NaI(Tl) (SuN) scintillator [8]. It comprises eight segments, each composed of three individual PMTs, as seen in Fig. 2.6. Due to the fast response time of the NaI(Tl) scintillators and nearly 4π coverage of the detector as a whole, SuN is able to achieve high efficiency detection and correlation of γ -rays, while

maintaining sufficient resolutions of individual γ -rays via the separate segments. While high-precision germanium detectors are also commonly used for decay experiments, the goals of this experiment necessitate a higher efficiency detector, as observing all the γ -rays in a single decay allows for complete reconstruction of the event, a much more reliable determination of feeding probabilities for excited states, and thus a and better estimation of the ground-state feeding intensity.

As with the BCS, the secondary beam was implanted into a double-sided silicon strip detector (SuN DSSD, 1000 μm thickness) at the center of the SuN detector, which then observed the resulting β -decay. The SuN DSSD has a 20 mm \times 20 mm active area, subdivided into 16 1.25 mm wide strips orthogonally on the x and y planes. Thus a 256 pixel matrix was used to localize individual particle implants and their corresponding decays. Similarly to the BCS apparatus, a plastic scintillator veto was positioned at the end cap of the SuN beampipe, and served the dual purpose of vetoing failed implantations (“punchthroughs”) as well as light particle signals.

The advantages of SuN as a total absorption spectrometer are illustrated by looking at the results of a ^{60}Co —a well known decay—source run. ^{60}Co ($T_{1/2} = 1925.28$ d) β^- -decays to the 2505 keV energy level in its daughter ^{60}Ni in 99.85% of decays. In turn, this excited state relaxes to the ground state primarily via emission of two γ -rays of energy 1173 keV (99.85% intensity) and 1332 keV (99.98% intensity). Thus, these decays almost exclusively involve the emission of two γ -rays of unique energy from a single energy level. As a total absorption spectrometer, the individual segment spectra of SuN measure the energies of the two γ -rays, and the total absorption spectrum (TAS) shows the combined energy of the entire decay. The sum of the individual segments (SS) shows a summary of all events detected by any segment, while the TAS shows the energy sum of all simultaneous events.

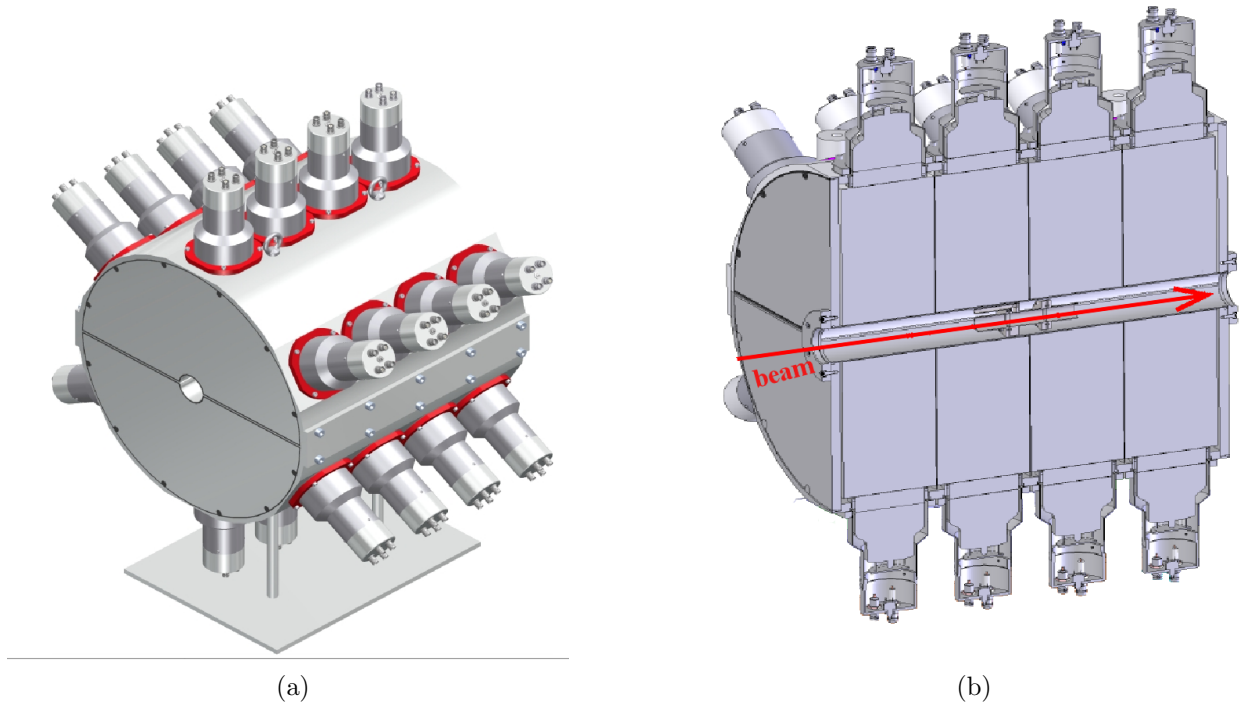


Figure 2.6: Schematics of the SuN detector as a whole (Fig.2.6a) as well as a cross section showing the direction of the incoming beam (Fig.2.6b). Note that the SuN DSSD is positioned halfway through the length of the detector, and stopped the beam there. Figures reproduced from [8].

Fig. 2.7 shows these two spectra from a given source run overlaid for clarity. Clearly visible are the individual γ -ray peaks at 1173 keV and 1332 keV in the SS, as well as the combined 2505 keV total energy peak in the TAS. Also notable are the two peaks in the TAS at the γ -ray energies, indicating some incomplete summing in SuN, as well as the combined energy peak in the SS, indicating that *both* γ -rays from a single decay are detected in the *same* segment of SuN.

Additionally, inset within Fig. 2.7 is the third primary observable from the SuN detector: the multiplicity distribution. This distribution is constructed from the given events as the total number of distinct segments recording a nonzero measurement. It is clear from this distribution that the source run contains a significant amount of background signals in addi-

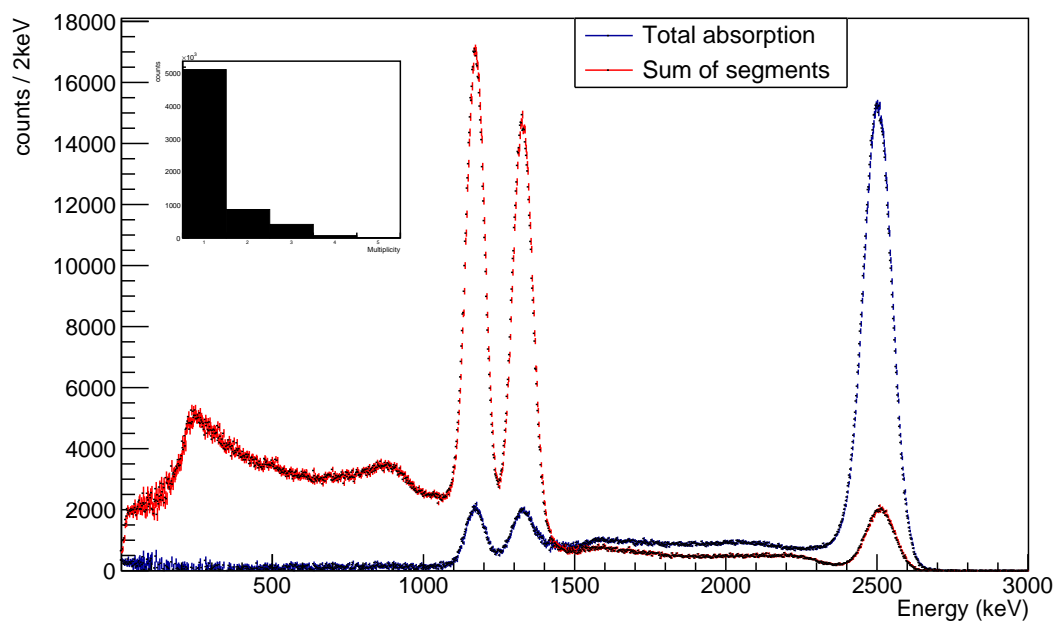


Figure 2.7: Overlaid comparison of the two main spectra observed by SuN in the ^{60}Co decay: the sum of individual segments (red), and the total absorption (blue). Visible are the two separate individual γ -ray peaks in the sum of segments, as well as the clear sum peak in the total absorption. Inset is the multiplicity distribution, from 1 to 5 distinct segments.

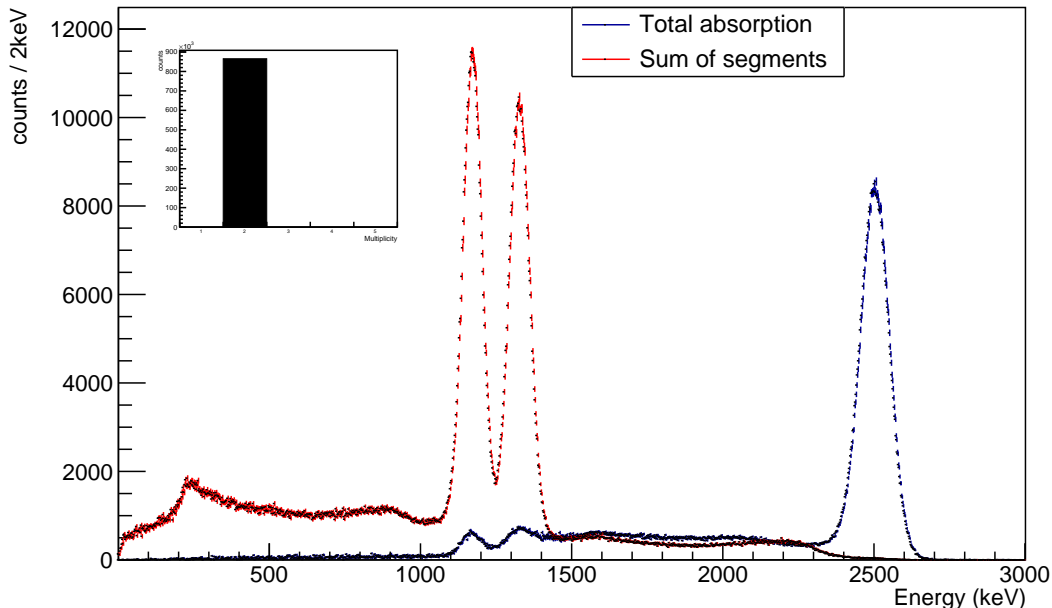


Figure 2.8: Same as Fig. 2.7 but now only including events with an exact multiplicity of two segments. The inset multiplicity distribution demonstrates this cut.

tion to the expected multiplicity one and two events from ^{60}Co decay. While the background subtraction method is discussed in greater detail in 4.1, it is illuminating to see the power of the multiplicity restriction of SuN here. Accordingly, Fig. 2.8 shows the same spectra from the same source run, but instead of including all multiplicity events, only the events which record signals in exactly two of SuN’s segments are shown. Nearly all the incomplete summing peaks and the single segment peaks are removed from the corresponding spectra—those that remain are simply randomly correlated background signals—and the low-energy background spectra is significantly suppressed.

2.3 Electronics Setup

The electronics setup for the experiment was the same as in previous experiments [41, 1] and was based on the NSCL digital data acquisition system (DDAS) [9]. DDAS relies on high

frequency (100 and 250 MHz) XIA Pixie-16 digitizer modules in conjunction with a Pixie-16 crate and a host controller to handle processing of all input signals. As a result, the signal processing itself is highly customizable, and each channel of a Pixie-16 module can be tuned to its source input. The specific settings can then be saved and stored for use in future experiments, assuming the setup is identical.

The Pixie-16 modules primarily rely on trapezoidal filters in the signal processing. The details are discussed in [9], but are best illuminated in Fig. 2.9. Fig. 2.9(a) shows a generic preamplified detector signal, as it may appear on an analog oscilloscope. Fig. 2.9(b) then shows the digital constant fraction discriminator (CFD) and trigger filter response to the generic signal. The trigger-filter threshold operates as the threshold for starting the DDAS signal processing. This threshold is there to cut out the majority of detector noise, and is set just below the upper edge of the noise peak on a channel-by-channel basis. Finally, Fig. 2.9(c) shows the response of the energy filter algorithm to the same generic signal. This algorithm is what allows for DDAS to extract an energy value from the signal relative to the other signals in the same channel. The three core configurations for the energy filter algorithm are the energy filter range, rise time, and flat top time. First, the energy filter range sets the number of ADC samples to be averaged for one step in the energy filter. The rise time and flat top time combine to give the extraction time, T_{Ex} , at which point the amplitude of the energy filter is read out as the energy of the signal. These energy filter settings can be customized for each channel of the detector, but are commonly set identically for identical detector outputs, and will be discussed in further detail for each detector.

All the detectors are biased through a corresponding multichannel high voltage power supply, with the output signals fed through a preamplifier before reading into the Pixie-16 modules. Generally, each detector component outputs a single signal, at a certain gain.

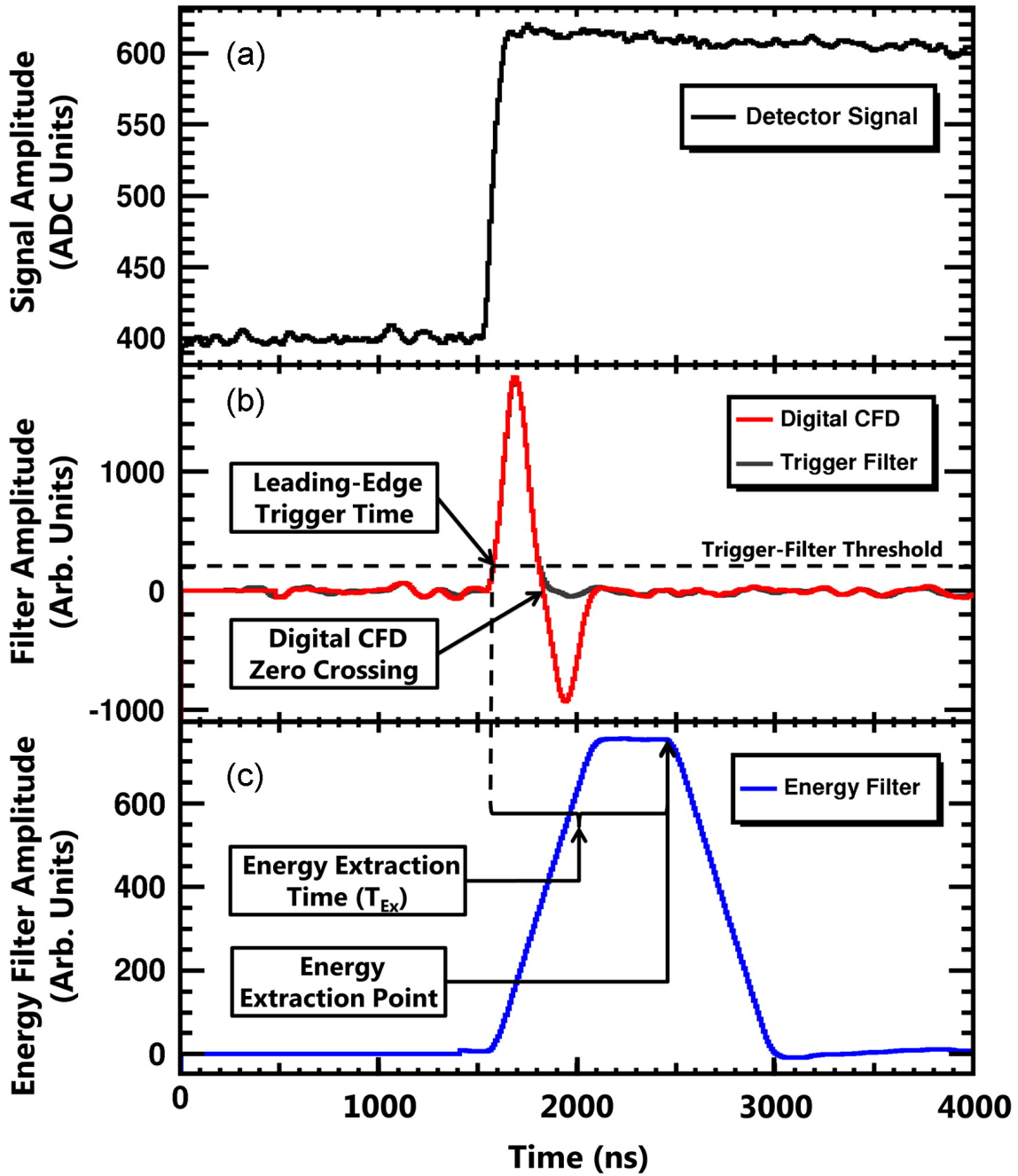


Figure 2.9: DDAS filter settings for signal processing in the Pixie-16 modules, figure reproduced from [9]. (a) shows the raw preamplified signal from the detector; (b) shows the digital constant fraction discriminator (CFD) and trigger-filter response to the signal in (a); and (c) shows the energy filter algorithm response.

The DSSD electronics—for both the SuN and BCS DSSDs—however, are somewhat more complex, as each strip of the DSSD outputs both a low-gain (to detect implantations) and a high-gain (to detect decays) signal. Moreover, in order to limit background events, the DSSD signals are hardware-gated to require a coincidence with the other side of the detector. This ensures that any recorded event can be spatially localized to a specific pixel on the DSSD.

2.3.1 BCS

The BCS stack produced output signals from one PIN (low gain, 1 channel), one DSSD (high and low gain, 160 total channels), one SSSD (high gain, 16 channels), and a veto detector (1 channel), in addition to the upstream PINs (2 channels) and TACs (5 channels), for a total of 185 individual detector output signals, on top of the 60 signals from the NERO setup. The sheer number of signals, along with the need to keep the SuN setup as static as possible, meant that multiple XIA Pixie crates were required for data acquisition. For the BCS portion, the crate holding the DSSD and SSSD were marked as the master crate, with the NERO and SuN crates each designated as sub-crates in the multi-crate setup. For the BCS portion, the SuN crate only recorded signals from the PINs, TACs, and BCS scintillator veto, and all remaining channels were turned off.

Each detector was biased to a high-voltage according to its specific requirements, and signals were passed through preamplifiers before being submitted to the Pixie-16 modules. The DSSD signals stand out as they were passed through dual-gain preamplifiers which allow for reading both the high and low gain outputs. Moreover, an OR gate TTL signal (1 if any channel has a signal, 0 otherwise) was extracted via the front panel of the Pixie-16 modules, for each of the modules which contain the front and back signals from the DSSD. This OR gate was then additionally OR gated with the other signals from the same side and same

Detector signal	Energy Filters			Thresh. Filters		
	Range	T_{rise} (μ s)	T_{flat} (μ s)	T_{rise} (μ s)	T_{flat} (μ s)	Thresh. (ADC)
DSSD _{high}	3	9.2	0.64	6.16	4.0	\sim 1400
DSSD _{low}	1	2.3	0.24	1.34	1.2	\sim 2000
SSSD	3	3.04	0.48	7.76	2.4	\sim 4000
PIN1	3	2.08	0.8	8.96	1.2	\sim 20000
PIN2	3	1.040	0.4	5.12	3.2	\sim 6400
PIN3	3	0.8	0.4	5.12	3.2	\sim 6400
TACs	3	1.28	1.28	0.48	0.08	\sim 600
Veto	3	0.8	0.24	0.8	0	\sim 1000

Table 2.1: Table showing the DDAS filter settings for the BCS detectors. Note that the thresholds varied widely by channel, thus an approximate value is shown here.

gain of the detector, and this aggregate OR signal was then AND gated with the aggregate OR signal of corresponding gain from the other side of the detector. The output of the AND gate was then returned to each module. This signal processing allowed for only recording signals which could be properly localized on the DSSD.

Energy and trigger filter settings were adjusted for each channel to optimize the energy resolution and reduce the noise signal, particularly for the DSSD. The resulting rise times, flat top times, and filter ranges are shown in Tab. 2.1. While these settings are likely not optimized for any given experiment in the future, they do provide a potential starting point from which further optimizations can be made to the specific case in question.

2.3.2 NERO

Each detector in NERO is an individual tube of either ^3He or BF_3 gas. As outlined, these detectors are arranged in different rings throughout the NERO matrix, and separated into four different quadrants, shown in Fig. 2.4, called Quads A, B, C, and D. Each Quad consists of four ^3He tubes and 11 BF_3 tubes. Each detector is biased via a high-voltage power supply, and the output is passed through a preamplifier before being fed to a Pixie-16

Detector signal	Energy Filters			Thresh. Filters		
	Range	T_{rise} (μs)	T_{flat} (μs)	T_{rise} (μs)	T_{flat} (μs)	Thresh. (ADC)
NERO ^3He	3	2.0	2.0	4.0	0.8	~ 1000
NERO BF_3	3	2.0	1.04	4.0	0.8	~ 800

Table 2.2: Table showing the DDAS filter settings for the NERO detectors. The thresholds varied widely by tube, thus an approximate value is shown here.

module. Similarly to the BCS, the energy and trigger filter settings in DDAS were optimized in order to read in the signals from the detectors while reducing noise. The DDAS parameters for processing the NERO detector signals are described in Tab. 2.2.

2.3.3 SuN

Signal processing of the SuN silicon detectors followed much of the same logic as the BCS detectors, with the important difference that the DSSD only outputs a total of 64 combined high and low gain channels instead of the 160 from the BCS DSSD. However, the same logic gating as for the BCS DSSD was necessary in order to limit the data rate of the detector by limiting the data acquisition to properly localized events. Thus the same OR and AND gating to guarantee coincident signals on the front and back of the detector are applied to the SuN DSSD as in Sec. 2.3.1.

The PMTs in the SuN scintillators operate with internal triggers which only pass when all three PMTs in a specific segment of SuN record a nonzero signal. This allowed the software thresholds for the SuN PMTs to be set lower while preventing a dramatically increased count rate due to noise alone. All other detectors in the SuN setup use self-triggering modes. The collective DDAS settings for all the detectors used in the SuN arrangement are shown in Tab. 2.3.

Detector signal	Energy Filters			Thresh. Filters		
	Range	T_{rise} (μs)	T_{flat} (μs)	T_{rise} (μs)	T_{flat} (μs)	Thresh. (ADC)
DSSD _{high}	3	0.96	0.512	4.928	3.20	~ 2000
DSSD _{low}	3	0.96	0.512	4.928	3.20	~ 400
SuN PMTs	3	0.48	0.16	0.16	0.048	~ 20
PIN1	3	1.664	0.64	7.168	0.96	~ 11200
PIN2	3	0.832	0.32	4.096	4.096	~ 6400
TACs	3	1.024	1.024	0.384	0.064	~ 600
Veto	3	1.664	0.64	4.096	2.56	~ 3000

Table 2.3: Table showing the DDAS filter settings for the SuN detectors. Note that the thresholds vary widely by channel, thus an approximate value is shown here.

2.3.4 Physics Events

NSCL Data Acquisition (NSCLDAQ) software was used to group individual detector signals into defined physics events. In order to do this, each signal that passes the trigger thresholds for the corresponding channel is timestamped—NSCL DDAS allows for synchronization of every channel within ± 10 ns[42]—and written out to an NSCL data acquisition ring buffer. These ring buffers are collected by the PIXIE crate controller and passed to an NSCLDAQ event builder. Each individual crate in the multi-crate setup has its own controller, and all the corresponding ring buffers are joined together under the event building software, which assigns a global timestamp to the data dumped from the ring.

Once the data packets are joined and properly tagged with timestamp and source information, they can be grouped—“glommed”—into a defined physics event. This is done by setting a coincidence window and glomming all events within that window together. Thus, a group of signals indicating the implant of a beam particle or the decay of an implanted isotope can be properly joined as a single event.

The coincidence window is set to 300 ns for the SuN portion of the experiment in order to reduce the contribution from background, while the NERO coincidence window is set to

200 μs to allow for the moderation of neutrons through the NERO matrix (described in Sec. 2.2.3).

Chapter 3

Simulation Methods

3.1 GEANT4 Simulations

In order to extract γ -ray branchings from the decays observed in SuN, the entire detector system is modeled using the GEANT4 [43] software package (v9.5.2) and individual events are then simulated and analyzed. A decay scheme can be constructed from and verified against comparisons between observed and simulated data. Details of the GEANT4 model are provided in past works [41], which have explored in-depth the necessary parameters for modeling the SuN detector efficiency and resolution.

The simulations consist of a complete software reconstruction of the SuN detector apparatus, including the SuN DSSD and its mount. Then, a β -decay or β - γ event is simulated by placing the particle(s) in a random initial location within the physical size of the SuN DSSD with a probability distribution corresponding to the observed distribution of implants. Each particle is assigned an energy; γ -ray energies for a given simulation are specified at exact values via an input file. The γ -ray energies are chosen based on the decay and energy in question, as discussed later. The energy of the electron is sampled from the β -decay energy distribution of allowed transitions, using the Q -value of the β -decay transition to be simulated. The antineutrino is assumed to escape detection due to its low cross section and is not simulated. All particles are emitted isotropically from the initial location within the

SuN DSSD. Particle transport and interactions with physical elements are then calculated via GEANT4 physics libraries per the version (v9.5.2), with the detector response defined by the function determined in [41]. The resulting signals in the SuN PMTs from the particles interacting with the scintillator material are simulated and recorded in a structure analogous to the observed data. Notably, the deposition of energy from electrons in the SuN scintillators can complicate observed spectra [1]. Thus, simulating the electron is very important for fully characterizing the measured energy spectrum of a decay event.

In addition to β -delayed γ emission, β -delayed neutron emission is expected among the neutron-rich isotopes being measured. As a result, templates for the β -delayed neutron and potentially β -delayed neutron- γ emission also need to be simulated. Neutrons are known to interact with NaI(Tl) detectors through inelastic scattering on ^{23}Na and ^{127}I , potentially capturing on ^{127}I which results in a total energy deposition, $E = {}^{128}\text{I}S_n + E_n$ [44]. These interactions lead to subsequent γ -ray cascades, which are observed along with β -delayed γ -rays. As the energy distributions of the β -delayed neutrons are not well characterized, the SuN response to these decays are simulated using monoenergetic neutrons of 1 MeV.

3.1.1 GEANT4 Validation

To validate the simulations, they are bench-marked against experimental data obtained from a γ -ray emitting ^{60}Co calibration source. The activity of the particular source is known from factory calibrations, and is used along with the known γ -ray intensities of ^{60}Co decay, to estimate the total number of γ -rays expected to be observed. However, when comparing directly with the observed data, the simulated spectra are normalized to the observed spectra, such that the total counts match. Fig. 3.1 shows the agreement between the observed and simulated TAS and SS. The summing efficiency for the simulated and observed ^{60}Co source

is 67(2)% and 63(2)% respectively, both in agreement with results from [8].

The slightly decreased observed summing efficiency is a known characteristic of SuN for highly active γ -ray sources [45], such as the one used here with an estimated activity of $5.6 \times 10^3 \gamma/s$. This is much higher than the γ rate of isotopes seen in the experiment. The total implantation rate is $\sim 6 \text{ imp/s}$. The average rate of γ -rays per implantation varies by isotope, but can be conservatively estimated as $<5 \gamma/\text{imp}$, resulting in a total γ rate two orders of magnitude below the source rate, which would indicate the calculated summing efficiencies are conservative. Thus, the simulations reproduce the observed spectra, providing confidence that simulated templates can be used to extract the unknown level scheme transitions from the experimental γ -ray spectrum.

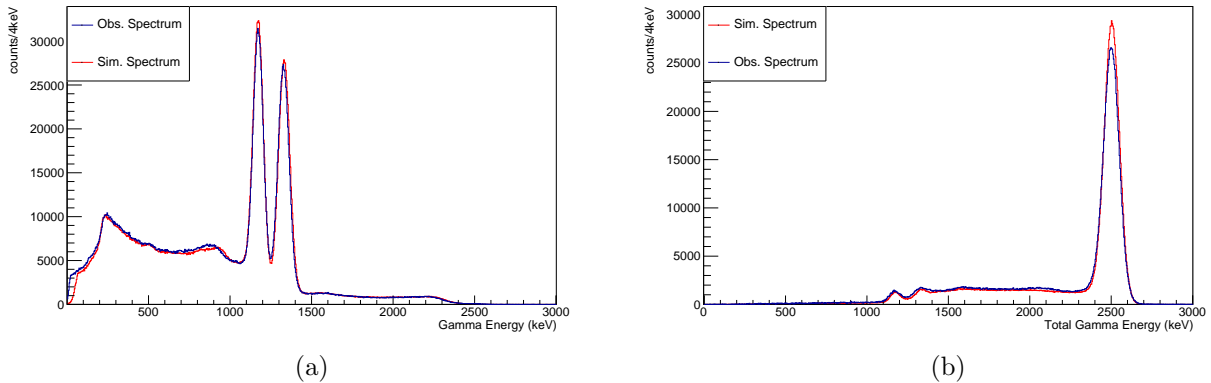


Figure 3.1: Histograms of the SuN TAS and SS for an observed (blue) and simulated (red) ^{60}Co source. All are filtered to only include events with multiplicity ≥ 2 .

3.1.2 GEANT4 Template Construction

The simulation of the SuN detector in GEANT4 is now used to extract β -decay feeding intensities using GEANT4 generated templates. A template is the detector response spectrum generated by the deexcitation pathways from a given excited state to the ground state. It

is constructed from the linear superposition of one or more individual sub-templates that represents specific deexcitation paths to the ground state. The experimental data are then fitted using a linear superposition of templates for each excited state or energy bin up to the Q -value that can be fed by the β -decay. The coefficients of the linear superposition of the templates yield the desired feeding intensities.

As introduced in 1.2, the level scheme of an isotope prescribes the possible states and deexcitation transitions that a given excited nucleus can pass through while relaxing to the ground state. The level scheme is discrete for low excitation energies, but as the excitation energy increases, the nuclear level density (NLD) increases and eventually forms a continuum region [46]. This is observed experimentally as the total energy detected in a decay transitions from clear, discrete energies, to a more continuous energy spectrum. The level diagram above the discrete scheme can be approximated as a quasi-continuum using a prescribed NLD. An example diagram of a NLD by excitation energy is shown in Fig. 3.2. Of the three nuclei of interest, only ^{57}Ti has a known level scheme. For the other isotopes, the level scheme is constructed based on the observed decays. The ^{57}Ti decays are compared to previous data to validate the method. E_{crit} is chosen as the energy where discrete states are no longer clearly identifiable in the TAS due to both the increasing NLD and the detector resolution.

For decays to excitation energies in the discrete level region, feeding is limited to the discrete states. There is a template for each state that is determined by simulating in **GEANT4** the γ -ray cascade from this state. This requires input γ -ray decay branchings of all states in the cascade. These are taken from previous measurements when available, and constructed from the experimental data otherwise.

An example template can be seen in the decay of ^{57}Ti , for which the TAS is shown in Fig. 3.3 and the previously proposed level scheme [11] is shown in Fig. 3.4. Looking solely

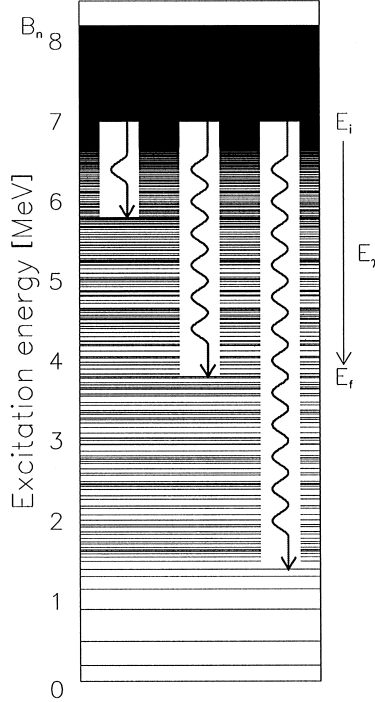


Figure 3.2: Generic example of the increase in the nuclear level density from discrete states (roughly 0–1.5 MeV) to a quasi-continuum (roughly > 1.5 MeV). Figure is reproduced from [10].

at the energy level at 2036 keV, the level scheme suggests that there are three potential γ -ray cascade pathways that a nucleus can follow to deexcite from this state. These three sub-templates are shown in Fig. 3.5 and consist of (a) a 1923 keV γ -ray to the state at 113 keV followed by a 113 keV γ -ray to the ground state; (b) a 1862 keV γ -ray to the state at 174 keV followed by a 174 keV γ -ray to the ground state; and (c) a 1862 keV γ -ray to the state at 174 keV followed by both 113 keV and 62 keV γ -rays to the ground state. The composite template that comprises the decay from the energy level at 2036 keV then consists of some linear combination of these three individual sub-templates.

This information can be confirmed from the TAS, where a gate can be applied on a specific level, in this case the level at 2036 keV. Plotting the SS gated on this total energy window then displays the γ -rays which comprise the cascade from that energy level. This, combined

with a likewise-gated multiplicity histogram (shown together with a template fit in Fig. 3.6), confirms the three cascades depicted in Fig. 3.5. Multiplicity gates are applied on the SS in addition to the TAS gates. This additional restriction then displays only those γ -rays which are coincident at a given energy level and a given multiplicity. With this information, these three cascades are each simulated in `GEANT4`.

It is important to note that a TAS-gated region is not necessarily purely representative of the decay scheme at that energy level. As mentioned in Sec. 3.1, electrons can deposit energy in the SuN PMTs that may be summed with the γ -rays, thereby increasing the total energy observed. Thus, in completely reconstructing an energy level, E_i , in the decay scheme, it is necessary to additionally include the simulated spectra from lower energies, $E_j < E_i$ in the decay scheme, gated on energy E_i . For instance, in the SS from the 2036 keV level shown in Fig. 3.6, there is a small peak around 1570 keV. This peak is not due to a deexcitation path from the level at 2036 keV, but rather from the level at 1731 keV where an electron has deposited the ~ 300 keV to make that decay appear alongside those from the 2036 keV level. In this way all determined lower energy levels are gated and included in the simulated spectra which are fit to the observed data at a higher energy level. Though the lower levels are included in order to optimize the fit, they are ignored in constructing the final template for that energy level. The “true”— γ -rays sum to the excited energy—sub-template weightings are extracted from the fit, and renormalized to unity, ignoring the lower level contributions.

Incomplete summing from higher energy levels should also be included in constructing each level template. However, including all other templates in the construction of each template would require one of two treatments: (1) a recursive fit of sub-templates for each template until the system converges, or (2) defining no fixed templates and instead fitting all

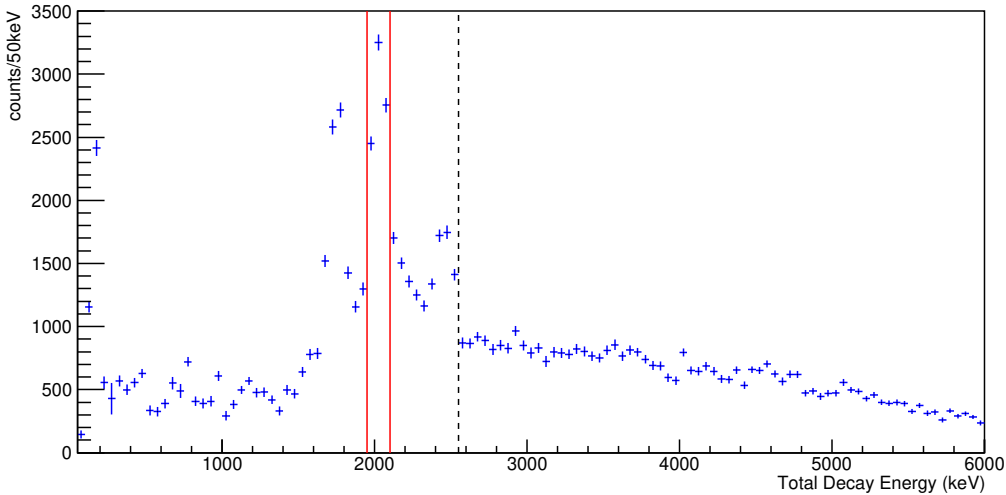


Figure 3.3: Background- and daughter-subtracted TAS for ^{57}Ti correlated decays. Red lines indicate the gates applied to select the level at 2036 keV. The black dashed line shows the cutoff, $E_{\text{crit}} = 2550$ keV, at which the discrete level region ends and the quasi-continuum begins.

possible sub-templates to determine the final feeding. Neither option was computationally feasible, and so instead the templates are built from low energy to high energy.

3.2 RAINIER Simulations

The templates for feeding states in the quasi-continuum region are obtained with the **RAINIER** simulation tool [47]. For these excitation energies, level energies are treated as a continuum, divided into energy bins. A template is then constructed for feeding into each bin, referred to as a pseudolevel. The width of the pseudolevels are chosen to correspond with the increasingly coarse resolution of SuN at higher energies: $E_{\text{crit}}-3$ MeV : 100 keV; 3 MeV–3.9 MeV : 150 keV; 3.9 MeV–7.1 MeV : 200 keV; 7.1 MeV–10.4 MeV : 300 keV; 10.4 MeV– Q : 400 keV. **RAINIER** uses a NLD and γ -ray strength functions (γSF) to calculate continuum deexcitations until the discrete states discussed above are reached. The remaining gamma

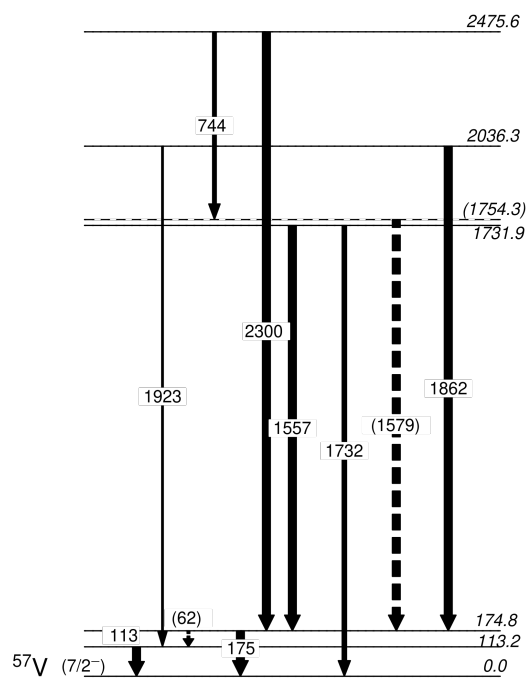


Figure 3.4: Proposed ^{57}V level scheme from [11] for the β decay of ^{57}Ti to ^{57}V

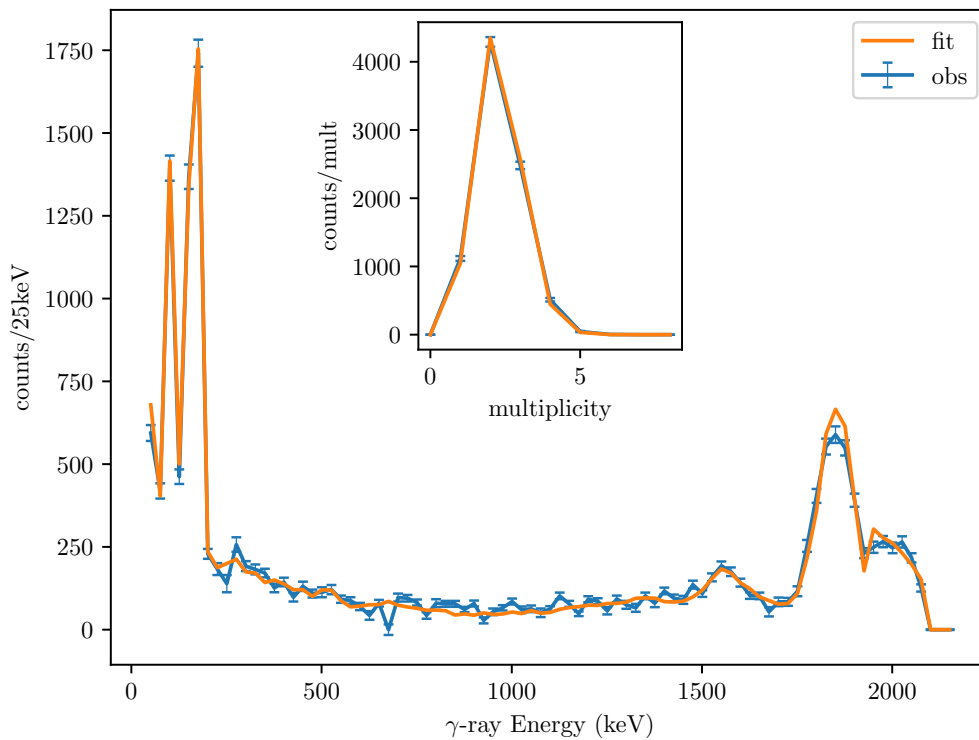


Figure 3.6: Background- and daughter-subtracted SS and multiplicity for ^{57}Ti correlated decays, gated on the 2036 keV level in the TAS. The fit of the composing γ -ray cascades from the level is shown in orange.

are included in the γ SF. As the Oslo method [10] has found a strong upbend in the M1 transition strength function in nearby ^{57}Fe [49], an upbend is also included here. The upbend takes the form of a negative exponential

$$f_{\text{upbend}} = C \exp(-aE_{\gamma}) \quad (3.1)$$

where $C = 1 \times 10^{-7} \text{ MeV}^{-3}$ and $a = 1 \text{ MeV}^{-1}$ [50].

While the β -Oslo method could in theory be used to extract the exact nuclear level density and γ -strength function parameters for any of the desired isotopes directly from the experimental results, the analysis typically requires $\mathcal{O}(100000)$ observed decays [51] in the quasi-continuum region, which was not achieved in this case for any of the studied isotopes. An attempted analysis yielded only that the employed parameters and proposed upbend is consistent with the data [45].

3.3 Methods for Estimating Feeding Uncertainty

Once all the level templates for the all energies up to the Q -value are constructed and simulated in **GEANT4**, a linear superposition of all the simulated γ distributions are fit to the corresponding observed distributions. These distributions include the TAS, SS, multiplicity, and multiplicity-gated SS ($m = 1, 2, 3, 4$). The result is the feeding intensity to each of the levels in the level scheme.

To estimate the statistical uncertainty inherent to the fit, a Monte Carlo analysis is run, such that a number of pseudodata distributions are constructed based on the observed data. Each bin from each distribution is sampled from a Poisson distribution with mean equal

to the bin counts, and then refit with the same level templates as the original observed data. This process is carried out for 50,000 samples, and the results of each are collected. A Gaussian is fit to the resulting intensity distributions, whose 1σ variance is taken as the statistical uncertainty for the observed data fit.

Second, a new method was developed which utilizes a multi-objective evolutionary algorithm to minimize the fits of the level intensities to all of the observed distributions at once, and furthermore explores the limits of the fit parameters that still result in an acceptable fit of the data. While there is a single point which minimizes the summed χ^2 of the fit to the observables, the purpose of this multi-objective method is to evaluate the sensitivity of the fit to the feeding of each individual level. The algorithm employed here is the Multi-Objective Evolutionary Algorithm based on Decomposition with a Differential Evolver (MOEA/D-DE) [52]. The multi-objective problem is constructed with the fit χ^2 of each of the TAS, SS, and multiplicity as objectives, each of the level intensities as a parameter, and an additional constraint that the sum of the fit level intensities adds up to 100%. The algorithm is then evolved, and all the candidate points are saved for each evolution. The resulting data set contains several hundreds of thousands of candidates, each one with a specific set of level intensities and χ^2 objective values. For each of the TAS, SS and multiplicity, the χ^2 is summed, and the resulting distribution of intensities is plotted (Fig. 3.7). The distribution of MOEA/D-DE intensities are approximated as Gaussian and fit with a corresponding mean and variance. The error is then taken as the 1σ errors above and below the mean. These bounds act as the systematic uncertainties for this method of fitting, and are summed in quadrature with the statistical uncertainties from the Monte Carlo to give the total uncertainty on the feeding intensities.

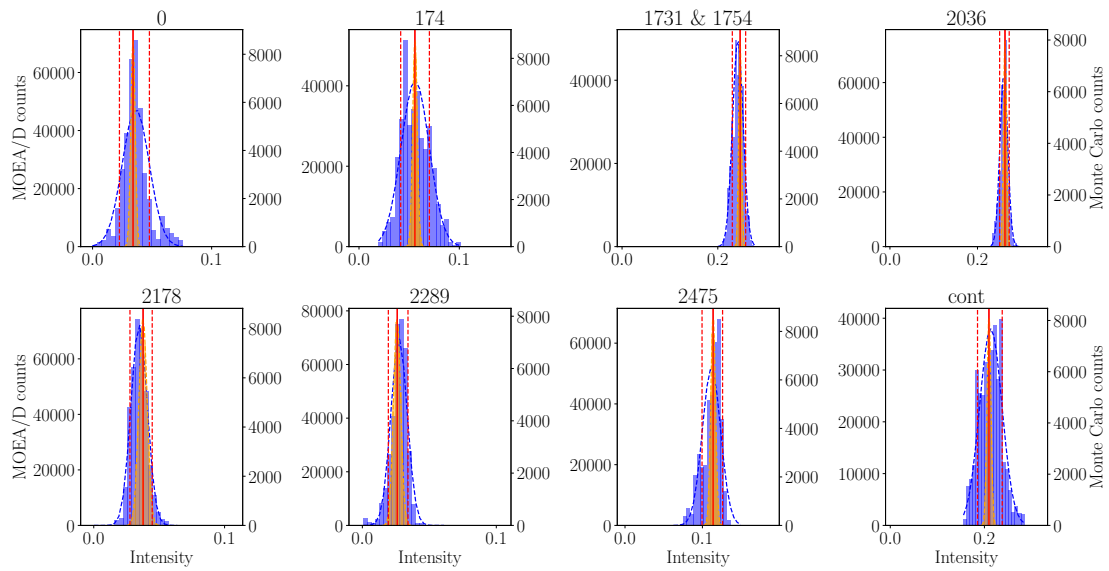


Figure 3.7: Comparative distributions of fit intensities of the MOEA/D-DE (blue) and Monte Carlo (orange) error estimations for the decay of ^{57}Ti . The vertical dashed red lines give the lower and upper bounds of the feeding uncertainty for a given level. The vertical solid red line gives the feeding intensity which minimizes the summed χ^2 obtained from the fit. The blue dashed curve is the Gaussian fit to the MOEA/D-DE distribution, and the orange dashed curve is the fit to the Monte Carlo distribution.

Chapter 4

Data Analysis

4.1 Calibrations

All the detectors described in Sec. 2.2 are calibrated using a source either to establish a direct relationship between channel and signal energy, or else to simply establish a threshold of an accepted signal over noise.

4.1.1 BCS

To begin, the upstream PIN detectors were calibrated under the high-gain setting of the PIN preamplifier with an ^{241}Am source. This source was used to set the electronic signal processing parameters listed in Tab. 2.1, which were optimized to maximize the energy resolution of the PIN detectors. After optimizing the high-gain energy resolutions using a source, the detectors are switched to the low-gain setting (maintaining the high-gain-optimized parameters), which is used for the particle identification. No source run was recorded prior to the experiment, but a post experiment run determined energy resolutions of 10.5% and 8.2% respectively on PIN01 and PIN02. Thus PIN02 was selected for use in determining particle identification plots.

The PIN03 detector was used as an active degrader and transmission check to the BCS chamber, and so was likewise optimized to improve energy resolution. The individual chan-

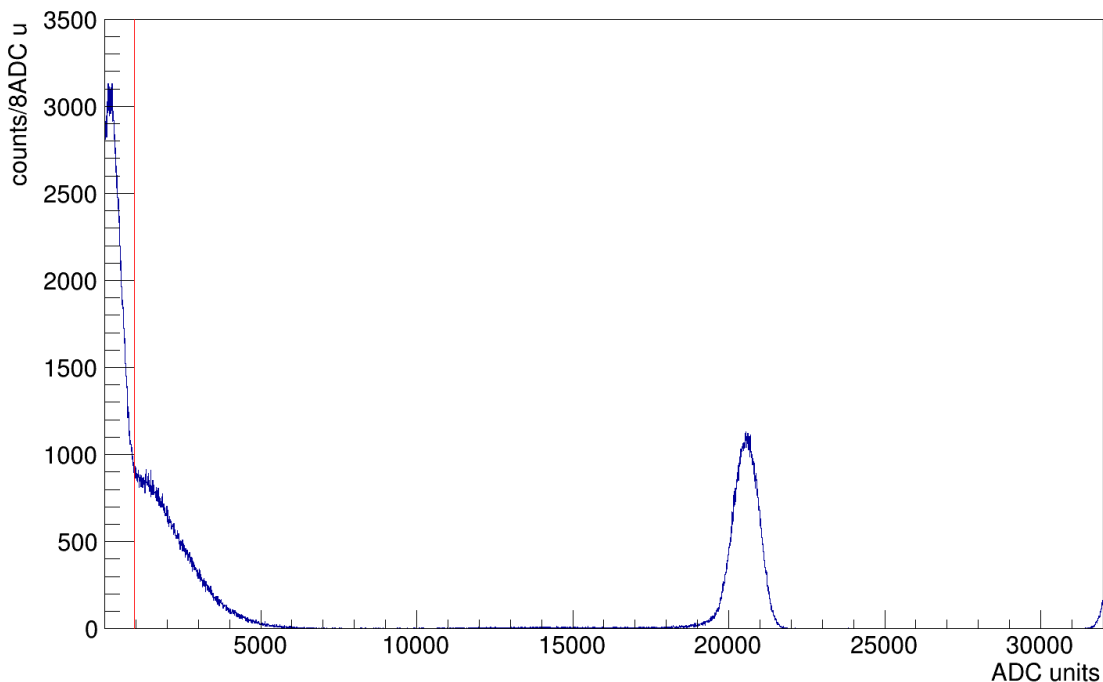


Figure 4.1: Spectra of a sample strip from the ^{241}Am and ^{90}Sr joint source run. Visible is the noise peak below the threshold (red line) at ~ 1950 ADC units which transitions into the ^{90}Sr electron β -decay spectrum. The ^{241}Am α -decay at ~ 20000 ADC units is used to gain-match the energies of each SSSD strip.

nels of the SSSD were gain-matched via an ^{241}Am source, and the low-energy thresholds were set against a ^{90}Sr source. The spectra of a sample strip from this joint source run is shown in Fig. 4.1.

The BCS DSSD high-gain signals were calibrated with a ^{228}Th source. The ^{228}Th decay chain produces α particles at 5.423, 5.685, 6.288, 6.778, and 8.785 MeV and is therefore commonly used for calibrating silicon detectors. A spectrum from a sample strip showing the first four peaks is shown in Fig. 4.2. These calibrations produced varied resolutions by strip of the silicon detector but for the 6.778 MeV energy, every strip had an energy resolution below 5%. Collectively, these four or five energy peaks were used to calibrate each strip of the detector using a linear fit, the residuals of which are shown in Figs. 4.3 and 4.4.

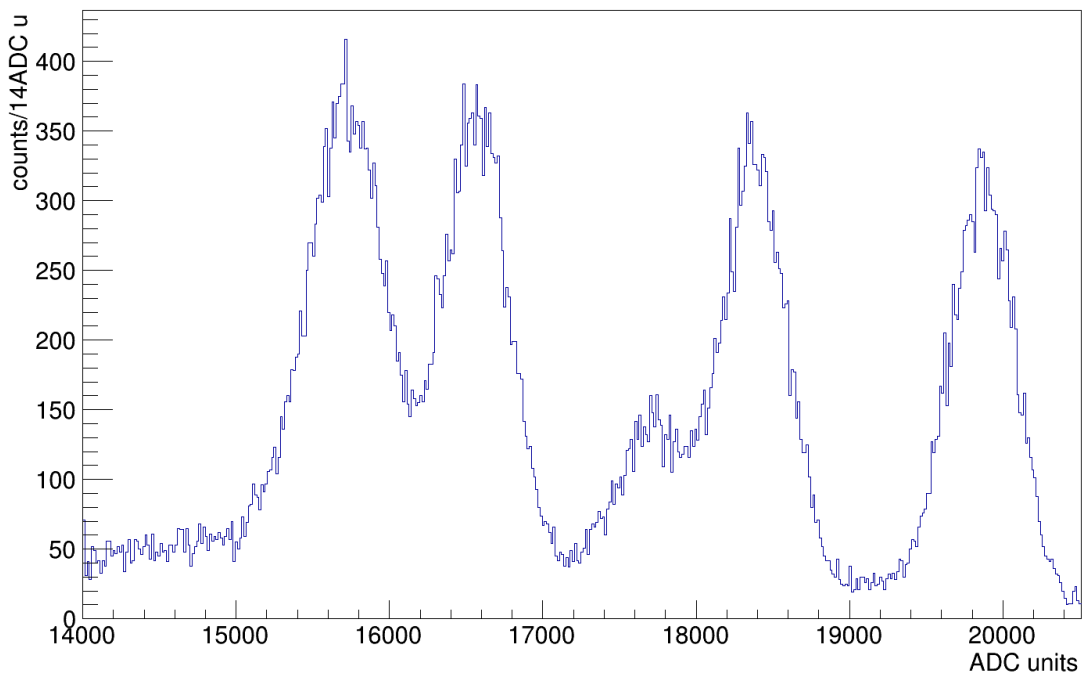


Figure 4.2: Energy spectrum for a sample strip from the ^{228}Th calibration run. Note that the gain from the preamplifier was such that the higher-energy α particle at 8.785 MeV was not visible.

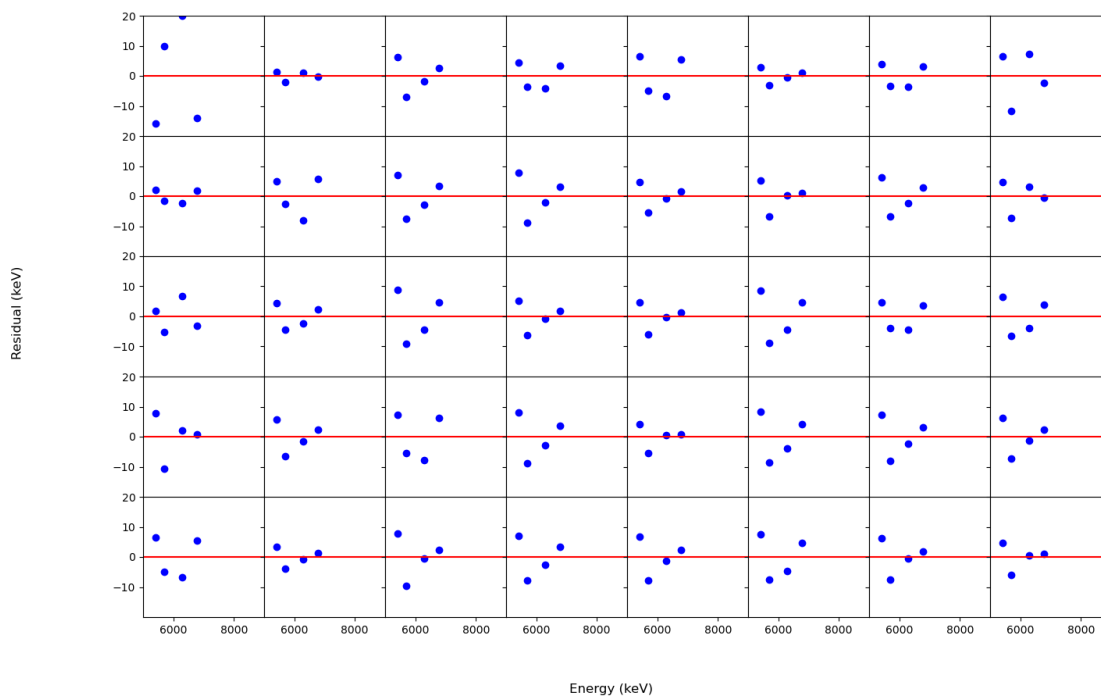


Figure 4.3: Residuals of the linear fit of the back side strips of the BCS DSSD to the calibration α particles from ^{228}Th decay. Note that the gain from the preamplifier was such that none of the spectra included the higher-energy α particle at 8.785 MeV.

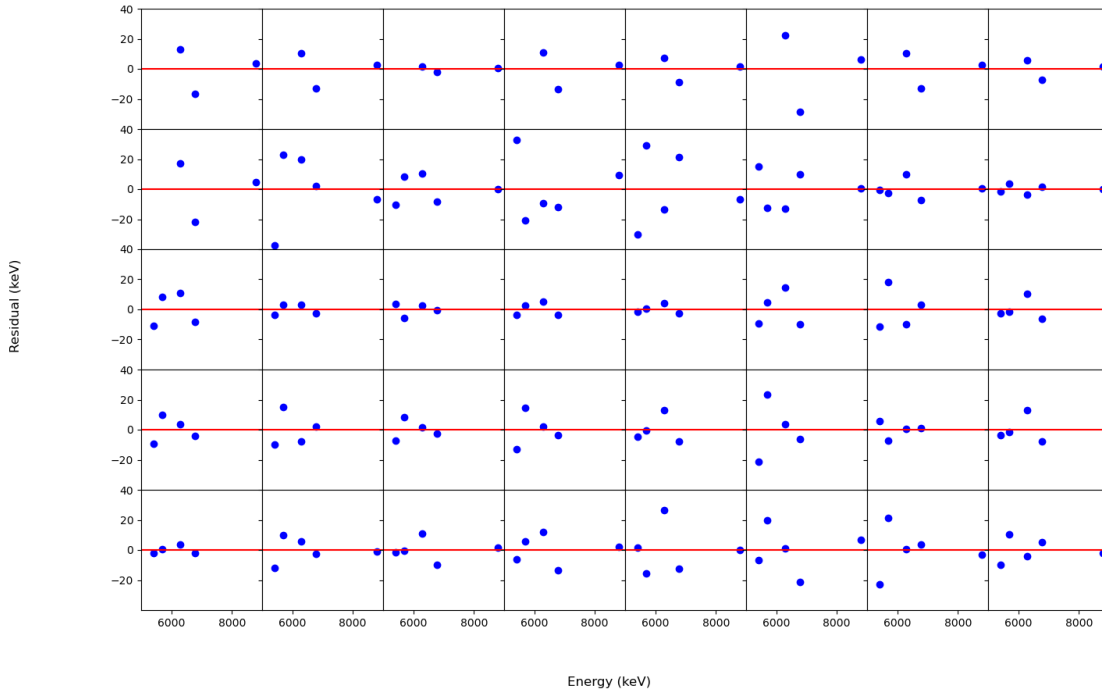


Figure 4.4: Residuals of the linear fit of the front side strips of the BCS DSSD to the calibration α particles from ^{228}Th decay. Note that the resolutions of the first nine strips were insufficient to distinguish the two lowest energy α particles at 5.423 and 5.685 MeV, and so only the higher energy particles were incorporated to the fit. As in Fig. 4.3, the gain for several of the strips was such that the higher-energy α particle at 8.785 MeV was not included and was thus not included in the fit.

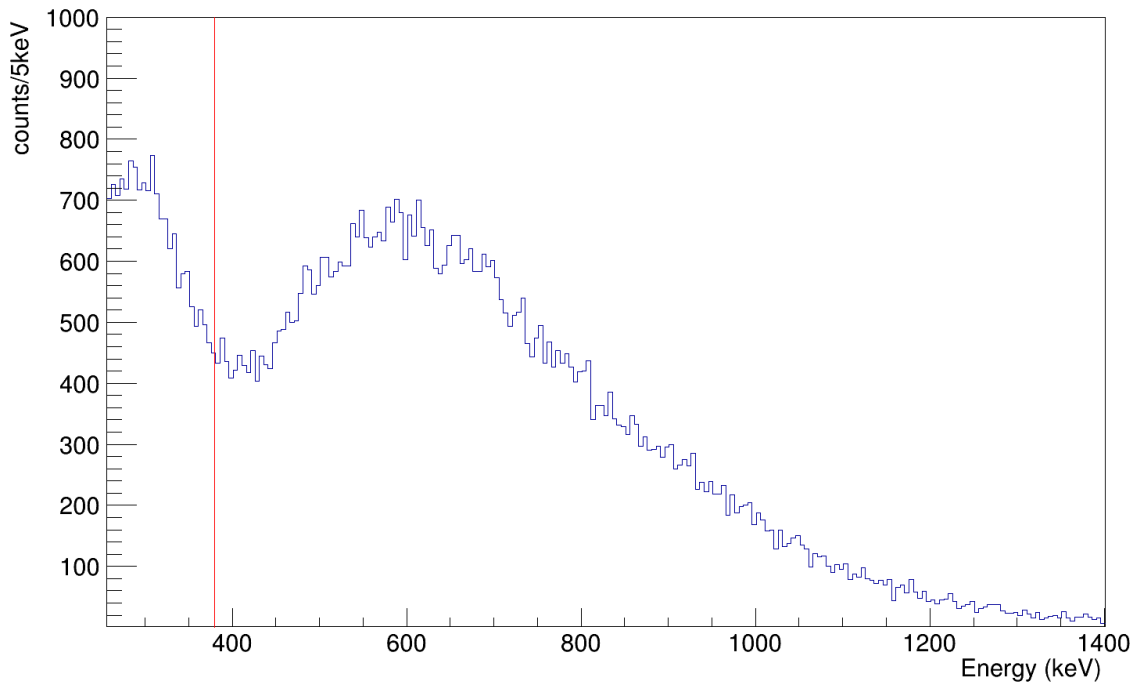


Figure 4.5: Energy spectrum for a sample strip from the ^{90}Sr calibration run. The software threshold for the sample strip is shown by the red line.

In addition to the energy calibration, low-energy thresholds need to be set for the BCS DSSD high-gain channels since the hardware thresholds are set low enough that they will trigger on some edge of the noise peak. As for the SSSD, the software thresholds are set based on the electron spectra from the β -decay of a ^{90}Sr source. An energy spectrum from a sample strip for the ^{90}Sr decay is shown in Fig. 4.5 and includes a representative low-energy threshold.

While the low-gain channels of the BCS DSSD were not calibrated, gain-matching based on online beam data was used to align the energies of the individual strips. Similarly, the BCS scintillator light-particle threshold was determined based on the live beam spectrum. A summed spectrum of all the runs in the BCS portion of the experiment is shown in Fig. 4.6. This spectrum shows the expected characteristics of light-particle energies in the secondary

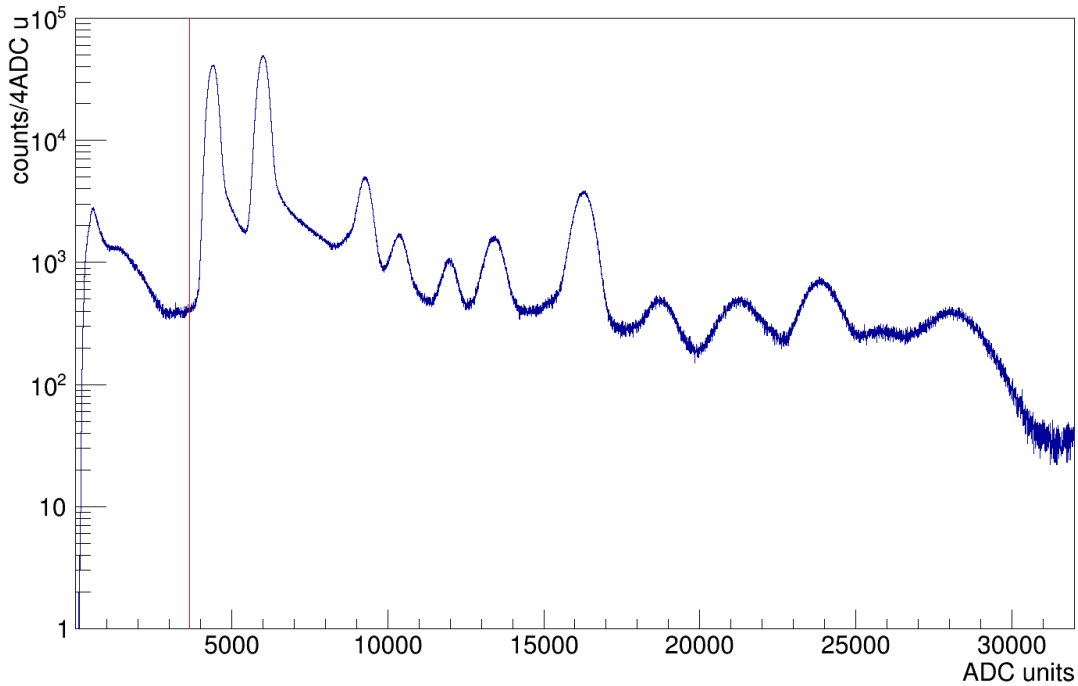


Figure 4.6: Energy spectrum for the BCS scintillator light-particle veto for the entire BCS portion of the beam time. The software threshold for the sample strip is shown by the red line. A decay event requires that the signal in the scintillator is < 3650 ADC units or else is rejected as a light-particle event. Note that this spectrum only shows non-zero scintillator signals.

beam. Though the exact energy is not calibrated for the scintillator, a cut is applied based on this spectrum, which discriminates light-particle signals (which can mimic β -decay signals in the silicon detectors) from true β -decay events.

4.1.2 NERO

Determining the NERO detector efficiency requires a neutron source with a well-documented activity. Here a ^{252}Cf source produced in December 1989 and with an activity most recently observed in October 2014 was placed in the center of the NERO array and data from the four quads was collected over the course of a several hour calibration run. A subsequent

run then collected data with only room background neutron sources. The total background-subtracted neutron rate in the calibration data was then compared with the known activity of the source, determining the overall efficiency of NERO.

^{252}Cf ($T_{1/2} = 2.645\text{ yr}$) produces neutrons via spontaneous fission, with a fission branching rate of 3.102% and 0.116 neutrons per decay [53], while the remainder α decays to ^{248}Cm ($T_{1/2} = 3.48 \times 10^5\text{ yr}$). The original composition of the source used here is listed in Tab. 4.1 and includes other Cf isotopes including the neutron emitter ^{250}Cf ($T_{1/2} = 13.08\text{ yr}$, SF=0.077%, n/d=2.71e-3 [54]). Over time, the ^{252}Cf decays away, and the neutron intensity of the source decreases considerably. The remaining ^{250}Cf then accounts for a greater proportion of the overall neutron activity. Tab. 4.1 additionally shows the isotopic composition at the 2014 activity measurement date, as well as the composition on the day of the calibration for this experiment, which was extrapolated from the 2014 measurement via exponential decay curves with the known half-lives. The total neutron activity from the source used is determined to be 147.1 n/s.

Neutron signals in the NERO counters have characteristic spectra for both the ^3He and the BF_3 counters, exemplified in the sample spectra shown in 4.7. The limits of the spectra used to defined neutron events are determined for each counter to include the entire range of neutron signals while excluding the low energy noise peak. The spectra are then each integrated over the designated ranges and the sum total of all the counters is the total number of neutrons observed by NERO.

This sum total is determined for both a ^{252}Cf source run, as well as a blank room background run. The efficiency of NERO is given by:

$$\epsilon_n = \frac{n_{true}}{n_{emit}} = \frac{n_{obs} - n_{bg}}{n_{emit}} \quad (4.1)$$

	1 December 1989	16 October 2014	22 March 2019 (calc.)	
Nuclide	Amount (%)	Amount (%)	Amount (%)	Neutron Activity (s^{-1})
^{249}Cf	7.32	6.972	6.913	0
^{250}Cf	13.11	3.506	2.772	39.3
^{251}Cf	4.55	4.463	4.449	0
^{252}Cf	75.02	0.110	0.035	103.8
^{245}Cm	0	0.351	0.412	0
^{246}Cm	0	9.583	10.313	0.1
^{247}Cm	0	0.087	0.102	0
^{248}Cm	0	74.907	75.004	3.9
Total	100	100	100	147.1

Table 4.1: Table showing the original isotopic composition of the ^{252}Cf source, along with the 2014 calculated composition based on the activity, and finally the extrapolated composition on the day of the calibration for this experiment. Table updated from [1].

Quad	n_{obs}	n_{bg}	n_{true}	n_{emit}	Efficiency
A	606635	46934	559701	1957363	29%
B	594682	46382	548300	1957363	28%
C	591207	39703	551504	1957363	28%
D	581411	31726	549685	1957363	28%
Total	2373935	164745	2209190	7829452	28%

Table 4.2: Table showing the observed source, background, and background subtracted source neutron rates, and the overall efficiency calculated using the extrapolated ^{252}Cf neutron activity from Tab. 4.1

where n_{obs} is the total observed neutron events in NERO during the source run, n_{bg} is the total observed neutron events in NERO for a background run, and n_{emit} is the total neutrons emitted by the ^{252}Cf source during the source run. The counts are shown in Tab. 4.2 and the resulting efficiency of NERO is 28(3)%. The error is primarily systematic, due in part to the extrapolation in determining the source composition from a then 5 year-old measurement. This is comparable, though slightly lower than the benchmark NERO ^{252}Cf efficiency of 31.7(2)% [55]. The discrepancy is in part due to uncharacteristic noise in the outermost BF_3 tubes which forced higher thresholds to be employed and contributed to the lower overall efficiency.

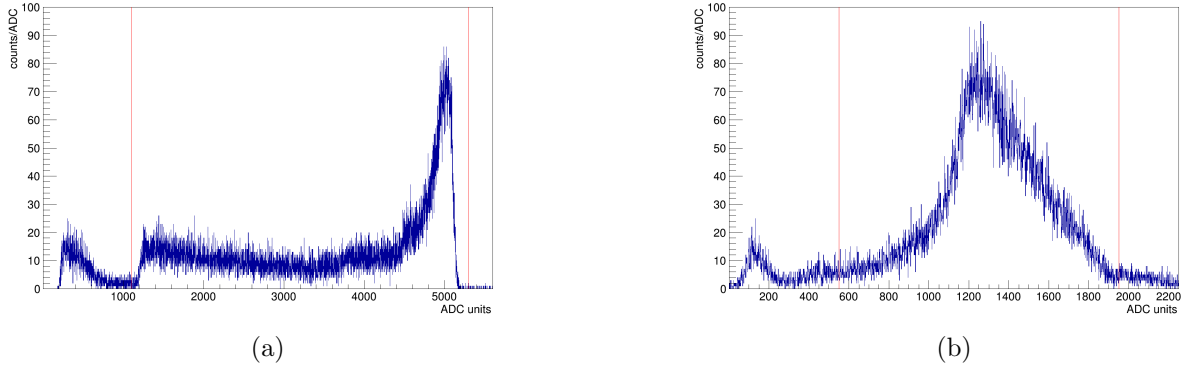


Figure 4.7: Sample spectra for the NERO neutron counting tubes. Fig. 4.7a shows a ^3He counter and Fig. 4.7b shows a BF_3 counter. Visible in both spectra is the low energy noise peak, along with the designated upper and lower limits (red vertical lines) of a neutron signal for these tubes. Only signals within the red bounds were considered neutron events, and the bounds are set for each tube individually.

4.1.3 SuN

As the SuN setup utilized the same upstream PIN detectors as the BCS, the PIN calibration from Sec. 4.1.1 applies for the SuN portion as well. This leaves the SuN PMTs, DSSD, and veto for calibration.

4.1.3.1 SuN PMTs

A background run is first taken in order to establish a constant background spectrum and to gain match the individual PMTs of SuN using the naturally occurring 1.460 MeV γ -ray from the electron-capture decay of ^{40}K to ^{40}Ar [56]. Fig. 4.8 shows the results of this gain matching across all 24 PMTs, with each spectrum showing the low-energy background peak in addition to the ^{40}K peak.

With the individual PMTs gain matched, the tubes are summed to comprise the 8 segments of the SuN detector and each of these is calibrated using a ^{241}Am , ^{137}Cs , and ^{60}Co source. The resulting points are linearly fit to the known γ -ray energies each of these iso-

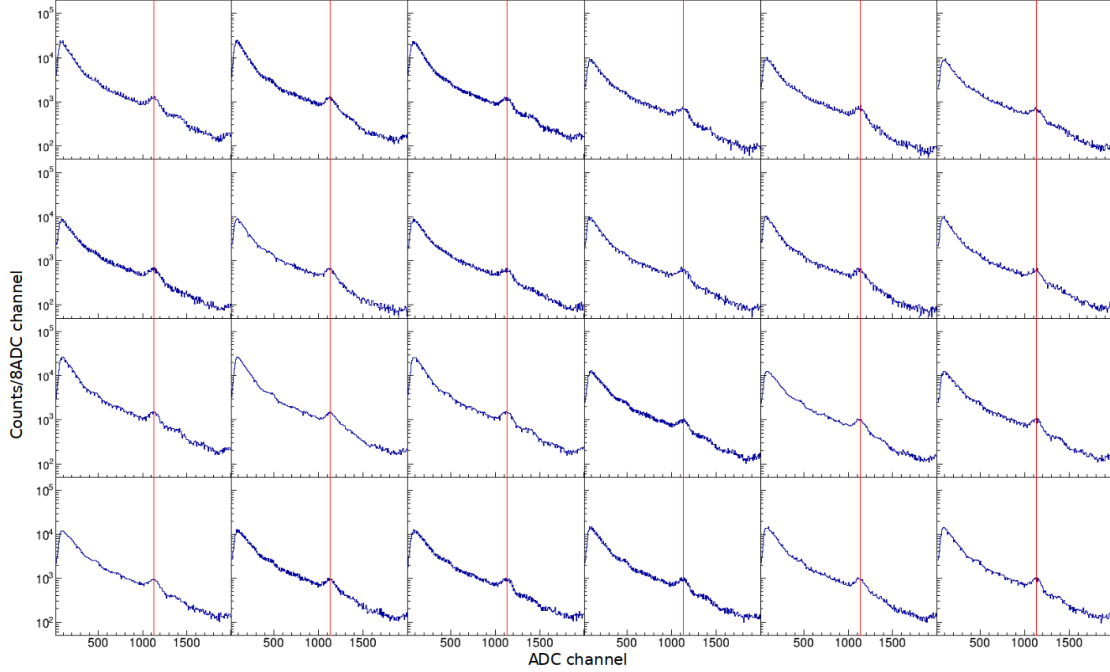


Figure 4.8: Histograms of the individual PMTs in SuN for a background run. A vertical line is drawn through the ^{40}K γ -ray peak—around 1100 ADC units—to which all of the PMTs are gain matched.

topes emit, respectively 59.5, 662, 1173 and 1332 keV respectively (^{60}Co accounts for the final two). The residuals from this linear fit are shown in Fig. 4.9. The individual spectra for each of the sources is discussed in further detail in Ch. 3.

Following the completion of the experiment, the same calibration source runs were conducted and the residuals from applying the pre-experiment calibration to the post-experiment source data is shown in Fig. 4.10. The post-experiment residuals are within the 25 keV binning width applied to the SuN spectra in Ch. 5, and so the same linear calibration was maintained across the SuN experimental runs.

4.1.3.2 SuN DSSD

As with the BCS DSSD, the SuN DSSD high-gain signals were calibrated with a ^{228}Th source. A spectrum from a sample strip showing the first four peaks is shown in Fig. 4.12.

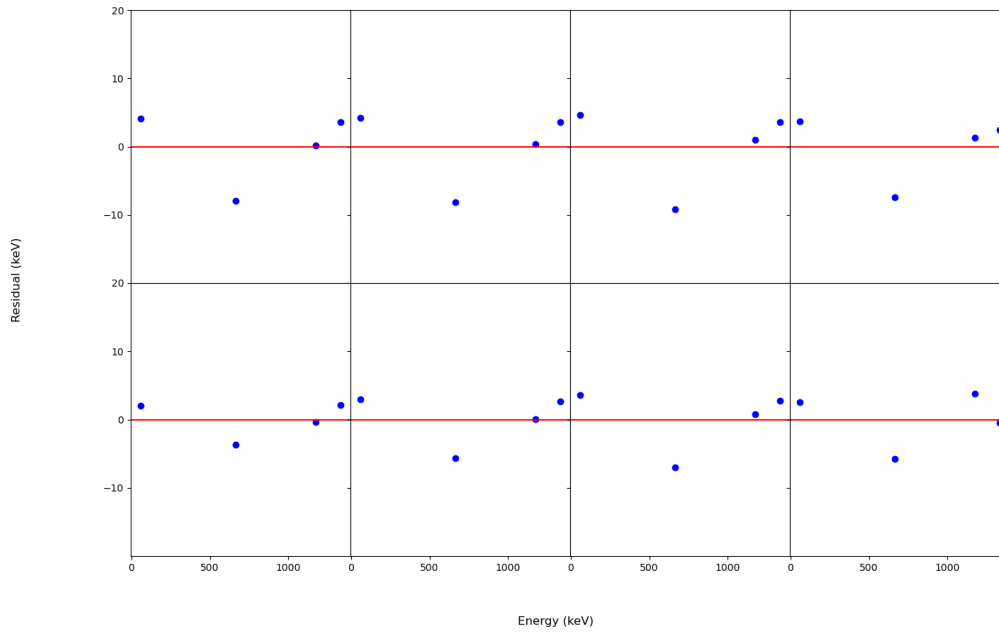


Figure 4.9: Residuals of the linear fit of the eight SuN segments to the calibration γ -rays from ^{241}Am , ^{137}Cs , and ^{60}Co .

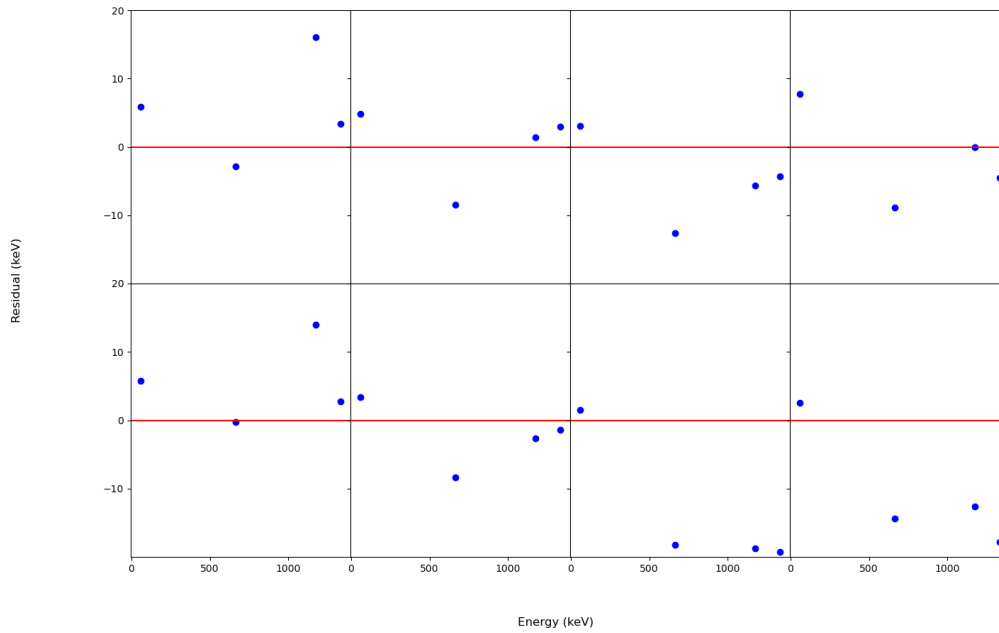


Figure 4.10: Residuals of the post-experiment calibration using the pre-experiment linear fit of the eight SuN segments to the calibration γ -rays from ^{241}Am , ^{137}Cs and ^{60}Co .

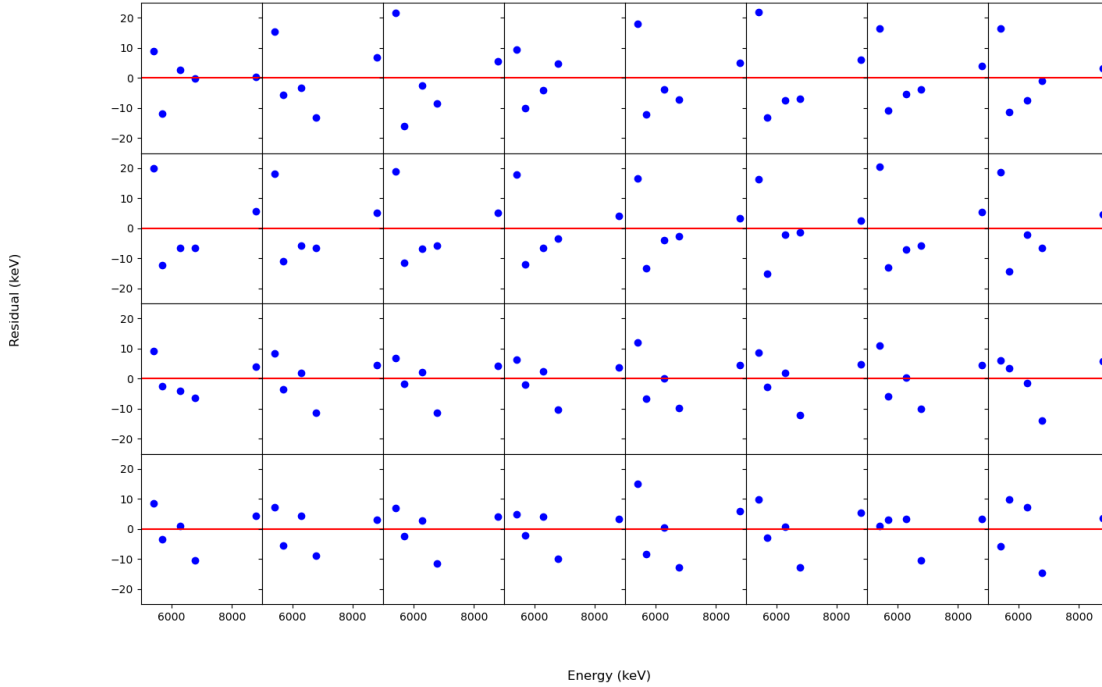


Figure 4.11: Residuals of the linear calibration of the SuN DSSD strips to the ^{228}Th source data.

These calibrations produced varied resolutions by strip of the silicon detector but for the 6.778 MeV energy, every strip had an energy resolution below 3%. Collectively, these four or five energy peaks were used to calibrate each strip of the detector using a linear fit, the residuals of which are shown in Fig. 4.11. Additionally, high-gain low-energy software thresholds were set using a ^{90}Sr source run as with the BCS DSSD. The low-gain channels of the SuN DSSD were not calibrated, but gain-matching based on online beam data was used to align the energies of the individual strips.

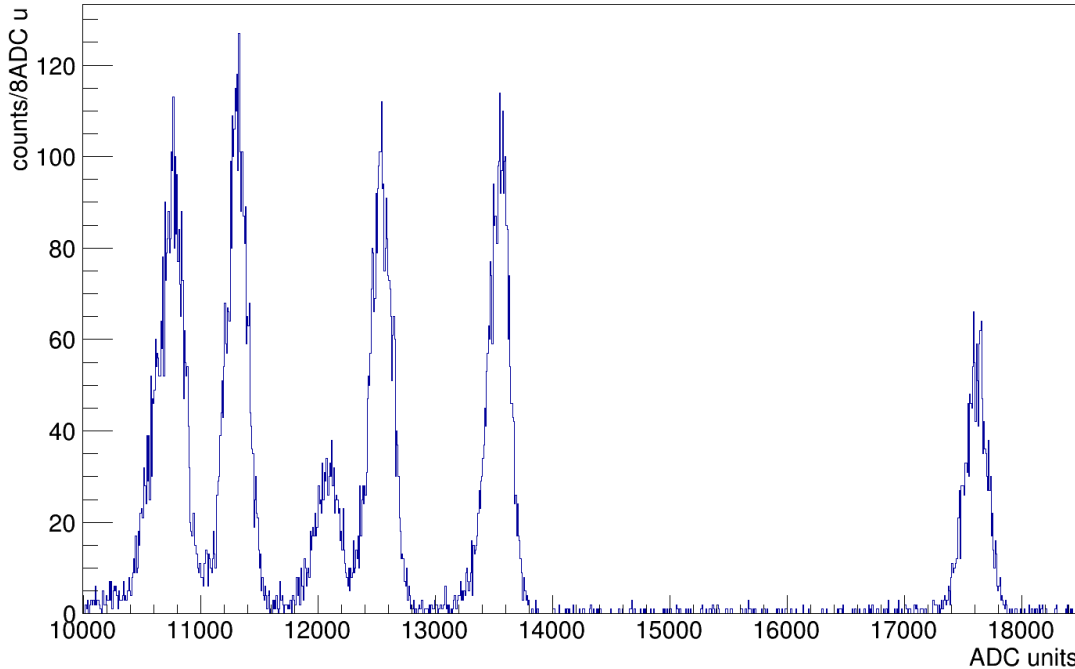


Figure 4.12: Energy spectrum for a sample strip from the ^{228}Th calibration run.

4.2 Particle Identification

As described in Sec. 2.2.1, the δE -TOF method is employed to separate implantation events into different isotopes. The energy deposited in the upstream PIN02 detector is the δE , and the TOF is measured as the time difference from the start at the PIN02 detector to the time-delayed stop at the I2S scintillator. Notably, as outlined in [41], the raw TOF is dependent on the momentum of the specific beam particle. Thus, a momentum correction is employed based on the position of the particle on the I2 scintillator. The results are shown in Fig. 4.13 for the BCS-NERO setup, and Fig. 4.15 for SuN.

Additionally, as is most evident in Fig. 4.15, a background “shadow” of particles between individual isotope clusters exists, particularly between the highest intensity isotopes, e.g. between $^{57-58}\text{Ti}$ or $^{58-59}\text{Ti}$. This was determined at the end of the experiment to be due to low

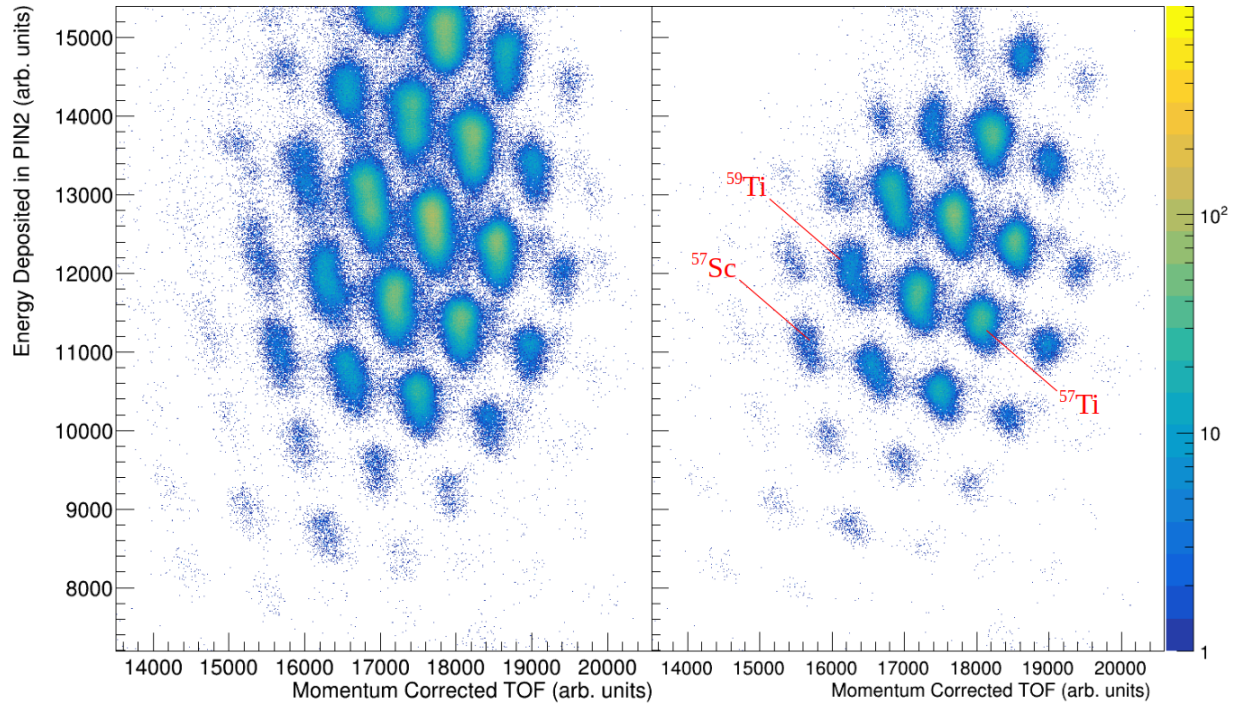


Figure 4.13: Particle ID (δE -TOF) plots for the BCS-NERO portion. Left shows all the beam particles that passed through the upstream PINs, right is the same but cut to only the particles successfully implanted in the DSSD.

trigger thresholds in the I2 scintillator, and was confirmed in the final runs of the experiment when the thresholds were increased. These shadows introduce additional background, and so cuts were applied on the particle ID plot to reduce their contribution as much as possible (Figs. 4.14, 4.16).

4.3 Correlations

Defined physics events (Sec. 2.3.4) such as a particle decay in a DSSD need to be correlated with the implantation event of the parent beam particle in order to identify the parent isotope. This is done after applying all the calibrations and thresholds described in Sec. 4.1. Implantation events are constructed by grouping the upstream detectors for particle

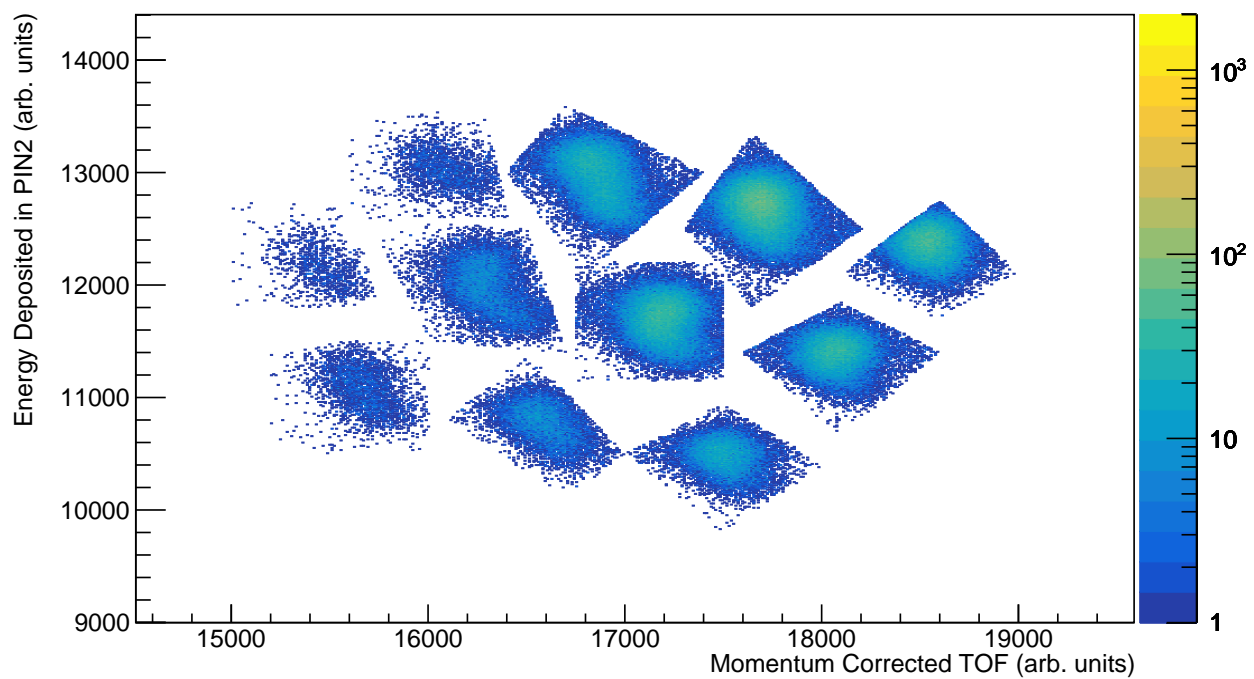


Figure 4.14: Particle ID (δE -TOF) plots for the BCS-NERO portion, cut on isotopes of interest. From left to right, top to bottom: ^{62}V , ^{61}V , ^{60}V , ^{59}V , ^{60}Ti , ^{59}Ti , ^{58}Ti , ^{57}Ti , ^{57}Sc , ^{56}Sc , ^{55}Sc .

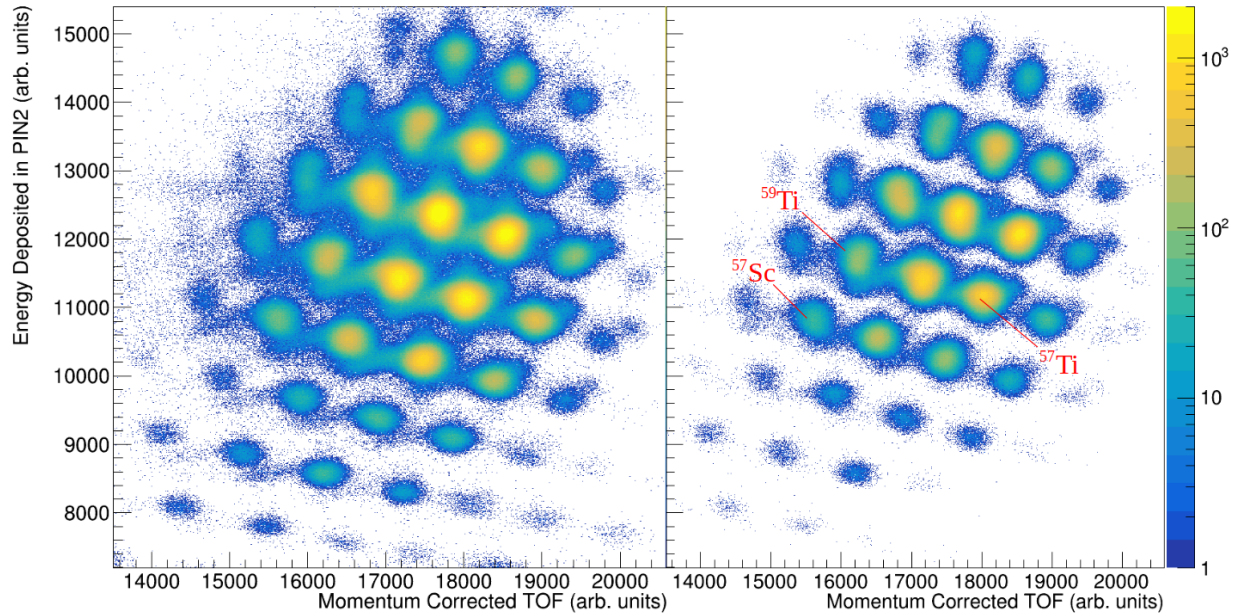


Figure 4.15: Particle ID (δE -TOF) plots for the SuN portion. Left shows all the beam particles that passed through the upstream PINs, right is the same but cut to only the particles successfully implanted in the DSSD. The visible “shadow” between some isotopes is due to trigger thresholds in the I2 scintillator. Particle cuts are applied in order to reduce the contribution from these events.

identification with the low-gain signals in the DSSD. The successful implantation events are stored and subsequent decay events within a specified spatial and temporal window are correlated to the implantation.

4.3.1 Event Logic

Events are classified into either implantation or decay events. If an event does not fit the criteria for either of these event types it is not further considered in the analysis.

4.3.1.1 Implantation Events

Given the detector setup described in Sec. 2.2, an implantation event for the BCS arrangement can be defined as an event which passes the following criteria after all calibrations and

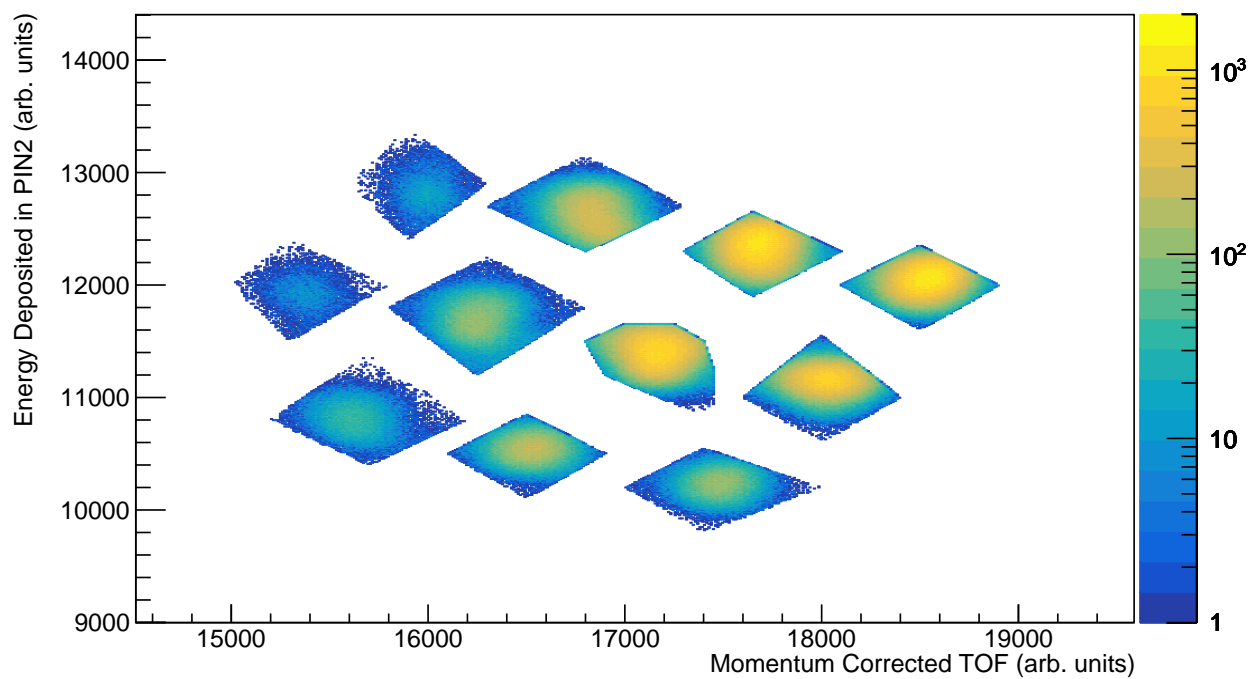


Figure 4.16: Particle ID (δE -TOF) plots for the SuN portion, cut on isotopes of interest. From left to right, top to bottom: ^{62}V , ^{61}V , ^{60}V , ^{59}V , ^{60}Ti , ^{59}Ti , ^{58}Ti , ^{57}Ti , ^{57}Sc , ^{56}Sc , ^{55}Sc .

thresholds are applied:

1. $E_PIN01 > 0$
2. $E_PIN02 > 0$
3. $E_BCS_DSSD_low_gain_front > 0$
4. $E_BCS_DSSD_low_gain_back > 0$
5. $E_BCS_SSSD < overflow$

Plainly, the conditions require that a beam particle is read as depositing energy through both upstream PIN detectors, as well as a single strip from both sides of the low-gain channels of the BCS DSSD, but not in the BCS SSSD. As the BCS SSSD only outputs a high-gain signal, any beam particle passing through it or implanting in it would deposit enough energy to cause an overflow.

The conditions for the SuN setup are similar:

1. $E_PIN01 > 0$
2. $E_PIN02 > 0$
3. $E_SuN_DSSD_low_gain_front > 0$
4. $E_SuN_DSSD_low_gain_back > 0$
5. $E_SuN_Veto = 0$

where the SuN veto detector takes the place of the BCS SSSD in validating that the beam particle did not punchthrough but was successfully implanted in the DSSD.

4.3.1.2 Decay Events

Again, given the detector setup described in Sec. 2.2, a decay event for the BCS arrangement can be defined as an event which passes the following criteria after all calibrations and thresholds are applied:

1. $E_PIN01 = 0$
2. $E_PIN02 = 0$
3. $E_BCS_DSSD_low_gain_front = 0$
4. $E_BCS_DSSD_low_gain_back = 0$
5. $E_BCS_DSSD_high_gain_front > 0$
6. $E_BCS_DSSD_high_gain_back > 0$
7. $E_BCS_Veto = 0$

Here, the conditions require that there is no beam particle depositing energy in any of the PINs or BCS DSSD. Additionally the BCS DSSD must have a positive, high-gain signal in both a front and back strip. Finally, the BCS scintillator veto needs to be below the light-particle signal energy.

The conditions for the SuN setup are similar:

1. $E_PIN01 = 0$
2. $E_PIN02 = 0$
3. $E_SuN_DSSD_low_gain_front = 0$
4. $E_SuN_DSSD_low_gain_back = 0$

5. $E_SuN_DSSD_high_gain_front > 0$

6. $E_SuN_DSSD_high_gain_back > 0$

7. $E_SuN_Veto = 0$

where the SuN veto detector serves as the light particle veto, in addition to the implantation validation.

If an event is designated a decay event, the correlator checks if it is within a specified spatial and temporal correlation window with an implantation event in the DSSD and correlates it if so. The spatial window refers to the pixel location of the implantation event and decay event. For the BCS DSSD, a 5×5 pixel window was used, where a decay event can be up to two pixels away from the implantation event in both x and y and still be spatially correlated. The SuN DSSD used both a 1×1 and a 3×3 pixel window depending on the isotope. The temporal window refers to the length of time after an implantation event that a decay can be temporally correlated with it. For both the BCS and SuN portions the temporal window was set to 2s in order to allow for daughter and subsequent isotopic generations to be included in the analysis.

In order to maximize statistics, implants were allowed to be correlated with multiple decays within the spatial or temporal window. This means that a large number of background decay events are correlated to a given implant, but the likelihood of successfully correlating a given implant with the true decay is increased. Tab. 4.3 shows the size of the total correlated data set for the isotopes of interest.

Isotope	BCS		SuN	
	Implants	Corr. Decays	Implants	Corr. Decays
⁵⁶ Sc	8115	11535	126809	105352
⁵⁷ Sc	2779	4604	30149	136576
⁵⁷ Ti	28590	36469	420852	180373
⁵⁸ Ti	40587	57469	554253	463925
⁵⁹ Ti	10488	15965	73223	46602
⁶⁰ Ti	1002	1595	4234	5116
⁵⁹ V	33109	42646	568672	394923
⁶⁰ V	62440	95340	505866	517050
⁶¹ V	34925	51985	115544	120477
⁶² V	2138	3448	4360	19194

Table 4.3: Table showing the total implants and correlated decays for the isotopes of interest. The correlator for ⁵⁷Sc, ⁶⁰Ti and ⁶²V for the SuN portion used a 3 × 3 spatial window, which accounts for the significantly increased relative number of correlated decays to implants over the other isotopes that used a 1 × 1 window.

4.3.2 Decay Curves

Having established a data set of correlated implantation and decay events, the decay time of a given correlated decay event can be determined by taking the time difference from implantation to decay. The histogram of all the decay times for a given isotope is then fit to determine the half-life of that isotope.

Radioactive decay is a probabilistic process, with a given species of isotope decaying to its daughter according to the differential equation:

$$\frac{dN(t)}{dt} = -\lambda N(t) \quad (4.2)$$

where N is the number of nuclei of the given isotope at time, t , and $\lambda = \ln(2)/t_{1/2}$ is the decay constant of the given isotope with half-life, $t_{1/2}$. The solution to the differential

equation then gives surviving nuclei N as:

$$N(t) = N(0)e^{-\lambda t} \quad (4.3)$$

and activity R :

$$R(t) = -\frac{dN}{dt} = \lambda N(0)e^{-\lambda t} = R(0)e^{-\lambda t} \quad (4.4)$$

where $N(0)$ is the initial amount of the parent isotope, and $R(0) = \lambda N(0)$ is the initial activity of the parent isotope. As the isotope decays the system of equations expands to include the daughter, neutron-daughter, and subsequent isotopes. This system is known as the Bateman equations [57], and has a general form described in [58] of

$$N_k(t) = \frac{N_1(0)}{\lambda_k} \sum_{i=1}^k \lambda_i e^{-\lambda_i t} \prod_{j=1, j \neq i}^k \frac{-\lambda_j}{\lambda_j - \lambda_i} \quad (4.5)$$

for the k -th isotope in a decay chain, and for the specific case considered here where the initial composition consists of only a single isotope. Eq. 4.5 is then modified to also include a neutron-daughter branch, with probability P_n . For the isotopes observed in this experiment, the half-lives of the great-granddaughter and neutron-great-granddaughter generations are much longer than the correlation time window of 2 s. As such only the parent, daughter, granddaughter, neutron-daughter and neutron-granddaughter isotopes are included in the decay curve fitting. No neutron branches are included beyond the parent, and are assumed to be negligible. Then, by combining Eqs. 4.4 and 4.5 for a system of parent, daughter,

granddaughter and specifying a branch to the neutron-daughter gives:

$$\begin{aligned}
R &= C_1 e^{-\lambda_1 t} \\
&+ (1 - P_n) \left(\frac{\lambda_2 C_1}{\lambda_2 - \lambda_1} \left(e^{-\lambda_1 t} - e^{-\lambda_2 t} \right) \right) \\
&+ P_n \left(\frac{\lambda_{2n} C_1}{\lambda_{2n} - \lambda_1} \left(e^{-\lambda_1 t} - e^{-\lambda_{2n} t} \right) \right) \\
&+ \frac{(1 - P_n) \lambda_2 \lambda_3 C_1}{(\lambda_2 - \lambda_1) (\lambda_3 - \lambda_1)} e^{-\lambda_1 t} + \frac{(1 - P_n) \lambda_2 \lambda_3 C_1}{(\lambda_1 - \lambda_2) (\lambda_3 - \lambda_2)} e^{-\lambda_2 t} + \frac{(1 - P_n) \lambda_2 \lambda_3 C_1}{(\lambda_3 - \lambda_1) (\lambda_3 - \lambda_2)} e^{-\lambda_3 t} \\
&+ \frac{P_n \lambda_{2n} \lambda_{3n} C_1}{(\lambda_{2n} - \lambda_1) (\lambda_{3n} - \lambda_1)} e^{-\lambda_1 t} + \frac{P_n \lambda_{2n} \lambda_{3n} C_1}{(\lambda_1 - \lambda_{2n}) (\lambda_{3n} - \lambda_{2n})} e^{-\lambda_{2n} t} + \frac{P_n \lambda_{2n} \lambda_{3n} C_1}{(\lambda_{3n} - \lambda_1) (\lambda_{3n} - \lambda_{2n})} e^{-\lambda_{3n} t} \\
&+ B \\
&= R_1 + R_2 + R_{2n} + R_3 + B
\end{aligned} \tag{4.6}$$

where C_1 is the initial activity of the parent nuclei, R_i is the activity of the i -th nuclei, and B is the constant background rate. For the isotopes of interest in this work, daughter decay constants, $\lambda_i, i > 1$, were experimentally known from previous work, and with the P_n values being determined separately from the NERO data (Sec. 4.4), leaves only three parameters to fit: the parent decay constant λ_1 , the initial parent activity C_1 , and the constant background rate B . These parameters are fit to the decay curve histogram via a χ^2 minimization using the TMinuit package in ROOT. A sample fit is shown for ^{57}Ti in Fig. 4.17.

4.4 P_n Calculation

For the BCS/NERO portion of the experiment, a β -n event is defined as a correlated decay event with a coincident neutron signal in NERO within the 200 μs coincidence window. Gating the decay curve on these events gives a clear indication of isotopes with significant

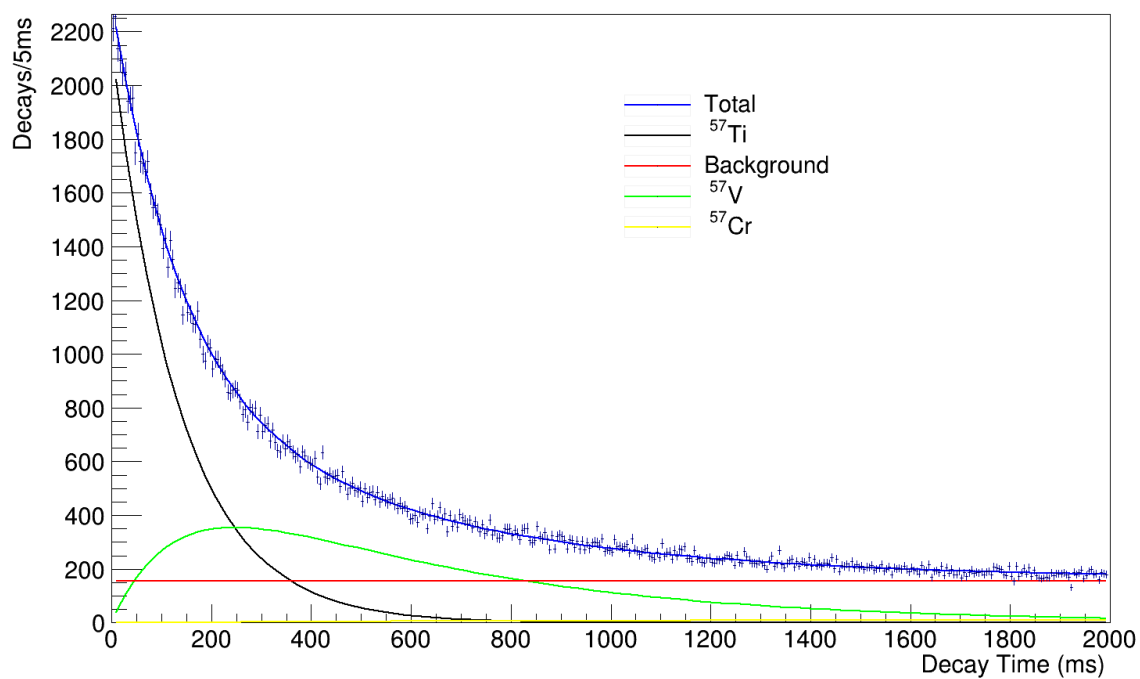


Figure 4.17: Decay time plot including parent, background, and all daughter decay curves from ^{57}Ti correlated decays. Neutron-daughter decays are not included here as the P_n was determined to be negligible.

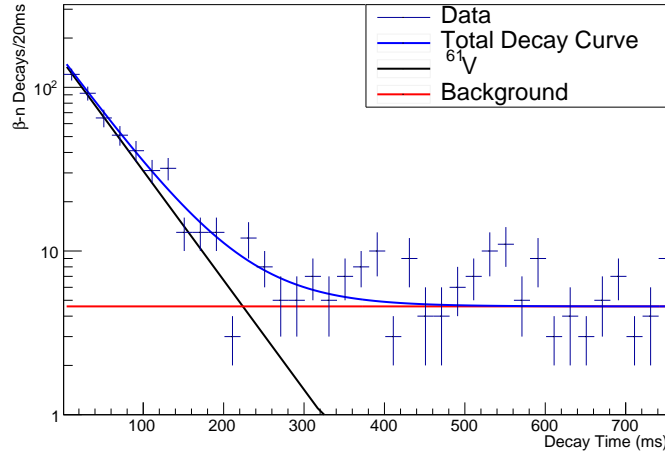


Figure 4.18: Neutron-gated decay time plot for ^{61}V . Only the parent and a flat background is included in this fit.

P_n branchings. For example, the neutron-gated decay curve of ^{61}V is shown in Fig. 4.18. The P_n for ^{61}V is known from previous experiments to be 14.5(2.0)% with a half-life of 48(2) ms [26]. As none of its daughters are known to emit neutrons, gating on neutron events leaves only the parent ^{61}V β -n events and a flat background. Fitting this with a similar method as the total decay curves (Sec. 4.3.2), the neutron-gated decay curve then gives an estimate for the half-life which is independent of daughter half-lives. This fit is only performed for the isotopes which are measured to have appreciable P_n values.

The P_n of a given isotope is calculated by comparing observed counts of β -n decays with several potential complicating factors. A β -n coincidence can be a true β -n event, but can also be a false β randomly correlated with a true n, a false n randomly correlated with a true β or a false β randomly correlated with a false n. In order to account for these possibilities various estimates are needed. There are 1 161 536 total observed neutron events—whether background or beam-induced—giving an overall rate for the BCS portion of 26.285 n/s or one neutron observed every 38 ms. Noting the 200 μs correlation window used for the BCS portion, and assuming the neutron rate to be roughly constant, there is then a 0.53% chance

of randomly correlating a neutron event for an average 200 μs window. This probability is then incorporated into the P_n calculation.

For a given isotope, a decay time window T is selected, and the P_n is calculated based on the following:

$$P_n = \frac{D_{true,\beta-n}\epsilon_\beta}{D_{true,\beta}\epsilon_{\beta-n}\epsilon_n} \approx \frac{1}{\epsilon_n} \sum^T \frac{(D_{forw,\beta-n} - P_{rand,n}D_{forw,\beta} - D_{rev,\beta-n})}{D_{true,\beta}} \quad (4.7)$$

where $D_{true,\beta}$ is the estimated number of β -decays of the parent isotope, $D_{forw,\beta-n}$ is the number of forward-time correlated β -n events, $P_{rand,n}$ is the probability of correlating a random n event with a β -decay, $D_{forw,\beta}$ is the number of total observed β -decays of all isotopes, $D_{rev,\beta-n}$ is the number of reverse-time correlated β -decays, and ϵ_n is the efficiency of NERO. Additionally, the efficiencies for detecting a β and β -n event— ϵ_β and $\epsilon_{\beta-n}$ —are here assumed to be equivalent and cancel. Finally, while the values $D_{forw,\beta}$, $D_{forw,\beta-n}$, and $D_{rev,\beta-n}$ are all simply the number of corresponding correlated events in a given time window, $D_{true,\beta}$ is determined by integrating the fit parent decay curve (Sec. 4.3.2) over the given time window to estimate the total number of parent events in the data. For all isotopes, the window T is set to be four parent half-lives.

Reverse-time correlated events are determined by running the correlator backwards in time, correlating random decays to implantations. This is done in order to estimate the background rate for the observables. As the background decay rate is constant throughout the experiment, background events will be unaffected by the forward or reverse time correlator [59]. However, true decay events do not appear in backwards correlation, and so the correlations generated are purely background, and can be directly subtracted from the forward correlated events. The reverse correlation is used to estimate the background for

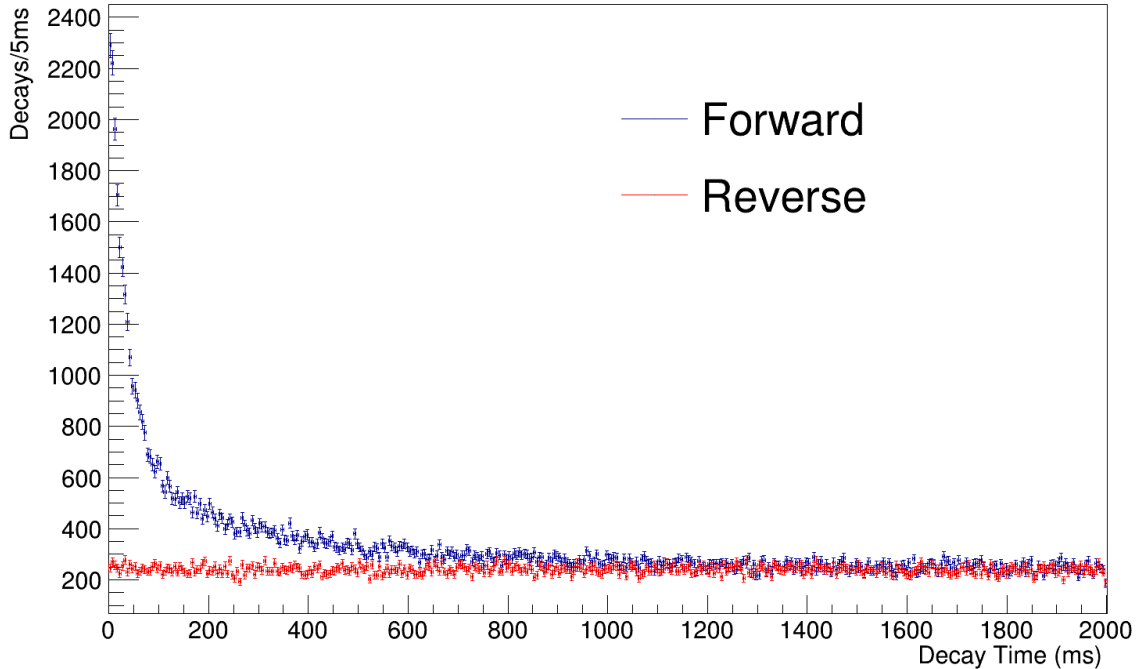


Figure 4.19: Comparison of time between implant and decay for forward and reverse correlated decays for ^{57}Sc decays in the SuN portion.

neutron events as well as the γ -ray spectra. An example of this subtraction is shown in Fig. 4.19 for the decay time curve of ^{57}Sc decays in the SuN setup. The forward decays display a characteristic exponential decay curve, while the reverse-time correlated events appear constant for all decay times.

4.5 Daughter Feeding

As briefly introduced in Ch. 3, the feeding intensities from each parent isotope to its daughter are determined by first, simulating the detector response to β -delayed γ -ray emission to each level in the level scheme of the daughter isotope. Second, the TAS, SS, multiplicity, and multiplicity-gated SS distributions are extracted from these simulations and rebinned to match the observed experimental data. Finally, a linear combination of all the levels is fit to

match the distributions in the observed data. The construction of the level scheme and the individual templates is described in Secs. 3.1.2, 3.2. The templates contain identically structured data as the observed data and so each observed spectra can likewise be constructed from the simulated data. The set of spectra observed by the SuN detector (hereafter collectively the “observables” or the “observable distributions”) incorporated into the fit are the following:

1. TAS
2. SS
3. Multiplicity
4. SS, gated on multiplicity = 1
5. SS, gated on multiplicity = 2
6. SS, gated on multiplicity = 3
7. SS, gated on multiplicity = 4

Each of the observables is extracted for each level in the level scheme or quasi-continuum, and linearly fit via a χ^2 minimization to the data as prescribed by the minimization:

$$\hat{\beta} = \arg \min_{\beta} \sum_k^K \left(\sum_i^I \frac{(y_{ik} - \sum_j^J \beta_j x_{ijk})^2}{\sigma_{ik}^2} \right) \quad (4.8)$$

s.t. $\|\beta\|_1 = 1$

where $\hat{\beta}$ is the set of J feeding intensities which minimizes the summed χ^2 values for all K observables, across all bins I . y_{ik} is the content of the i -th bin of the k -th observable in the experimental data, with a corresponding experimental error σ_{ik} . x_{ijk} is the simulated counterpart of y_{ik} but for the j -th level template.

Chapter 5

Results

5.1 P_n Values

P_n values are determined for the isotopes $^{56-57}\text{Sc}$, $^{57-60}\text{Ti}$, and $^{59-62}\text{V}$. They are determined using the approach described in Sec. 4.4. The results, including the total number of observed decays as well as observed β -n events are shown in Tab. 5.1. Also shown are the half-lives determined by fitting the β -n events to an exponential decay curve plus a flat background. The fits are plotted with the observed data in Fig. 5.1.

While the energy of the β -delayed neutrons can, in principle, range from $0 < E_n < Q_\beta - S_n$, it is assumed (supported by arguments outlined in Sec. 2.2.3) that the energy distribution is skewed toward $E_n < 1 \text{ MeV}$. NERO has been designed for a relatively flat efficiency in this energy range. The remaining efficiency uncertainty from the unknown neutron energy is therefore small and included in the 37(5)% efficiency value determined in [38]. This nominal efficiency was scaled by the ratio of the measured ^{252}Cf efficiencies to $\epsilon_n = 32(5)\%$. The total observed decay events, and coincident neutron events are tallied for the forward- and reverse-correlated events and the P_n is calculated from these according to Eq. 4.7. The error on the P_n is primarily statistical due to the number of observed β -n events, with the statistical error dominating for all isotopes except ^{60}V and ^{61}V . Error bars on the half-lives extracted from the fit neutron-gated decay curves are statistical and

Isotope	Forward		Reverse		P_n (%)	$T_{1/2}$ (ms)
	Obs. β	Obs. β -n	Obs. β	Obs. β -n		
^{56}Sc	2137	40	427	6	6(3)	–
^{57}Sc	792	32	62	1	12(4)	21(2)
^{57}Ti	9498	96	3538	55	< 5	–
^{58}Ti	13862	125	2765	45	< 3	–
^{59}Ti	3263	54	379	3	4(2)	–
^{60}Ti	286	7	26	2	< 19	–
^{59}V	10267	157	328	54	3(2)	–
^{60}V	20500	507	5580	86	8(2)	85(25)
^{61}V	9909	445	2009	37	16(3)	40(3)
^{62}V	515	17	71	1	10(5)	18(4)

Table 5.1: Table showing the observed β decay and β -n decay events for both forward- and reverse-time correlated events, as well as the determined P_n value for the isotopes studied. Additionally, for the isotopes with a determined $P_n > 6\%$, the neutron-gated decay curve half-life is shown. Upper limits are given at a confidence level of 95%.

estimated based on the results of the fit from the MINUIT suite from ROOT. The P_n value of 16(4)% for ^{61}V —the only previously well-defined P_n of this group¹—is in good agreement with the previously measured value of 14.5(2.0)% from [26].

5.2 Decay Curves

Correlated β decay curves vs. time are plotted for each isotope for both the BCS-NERO and SuN portions of the experiment in Figs. 5.2-5.11. Each decay curve is fit according to Eq. 4.6, with the P_n set to the values in Tab. 5.1, and daughter and granddaughter half-lives set to the previously determined values listed in Tab. 5.3. With the P_n and daughter half-lives determined, the fit is evaluated on the free parameters: (1) initial activity; (2) parent half-life; and (3) flat background rate. The resulting half-lives and their statistical errors are shown in Tab. 5.2 for both portions of the experiment, as well as an estimate

¹[11] found that a small β -delayed neutron branch could not be ruled out in the decay of ^{59}V , and estimated a lower limit of $\approx 3\%$, which is consistent with the value of 3(2)% determined here

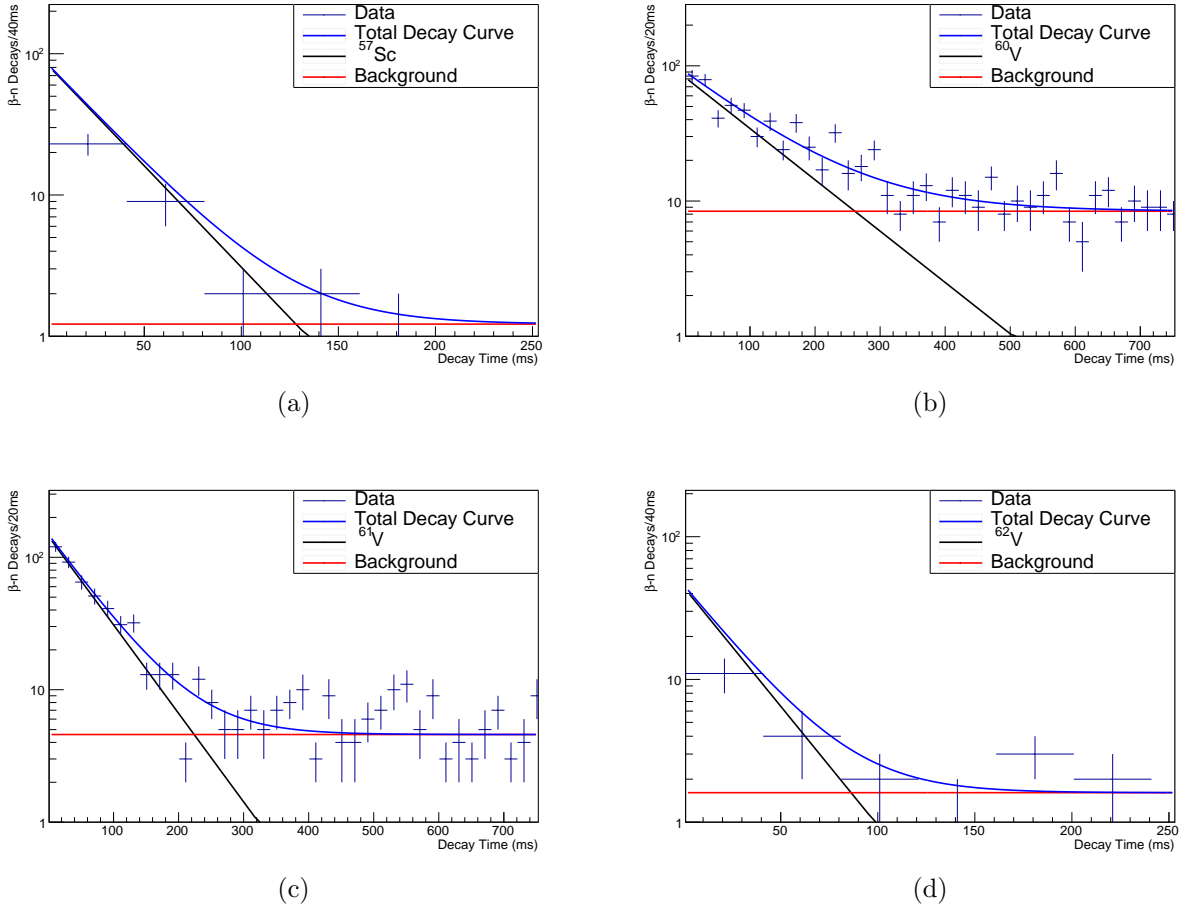


Figure 5.1: Neutron-gated decay curves for the (a) ^{57}Sc , (b) ^{60}V , (c) ^{61}V , and (d) ^{62}V isotopes.

of the total number of decays observed for each isotope. This is estimated by integrating the fit parent decay curve for the entire correlation window². The measured half-lives are internally consistent between the BCS and SuN portions, as well as consistent with previous measurements, with a few notable exceptions.

First, the previously reported ^{56}Sc half-lives are determined from two separate isomeric states [3], which were not distinguished in either the BCS or SuN fits, though the fit values do lie between the two proposed isomeric half-lives. Second, both the fit half-lives for ^{59}V fall

²Note this is integrated over the full 2000 ms correlation window. The number of parent decays in the four half-life window used in the P_n calculation can be calculated from this estimate and the corresponding parent half-life.

below the previous measurement. However, when the decay curve was gated on the 102 keV transition in the decay of ^{59}V to ^{59}Cr , a value of 96(1) ms was determined via a fit to an exponential with constant background, consistent with [11]. This may indicate the presence of some additional background that is not fully removed. Finally, while the BCS fit for ^{60}V is in line with previous measurements, the SuN value is significantly longer.

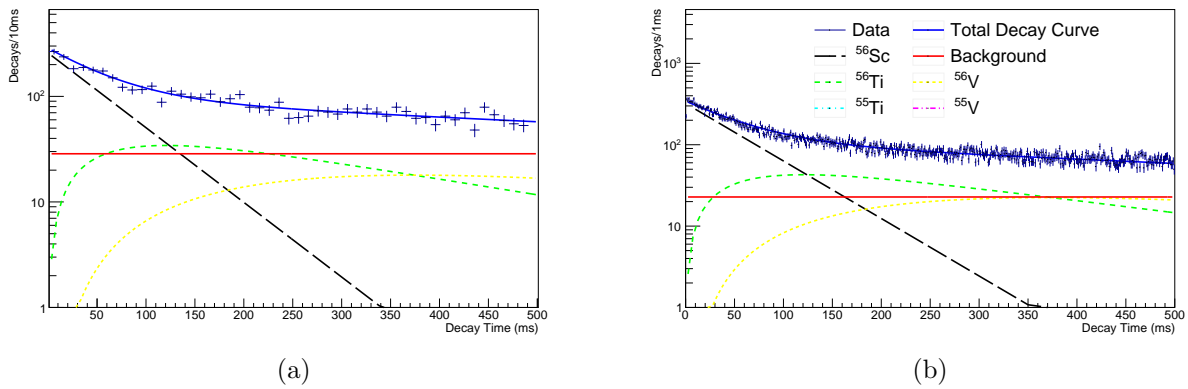


Figure 5.2: Decay curves for the ^{56}Sc isotopes for both the BCS-NERO (left) and SuN (right) portions. Legends are identical for both.

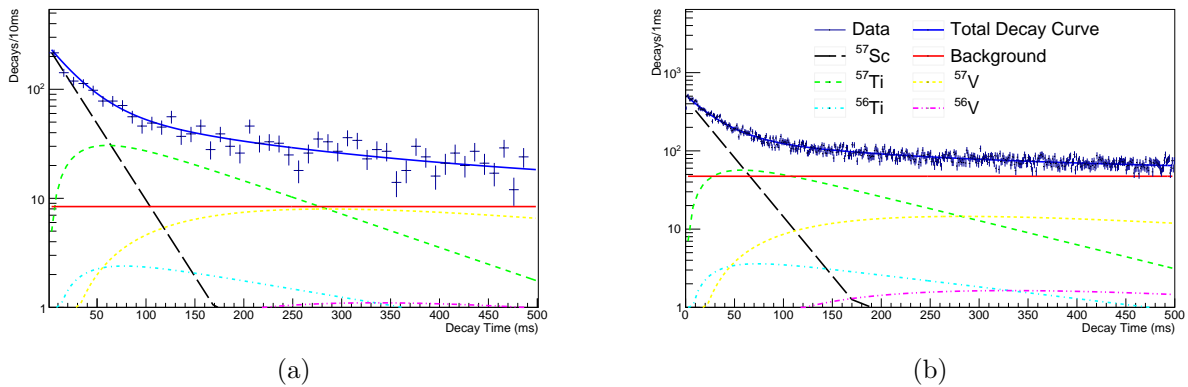


Figure 5.3: Decay curves for the ^{57}Sc isotopes for both the BCS-NERO (left) and SuN (right) portions. Legends are identical for both.

Isotope	Prev. $T_{1/2}$ (ms)	BCS		SuN	
		$T_{1/2}$ (ms)	Est. Decays	$T_{1/2}$ (ms)	Est. Decays
$^{56}\text{Sc}^*$	26(6),76(6)[3]	43(4)	1581	43(1)	19750
^{57}Sc	13(4)[28], 22(2)[3]	21(2)	752	20(1)	13393
^{57}Ti	98(5)[11]	95(7)	5394	94(1)	57895
^{58}Ti	59(9)[28]	53(2)	9672	52(1)	120892
^{59}Ti	30(3)[28]	31(2)	2486	26(1)	15861
^{60}Ti	22(2)[28]	21(4)	222	20(2)	972
^{59}V	97(2)[11]	82(5)	7000	91(2)	109634
^{60}V	68(4)[60]	69(3)	14247	77(1)	119940
^{61}V	47(1)[60], 48(1)[26]	46(2)	7748	46(1)	26570
^{62}V	33(2)[60]	31(4)	458	32(2)	1786

Table 5.2: Table showing previously measured half-lives, in comparison with the half-lives determined during the BCS and SuN portions of the experiment. Also shown are the total parent particles observed, estimated by integrating the fit decay curve from the half-life. ^{56}Sc was determined in [2] to beta decay from the ground state as well as a high-spin isomeric state to ^{56}Ti . Thus two half-lives were measured in [2, 3]. Here, the two states were fit to a single half-life. As the resolution of SuN was insufficient to distinguish the different ~ 1150 keV γ -rays.

Isotope	Prev. $T_{1/2}$ (ms)	Isotope	Prev. $T_{1/2}$ (ms)
^{55}Ti	1300(100) [61]	^{58}Cr	7000(300) [62]
^{56}Ti	200(5) [61]	^{59}Cr	1050(90) [11]
^{57}Ti	98(5)[11]	^{60}Cr	490(10) [63]
^{55}V	6540(150) [64]	^{61}Cr	233(11) [65]
^{56}V	216(4) [66]	^{62}Cr	209(12) [28]
^{57}V	350(10) [66]	^{58}Mn	3000(300) [62]
^{58}V	185(10) [66]	^{59}Mn	4590(50) [67]
^{59}V	97(2)[11]	^{60}Mn	280(20) [63]
^{60}V	68(4)[60]	^{61}Mn	710(10) [68]
^{56}Cr	5.94 min [69]	^{62}Mn	92(13) [28]
^{57}Cr	21100(1000) [70]		

Table 5.3: Table showing previously measured half-lives used for fitting daughter and grand-daughter decay curves.

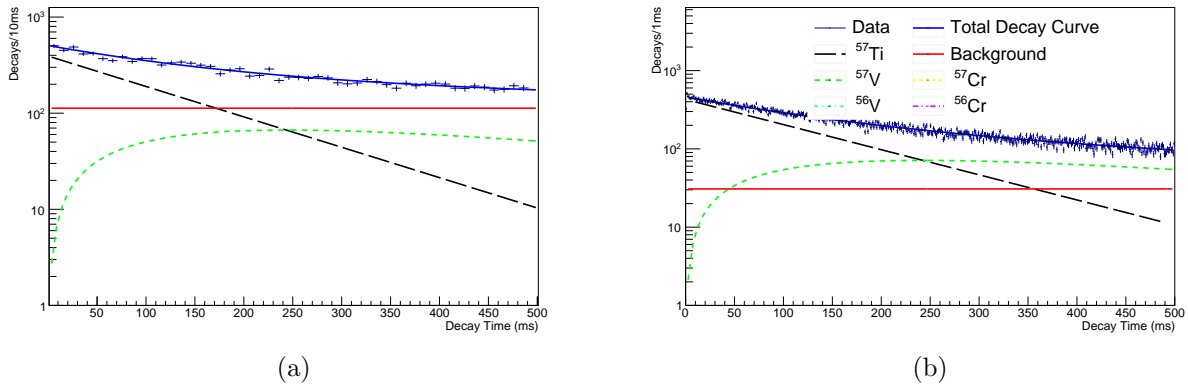


Figure 5.4: Decay curves for the ^{57}Ti isotopes for both the BCS-NERO (left) and SuN (right) portions. Legends are identical for both. In this 500 ms window, only the parent ^{57}Ti and daughter ^{57}V decays appear in appreciable amounts.

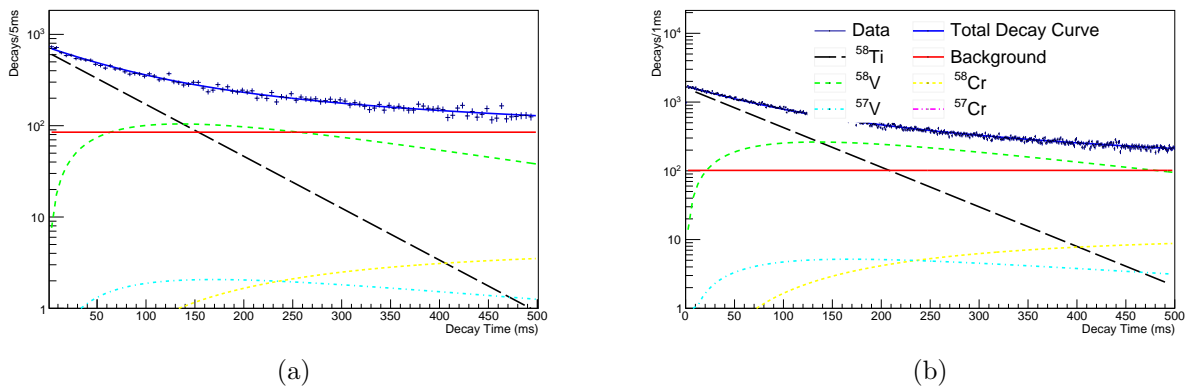


Figure 5.5: Decay curves for the ^{58}Ti isotopes for both the BCS-NERO (left) and SuN (right) portions. Legends are identical for both.

5.3 Gamma Analysis

5.3.1 ^{57}Ti Decay

The observable distributions from SuN are first background- and daughter-subtracted. For ^{57}Ti , the spectra are gated on the first 300 ms after implantation. This includes roughly three half-lives of ^{57}Ti ($T_{1/2} = 94(1)$ ms), but will also include ^{57}V ($T_{1/2} = 350(10)$ ms [66]) some contribution from daughter decays as well as a constant background. Background subtraction

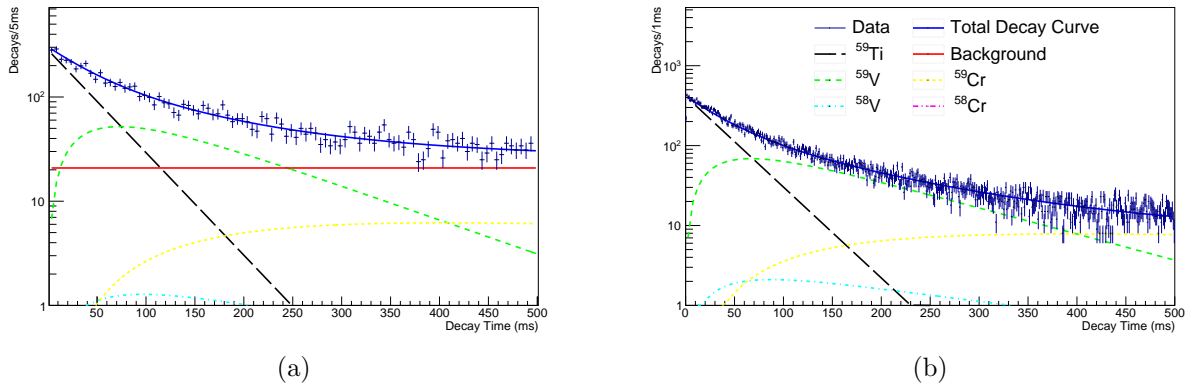


Figure 5.6: Decay curves for the ^{59}Ti isotopes for both the BCS-NERO (left) and SuN (right) portions. Legends are identical for both.

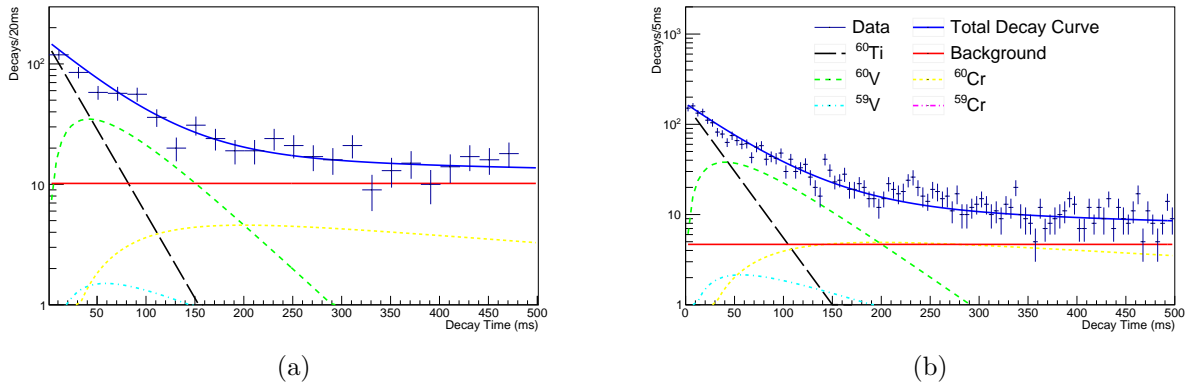


Figure 5.7: Decay curves for the ^{60}Ti isotopes for both the BCS-NERO (left) and SuN (right) portions. Legends are identical for both.

is done via the previously described reverse-time correlation method, and an example can be seen for the TAS in Fig. 5.12. Additionally, the ^{57}V daughter decay contribution to the TAS is removed by creating a daughter-decay TAS by gating the TAS on a late decay time window of 600–1200 ms. Because of its shorter half-life, the ^{57}Ti decay contribution is negligible in this time window, while the daughter decay is still significant. The long half-life of the granddaughter ^{57}Cr ($T_{1/2} = 21.1(10)$ s) means its contribution is negligible to either decay window. The small P_n of ^{57}Ti means neutron-daughter and neutron-granddaughter decays are also negligible. After applying again a reverse-time background subtraction, the

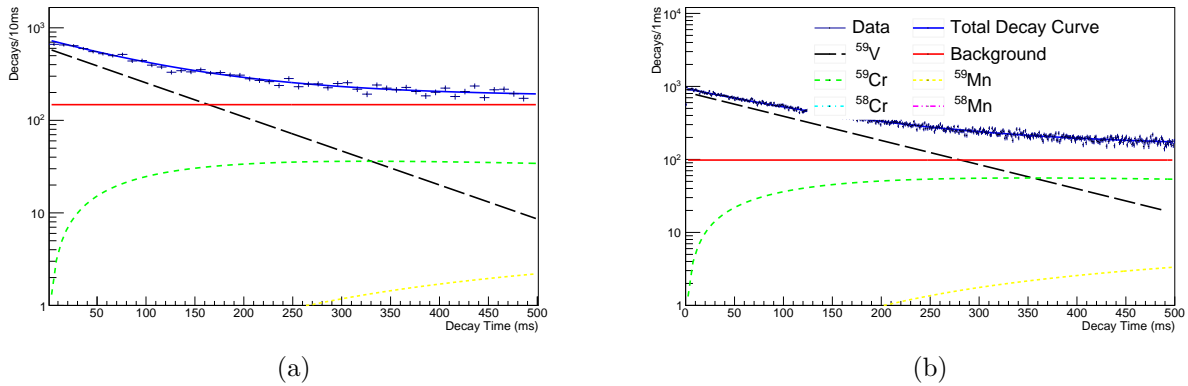


Figure 5.8: Decay curves for the ^{59}V isotopes for both the BCS-NERO (left) and SuN (right) portions. Legends are identical for both.

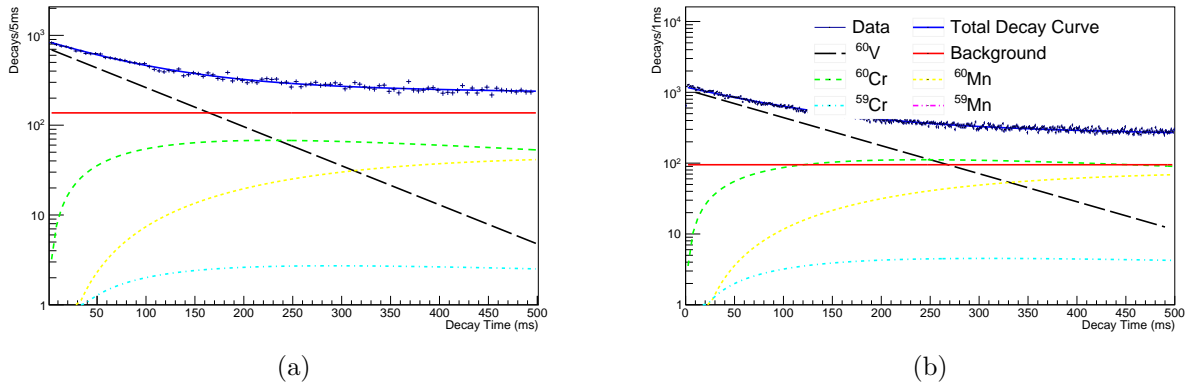


Figure 5.9: Decay curves for the ^{60}V isotopes for both the BCS-NERO (left) and SuN (right) portions. Legends are identical for both.

daughter-decay ^{57}V TAS is scaled by the expected ratio of $^{57}\text{V}:$ ^{57}Ti based on the decay curves and subtracted from the total TAS. This method is displayed in Fig. 5.13, where the peaks at 268 keV and 692 keV—known levels in the decay of ^{57}V to its daughter ^{57}Cr [66]—are removed from the TAS. The resulting final ^{57}Ti TAS spectrum (with error bars) is shown in Fig. 5.14. The same procedure is done for the SS (Figs. 5.15–5.16).

A previous study [11] using high resolution γ -ray spectroscopy measured the energies of a number of γ -rays associated with the β -decay of ^{57}Ti , and placed them in a proposed level scheme in ^{57}V shown in Fig. 3.4. Through the analysis described in Sec. 3.1, all the

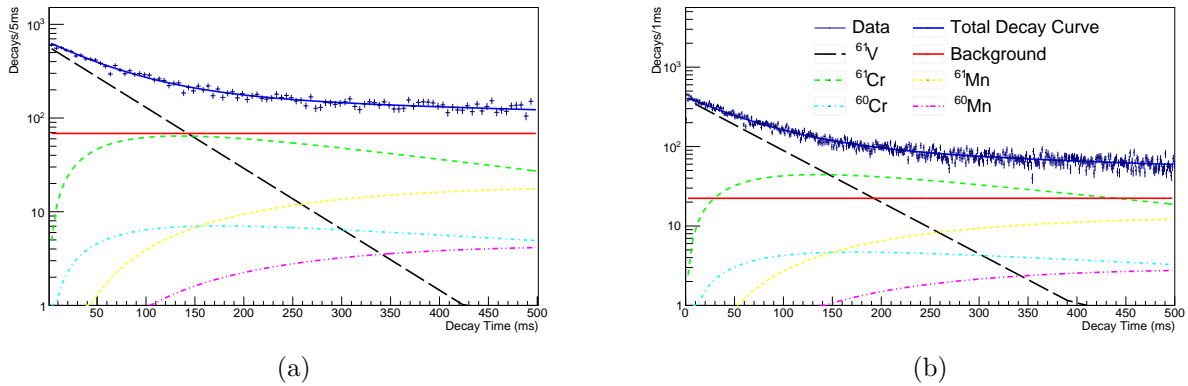


Figure 5.10: Decay curves for the ^{61}V isotopes for both the BCS-NERO (left) and SuN (right) portions. Legends are identical for both.

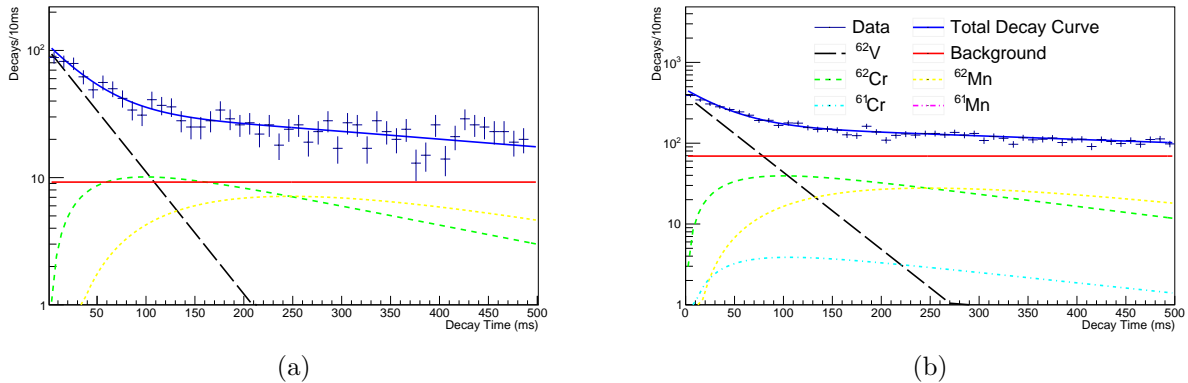


Figure 5.11: Decay curves for the ^{62}V isotopes for both the BCS-NERO (left) and SuN (right) portions. Legends are identical for both.

previously identified levels are confirmed here (Fig. 5.14, 5.16), with the caveat that the resolution of SuN was not high enough to distinguish the two proposed levels at ~ 1750 keV. Thus these two levels were combined into a single template, with relative intensities between them assigned per the intensities identified in [11]. In addition to the previously identified levels, two new levels are proposed at 2178 keV and 2289 keV. These two levels are composed of γ -rays identified in [11], and are here identified to be coincident with the 174 keV, 117 keV and 61 keV γ -rays. Thus they are placed as feeding entirely through the level at 174 keV to the ground state, as is depicted in the new proposed level scheme for ^{57}V in Fig. 5.17. All

the previously (currently) identified levels and γ -rays are marked with closed (open) triangles in Figs. 5.14, 5.16. Among the γ -rays in the SS is a small peak at 511 keV which is evidence of pair production generated by higher-energy γ -rays in the detector [71].

The templates for all the known discrete levels are constructed based on the proposed level scheme. Each template decay is simulated in `GEANT4` in terms of the SuN detector response. A linear superposition of the simulated templates are then fit to the data, and the results of the composite fit are shown in Figs. 5.18-5.20. The error analysis pipeline (Sec. 3.3) is then run on the resulting fits, estimating uncertainties for the fit β intensities. The uncertainties are extracted from the analysis taking the bounds of the Monte Carlo distributions as estimations of the statistical uncertainty, and the bounds from the MOEA/D analysis as estimations of the systematic uncertainty—or how well the templates actually construct the decay. The sum of the two sources is taken as the total uncertainty on the feeding to the given level. The results are displayed in Tab. 5.4, which also include the previously estimated intensities as well as the resulting $\log ft$ value for each level. When the lower limits are inclusive of zero, an upper limit is assigned at a 95% confidence level. As with similar β -decay studies in the past [1], the TAS analysis here finds a much reduced ground-state intensity than the high-resolution Ge detector study of the same isotope [11].

Individual γ -ray intensities are also extracted from the SS by fitting individual Gaussian peaks with mean energies of the known transitions and variances calculated from the SuN detector response at that energy. The integral of the fit is then divided by the integrated total counts in the background- and daughter-subtracted multiplicity distribution to determine the absolute intensity of the given transition. These results (Tab. 5.5) are in agreement with [11] for the low-energy transitions, but are substantially larger for higher energies. The combined decreased efficiency in Ge detectors [72] and larger resolution of SuN at higher

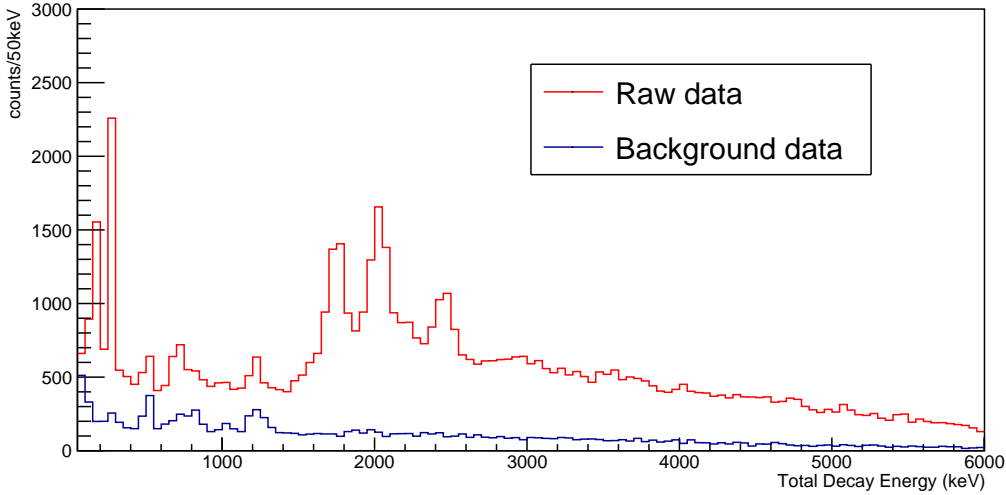


Figure 5.12: Raw, forward-correlated TAS (blue) and reverse-correlated background TAS (red) for the ^{57}Ti decay. Both are cut to only include decays in the first 300 ms after implantation.

Level (keV)	Prev. Intensity (%)	Current Intensity (%)	$\log ft$
0	54(3)	3(2)	5.88(18)
174	5(3)	6(2)	5.63(13)
1731 & 1754	1(1) + 16(2)	25(2)	4.65(2)
2036	16(2)	27(2)	4.55(2)
2178	–	4(1)	5.36(9)
2289	–	3(1)	5.50(13)
2475	7(1)	12(2)	4.81(5)
> 2475	–	21(3)	–

Table 5.4: Table showing the previously and currently measured intensities, along with $\log ft$ values, to the various energy levels in the decay of ^{57}Ti to ^{57}V

energies both contribute to these differences. Systematic errors for these intensities are not calculated here but are likely to be substantial ($> 5\%$ absolute error) and would allow for these measurements to be consistent with past data.

5.3.2 ^{57}Sc Decay

The background subtraction proceeds for the ^{57}Sc decay spectra as with ^{57}Ti in Sec. 5.3.1, though here the gate for parent decays is set as the first 100 ms (4-5 half-lives of ^{57}Sc) and

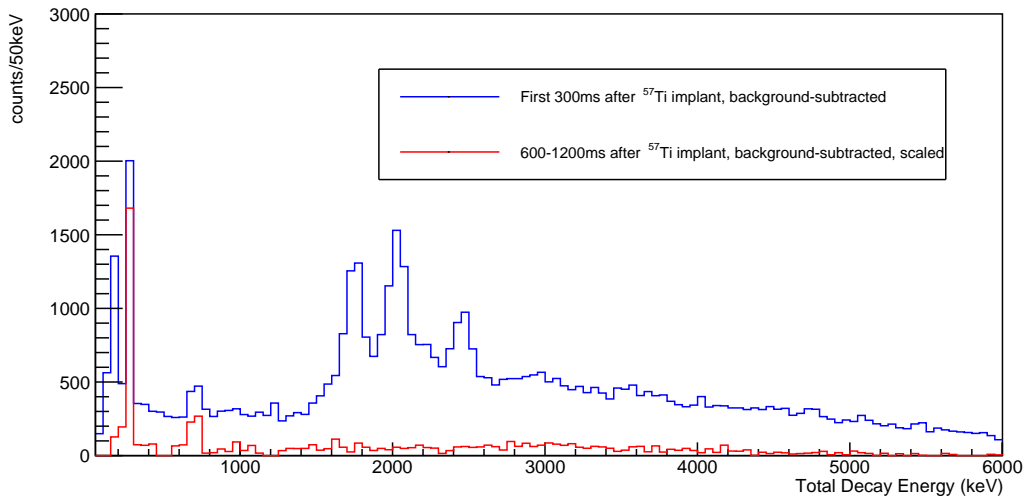


Figure 5.13: Background-subtracted TAS for $t < 300$ ms after implantation (blue) and the region $600 < t < 1200$ ms (red) for the ^{57}Ti decay. Note the two levels at 268 keV and 692 keV which are due to the β -daughter decay of ^{57}V .

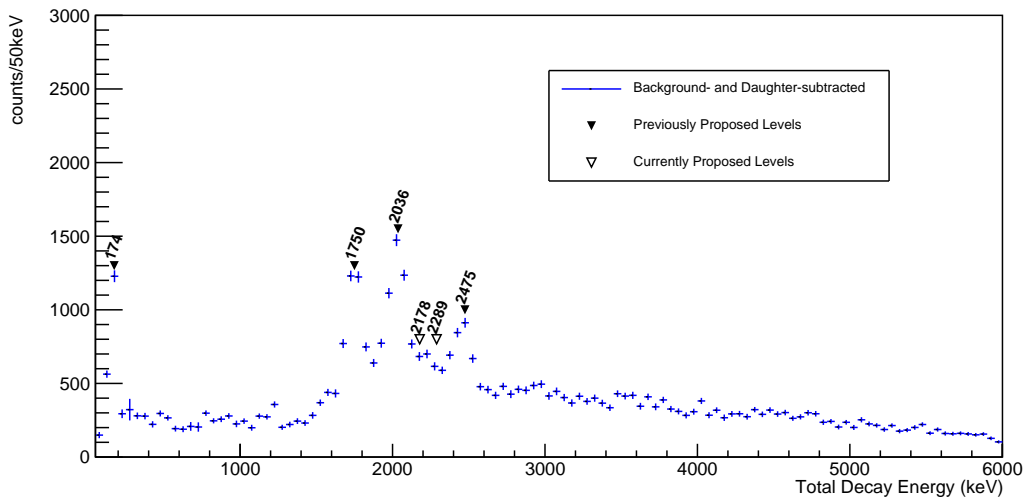


Figure 5.14: Final, background- and daughter-subtracted TAS for the ^{57}Ti decay. Note the two levels from ^{57}V are now removed. Closed triangles show the previously proposed levels [11], while the open triangles indicate proposed levels from this work.

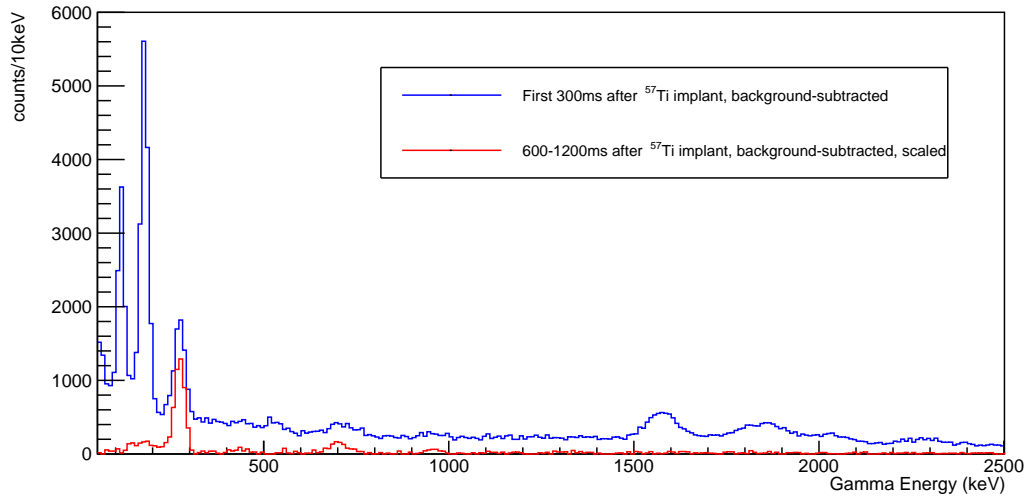


Figure 5.15: Background-subtracted SS for $t < 300$ ms after implantation (blue) and the region $600 < t < 1200$ ms (red) for the ^{57}Ti decay. Note the two γ -rays at 268 keV and 692 keV which are due to the β -daughter decay of ^{57}V .

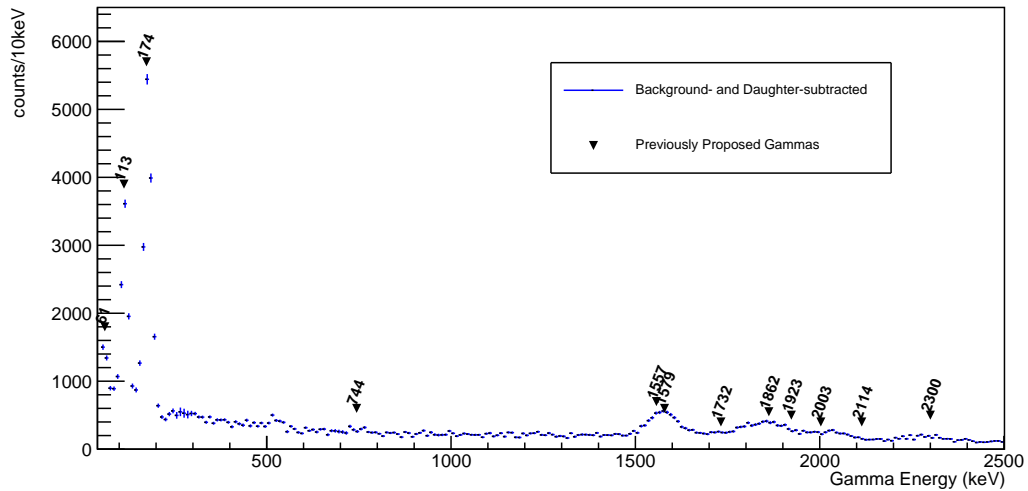


Figure 5.16: Final, background- and daughter-subtracted SS for the ^{57}Ti decay. Note the two levels from ^{57}V are now removed. Closed triangles show the previously identified γ -rays [11], while the open triangles indicate proposed levels from this work. The peak at 511 keV is due to electron pair production.

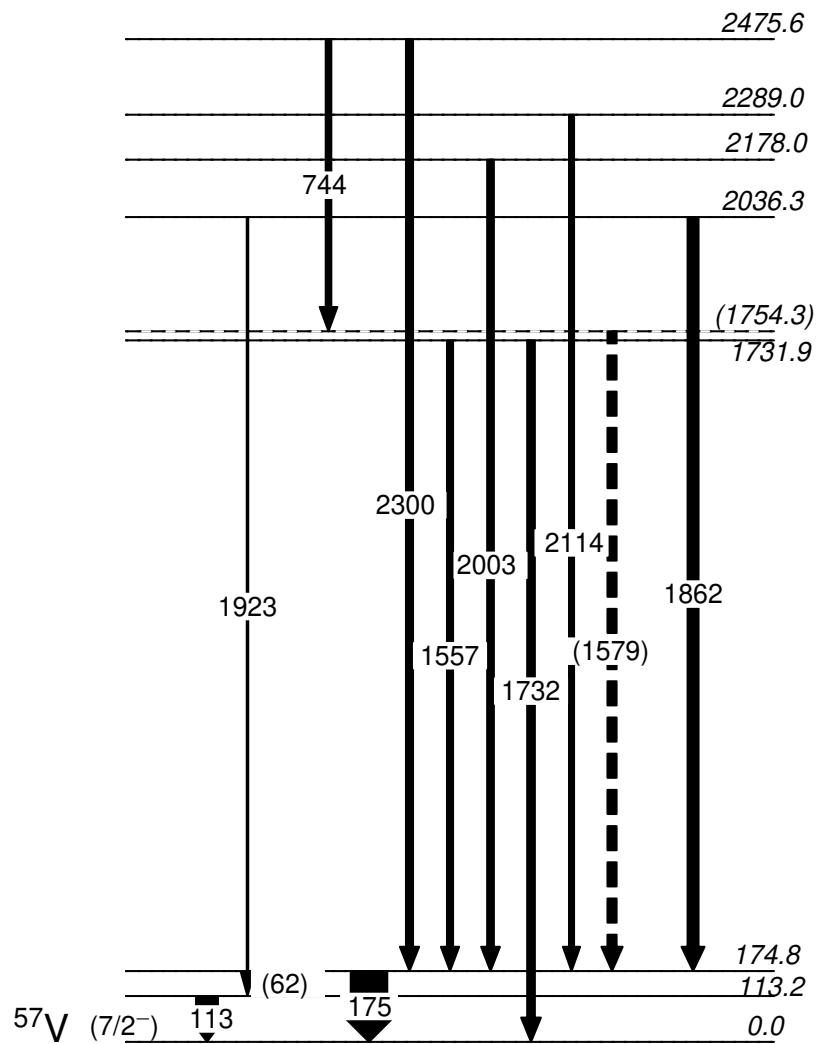


Figure 5.17: Revised ^{57}V level scheme for the β decay of ^{57}Ti to ^{57}V

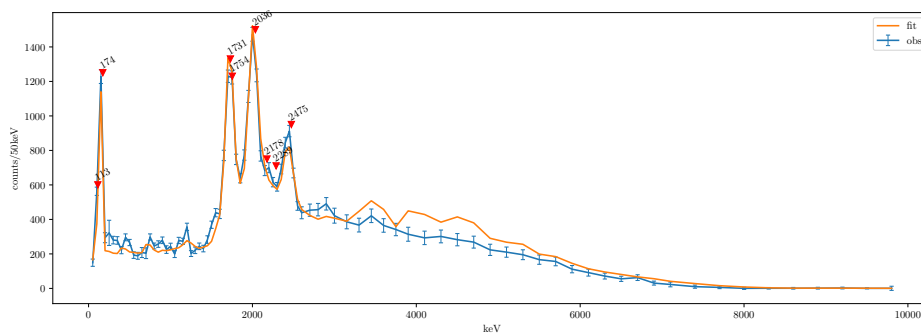


Figure 5.18: TAS for the ^{57}Ti decay.

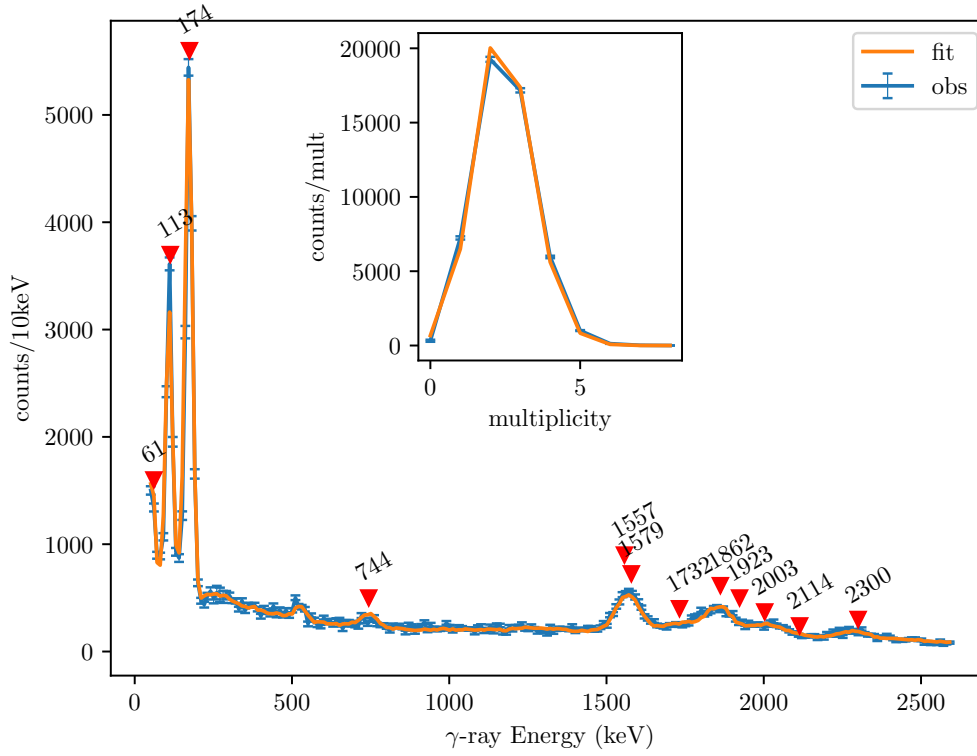


Figure 5.19: SS for the ^{57}Ti decay, the multiplicity fit is inset

γ -ray Energy (keV)	Prev. Intensity (%)	Current Intensity (%)
61	–	7.8
113	14(1)	18
174	31(2)	30
744	2.3(4)	4.6
1557, 1579	2.2(5), 16(2)	12.7
1732	1.2(2)	6.2
1861	2.6(5)	9
1922	2.6(5)	1.3
2003	1.8(5)	5.5
2114	0.7(3)	4.2
2300	5.0(5)	5.8

Table 5.5: Table showing the previously and currently measured intensities of individual γ -rays in the decay of ^{57}Ti to ^{57}V

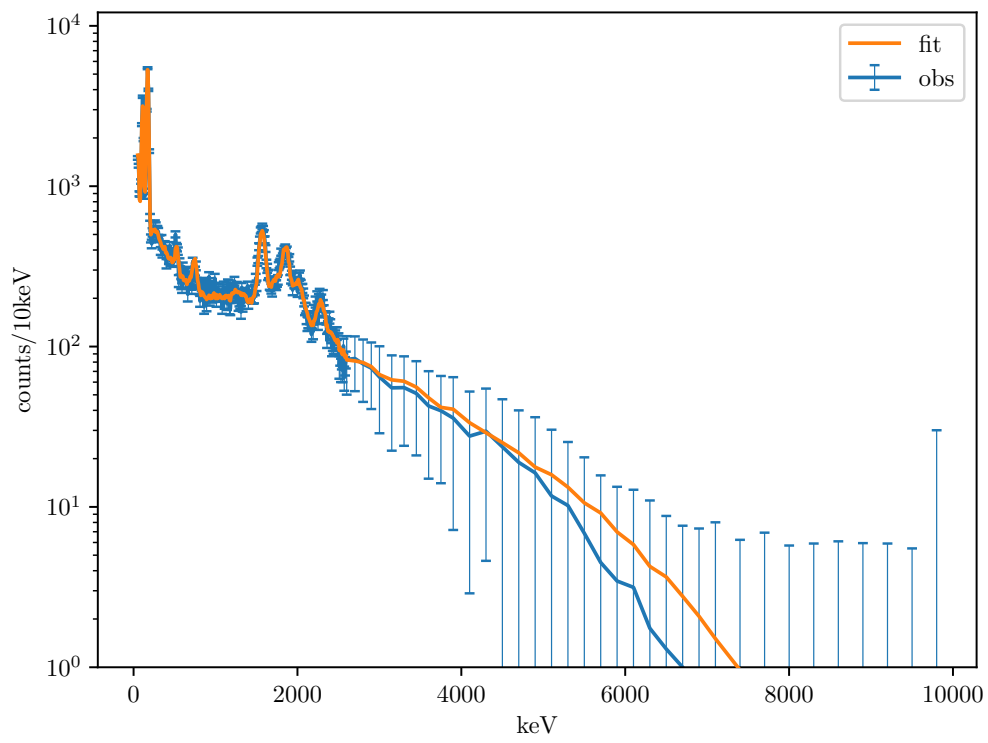


Figure 5.20: Log-scaled SS for the ^{57}Ti decay, including higher energy γ -rays

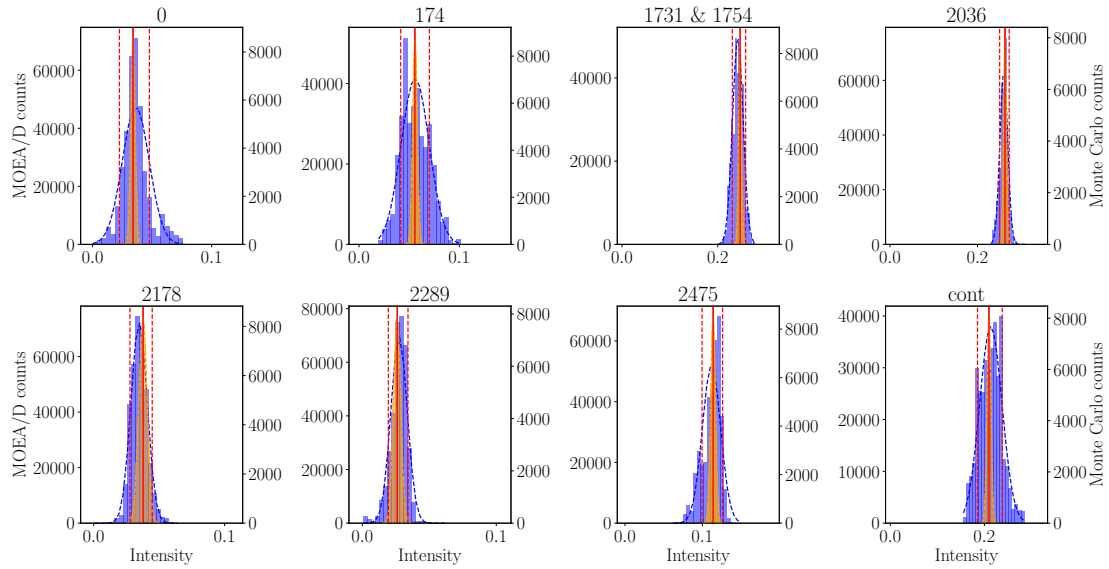


Figure 5.21: Results of the MOEA/D algorithm fit of the templates to the observed spectra (blue histogram) overlaid with the results of the Monte Carlo variation on the observed spectra (green histogram) for the β decay of ^{57}Ti to ^{57}V . Only the seven identified discrete levels are shown, with the summed feedings to the quasi-continuum levels shown in the eighth panel. The solid red line indicates the intensity given by the composite fit, and the dashed red lines indicate the upper and lower bounds for each template using the combined MOEA/D and Monte Carlo error estimation.

the daughter background is subtracted by gating on the first 10 ms of the ^{57}Ti particle-gated decays and scaling these to match the expected ratio $^{57}\text{Ti}:$ ^{57}Sc based on the decay curves and subtracted from the total TAS and SS respectively. Neutron-daughter (^{56}Ti) decays have no γ -ray emission above 2% [61], and both the granddaughter and neutron-granddaughter have long enough half-lives (> 200 ms) that they are negligible in the first 100 ms decay window. Thus subtractions are only necessary for the ^{57}Ti daughter. Since the experimental data set includes ^{57}Ti decays, the subtraction can be done by gating on the decays from ^{57}Ti implants, resulting in spectra of more pure ^{57}Ti than the late-time method used to approximate the ^{57}V decays above. The resulting SS and TAS histograms for ^{57}Sc decay are shown in Figs. 5.23–5.26.

A previous β -decay study [3] found several prominent γ -rays in the decay of ^{57}Sc (see Prev. Intensities in Tab. 5.7), but lacked statistics to identify coincidences and construct a level scheme beyond the suggestion that the high absolute intensity of the 364 keV γ -ray is evidence for the existence of a level that directly populates the ground state of ^{57}Ti . In addition, several lower-lying energy levels in ^{56}Ti were also established via ^{57}Sc β -decay. These use the levels include the ground state and the three lowest lying levels at 1128 keV, 1879 keV, and 2289 keV [3]. Since the $P_n = 12(4)\%$ for ^{57}Sc , these low lying states in ^{56}Ti may potentially be populated by β -delayed neutron emission from ^{57}Sc .

Though SuN lacks the resolution of HPGGe detectors, the efficiency allows for coincidences to be established between specific γ -ray peaks. Unique γ -rays which appear alone include 364 keV, 1144 keV and 1451 keV. Coincidences exist between the 364 keV γ -ray and each of 1087 keV, 1570 keV and 2050 keV γ -rays. Additionally, there are three γ coincidences between γ -rays at 364 keV, 780 keV and 820 keV; and 364 keV, 979 keV and 1087 keV. Finally, a two γ coincidence appears between 160 keV and 1840 keV.

The constructed level scheme for ^{57}Ti used in the simulations is shown in Fig. 5.22 and is the best attempt to rectify the more precisely measured γ -ray energies of [3] with the observed coincidences and multiplicities. The lower-resolution of SuN means that γ -ray energies cannot be determined with the precision of HPGe detectors. Therefore, deference was given to the specific energies previously observed when constructing the level scheme. Due to the significant P_n , β -delayed neutron emission to the ground state and first three excited states (1128 keV, 1879 keV and 2289 keV [3]) in ^{56}Ti were also simulated and included in the fit.

The fits are here constrained such as to require β -n feeding that matches the determined $P_n = 12\%$. As with the decay of ^{57}Ti , the error bar on the level intensities are calculated via the Monte Carlo and MOEA/D simulation methods, shown in Fig. 5.30 and tabulated in Tab. 5.6. Upper limits at a 95% confidence level are shown on the intensities whose lower limits are inclusive of zero.

The existence of the 364 keV level is here confirmed via the TAS. The newly proposed levels at 1451 keV, 1934 keV, 2000 keV, 2414 keV and 2430 keV have non-zero feeding above a lower limit, though the 1934 keV and 2000 keV and 2414 keV and 2430 keV cannot be distinguished. Moreover, the order of γ -rays from the 2000 keV level is unclear as no other coincidences exist. Significant feeding is also proposed to the ground and first excited states of ^{56}Ti , with marginal feeding above 1128 keV.

5.3.3 ^{59}Ti Decay

The background subtraction proceeds as with ^{57}Sc in Sec. 5.3.2, though here the gate for parent decays is set as the first 120 ms (4 half-lives of ^{59}Ti) and the daughter background is subtracted by gating on the first 7 ms of the ^{59}V particle-gated decays and scaling these to

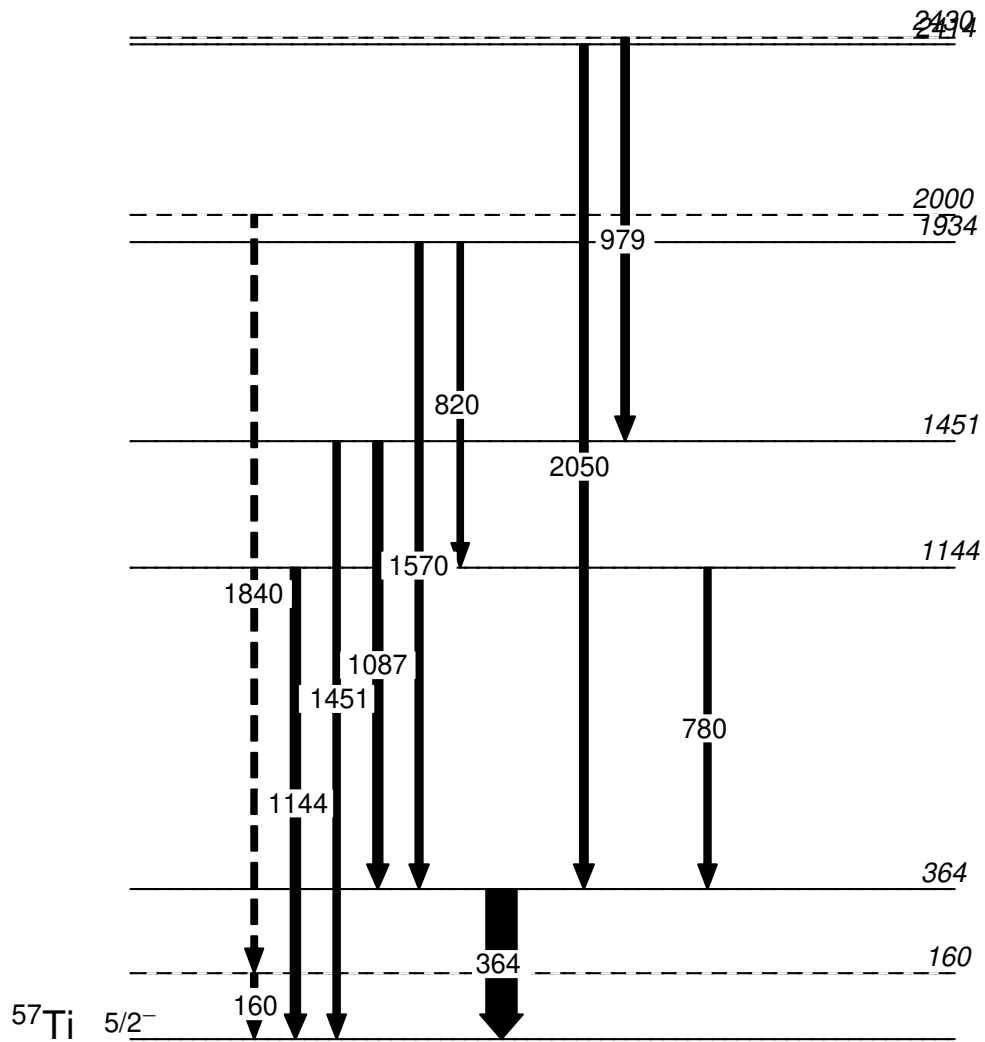


Figure 5.22: ^{57}Ti level scheme for the β decay of ^{57}Sc to ^{57}Ti

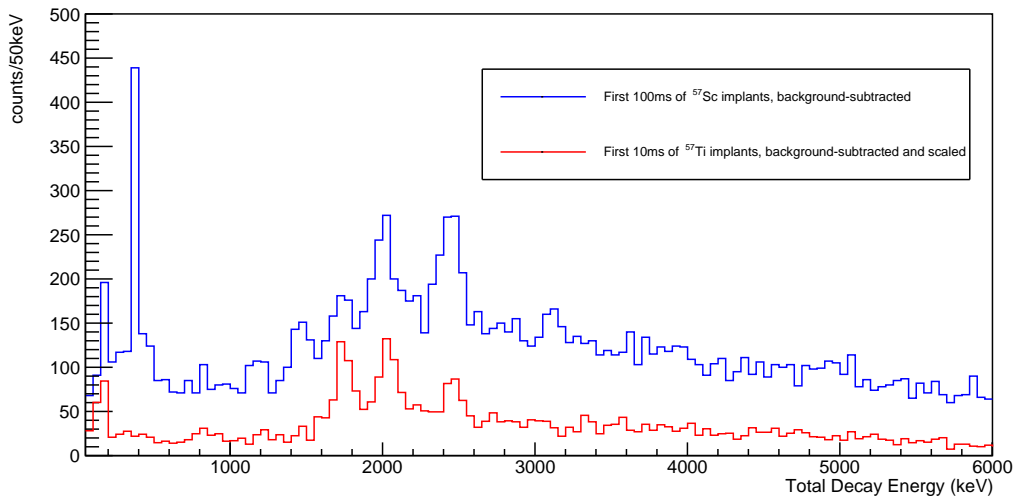


Figure 5.23: Reverse-time background subtracted TAS of the correlated decays within the first 100 ms following ^{57}Sc implants (blue), with the reverse-time background subtracted and scaled TAS of the correlated decays within the first 10 ms following ^{57}Ti implants (red).

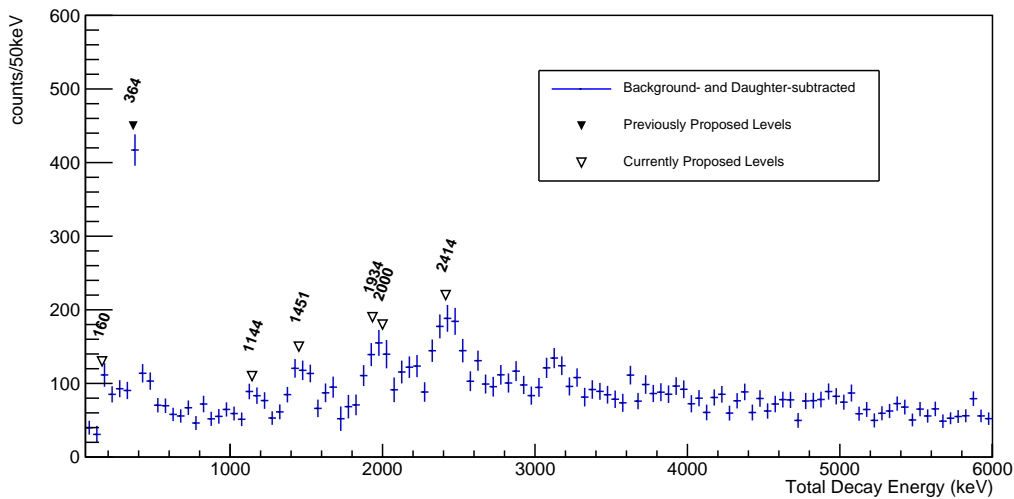


Figure 5.24: Final, background- and daughter-subtracted TAS for the ^{57}Sc decay. Closed triangles show the previously proposed levels [3], while the open triangles indicate proposed levels from this work.

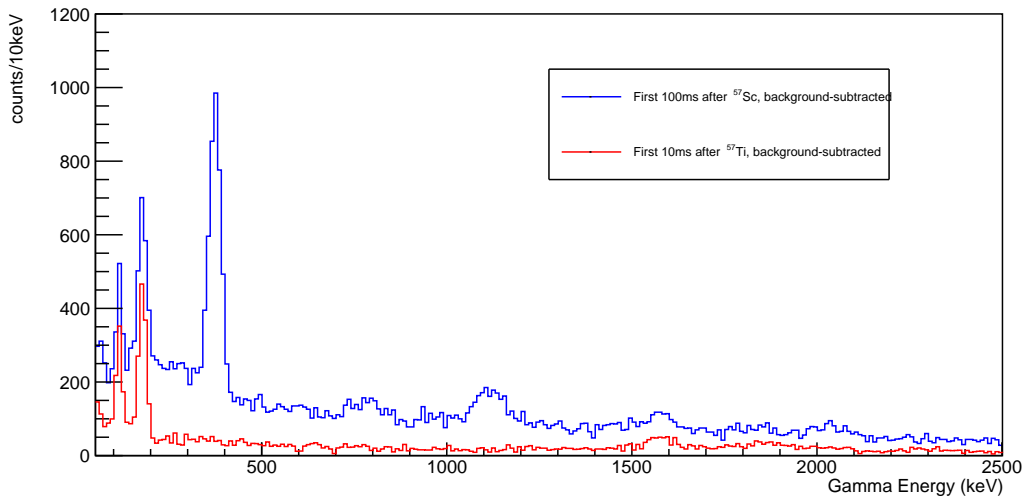


Figure 5.25: Reverse-time background subtracted SS of the correlated decays within the first 100 ms following ^{57}Sc implants (blue), with the reverse-time background subtracted and scaled SS of the correlated decays within the first 10 ms following ^{57}Ti implants (red).

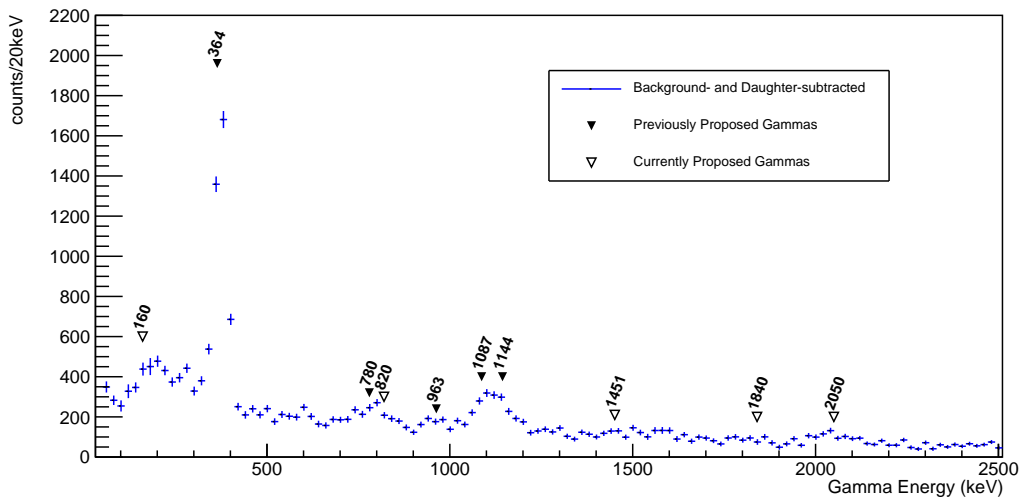


Figure 5.26: Final, background- and daughter-subtracted SS for the ^{57}Sc decay. Closed triangles show the previously identified γ -rays [3], while the open triangles indicate proposed γ -rays from this work.

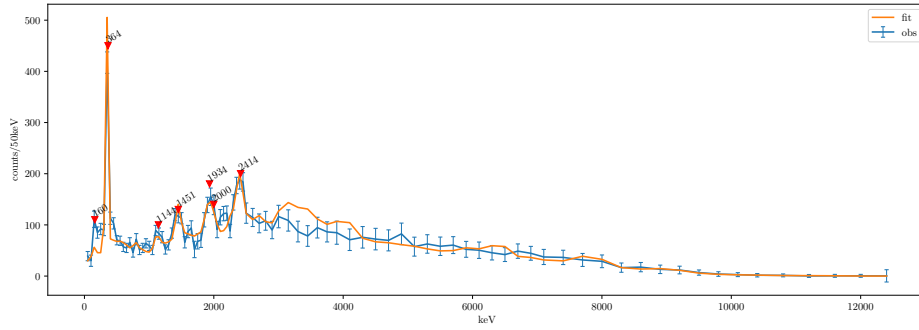


Figure 5.27: TAS for the ^{57}Sc decay

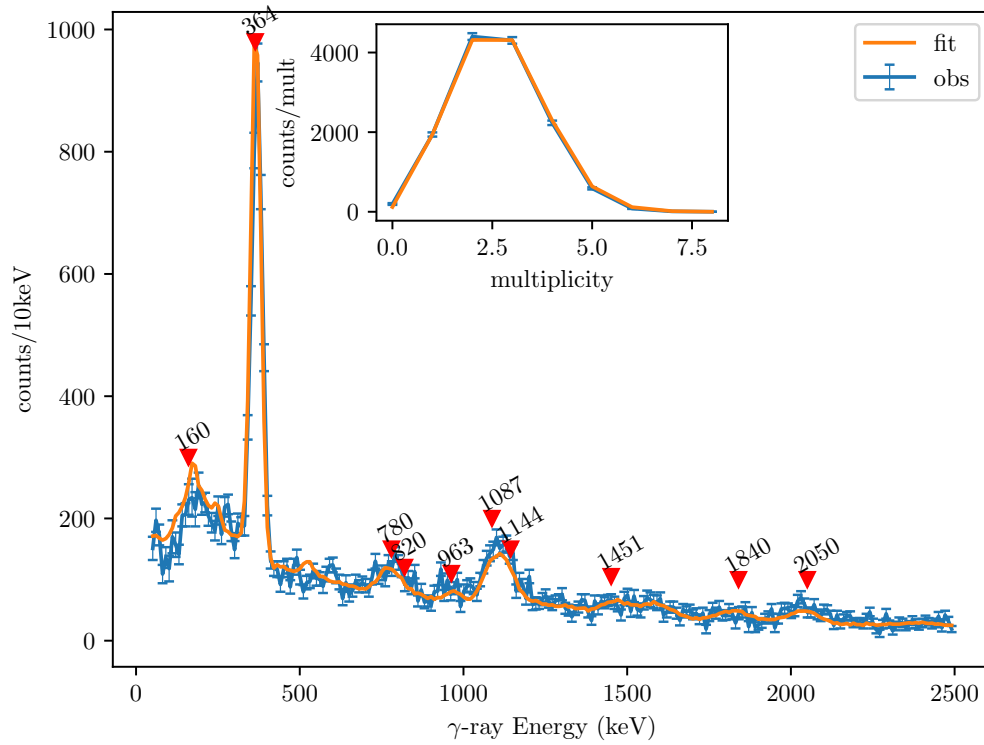


Figure 5.28: SS for the ^{57}Sc decay, the multiplicity fit is inset

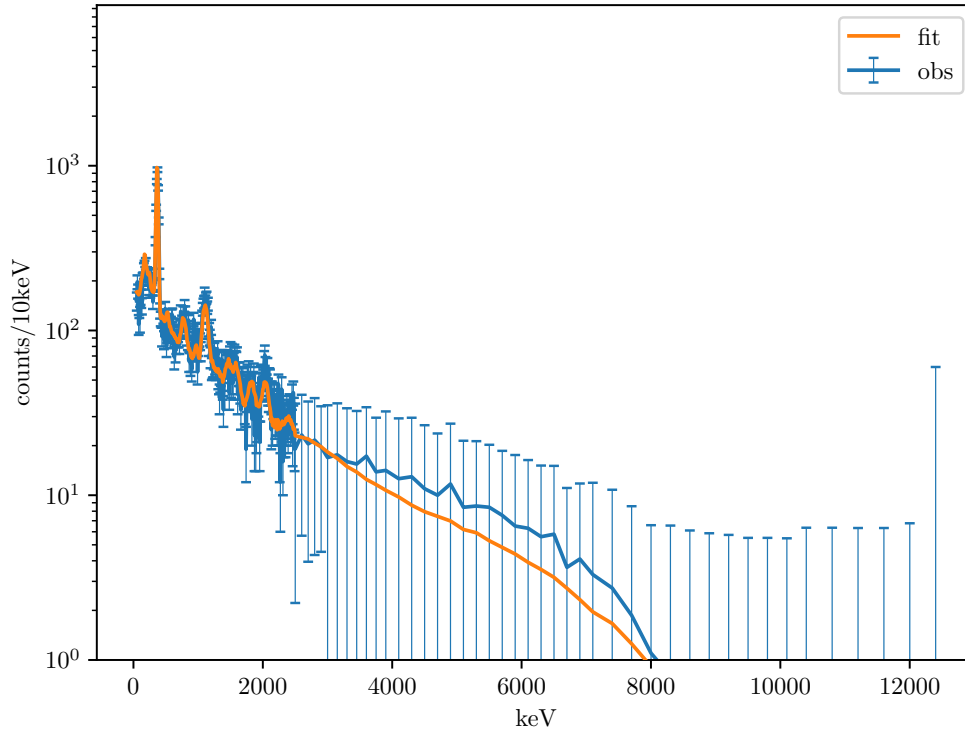


Figure 5.29: Log-scaled SS for the ^{57}Sc decay, including higher energy γ -rays

Level (keV)	Current Intensity (%)	$\log ft$
0	1(1)	6.02(89)
370	22(3)	4.73(7)
1144	< 2	> 5.76
1451	4(2)	5.29(30)
1934 & 2000	9(3)	4.86(14)
2414 & 2430	16(4)	4.49(12)
> 2600	37(9)	—
0n	5(3)	—
1128n	5(2)	—
1879n	2(2)	—
2289n	< 2	—

Table 5.6: Table showing the currently measured intensities, along with $\log ft$ values, to the various energy levels in the decay of ^{57}Sc to ^{57}Ti . $\log ft$ values are calculated by reweighting the intensities to only include transitions to the β -daughter.

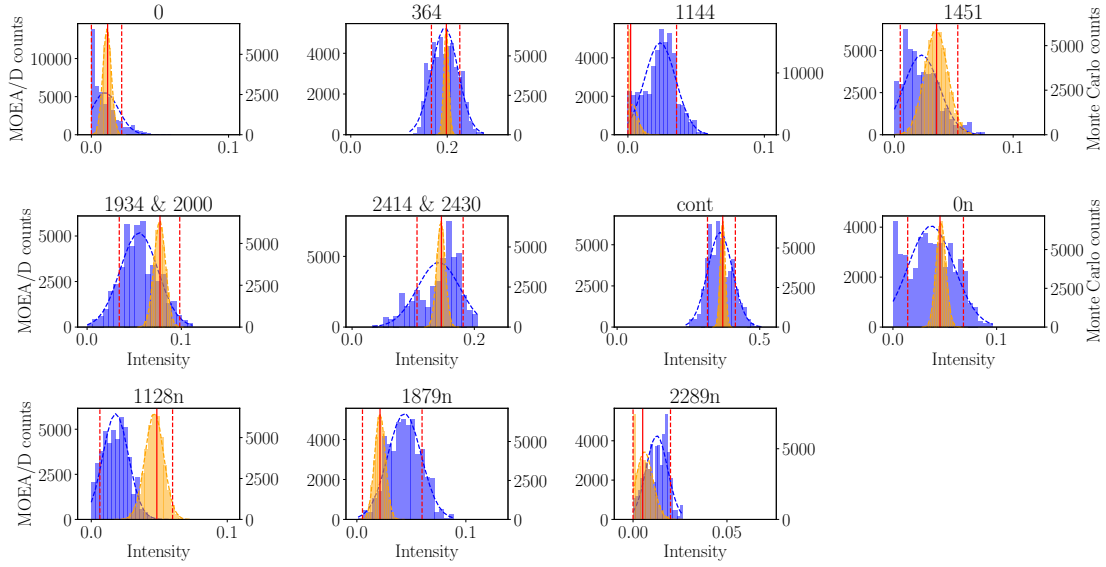


Figure 5.30: Results of the MOEA/D algorithm fit of the templates to the observed spectra (blue histogram) overlaid with the results of the Monte Carlo variation on the observed spectra (green histogram) for the β decay of ^{57}Sc to ^{57}Ti . Only the ten identified discrete levels are shown, with the summed feedings to the quasi-continuum levels shown in the eleventh panel. Four neutron-daughter feeding levels are also shown. The solid red line indicates the intensity given by the composite fit, and the dashed red lines indicate the upper and lower bounds for each template from the combined MOEA/D and Monte Carlo error estimation.

γ -ray Energy (keV)	Prev. Intensity (%)	Current Intensity (%)
160	–	5
364	76(8)	25
780	9(3)	7
979	5(1)	6
1087	21(3)	6
1127	12(2)	8
1451	–	5
1570	–	6
1840	–	5
2050	–	6

Table 5.7: Table showing the previously and currently measured intensities of individual γ -rays in the decay of ^{57}Ti to ^{57}V

match the expected ratio $^{59}\text{V}:^{59}\text{Ti}$ based on the decay curves and subtracted from the total TAS and SS respectively. The longer half-life of the neutron-daughter (^{58}V) and small P_n of ^{59}Ti mean the contribution of neutron-daughter decays to the γ -ray spectrum is negligible. Both the granddaughter and neutron-granddaughter have long enough half-lives (> 1 s) that they are negligible in the first 120 ms decay window. Thus subtractions are only necessary for the ^{59}V daughter. Since the experimental data set includes ^{59}V decays, the subtraction can be done by gating on the decays from ^{59}V implants. The resulting SS and TAS histograms for ^{59}Ti decay are shown in Figs. 5.32–5.35.

Previous experiments on ^{59}Ti found a γ -isomer at 108.5(5) keV [28, 29, 30] but no β -delayed γ -rays were reported. Thus the level scheme must be constructed entirely from the present data. This is done using the method established in Sec. 3.1.2. Gates are applied on the visible TAS peaks and the γ -rays which comprise them are identified as the centroids of resultant peaks in the SS. Unique γ -rays which appear alone include 115 keV, 910 keV, 1305 keV, 1645 keV, 2010 keV. Coincidences exist between the 910 keV and 1130 keV γ -rays, the 1135 keV and 1305 keV γ -rays, the 635 keV and 1645 keV γ -rays, and the 965 keV and 1645 keV γ -rays. Additionally, there are multiplicity two events for the TAS gate on 2610 keV which includes a peak at 1305 keV, so the 1305 keV and 1305 keV coincidence is also proposed. The resulting proposed level scheme is shown in Fig. 5.31. GEANT4 simulations use this level scheme, as well as the ground state and first excited state (114(2) keV) in the neutron daughter [28].

The fits are here constrained such as to require β -n feeding that matches the determined $P_n = 4\%$. As with the decay of ^{57}Ti , the error bar on the level intensities are calculated via the Monte Carlo and MOEA/D simulation methods, shown in Fig. 5.39 and tabulated in Tab. 5.8. Upper limits at a 95% confidence level are shown on the intensities whose lower limits are inclusive of zero.

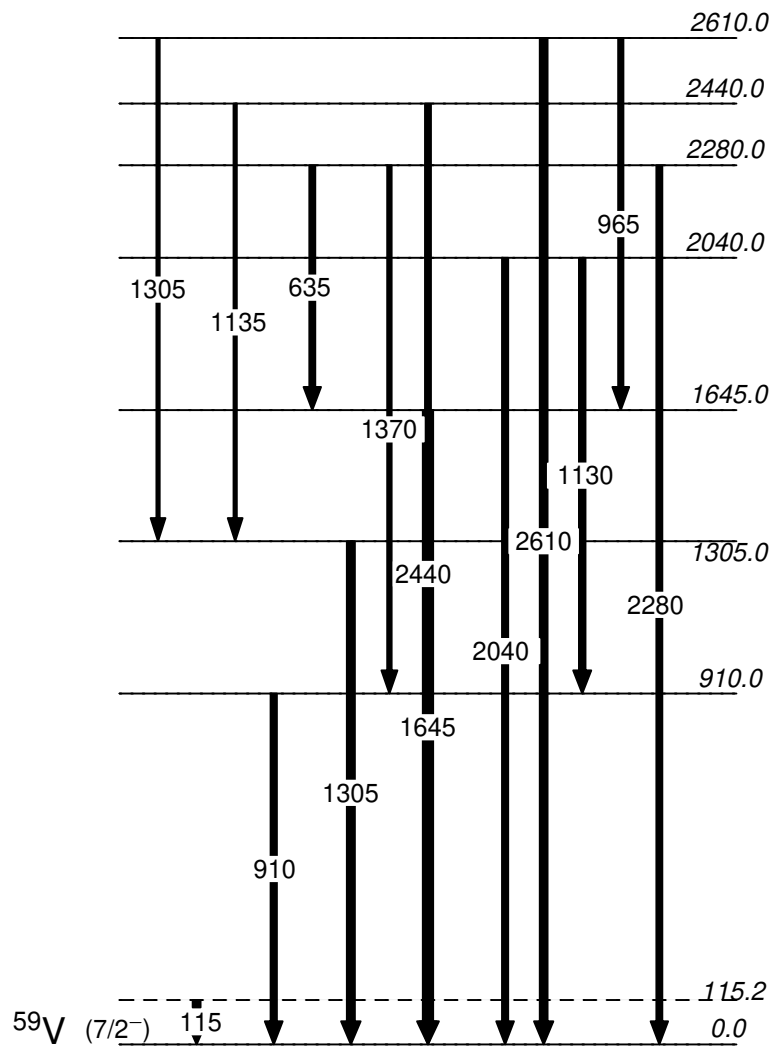


Figure 5.31: ^{59}V level scheme for the β decay of ^{59}Ti to ^{59}V

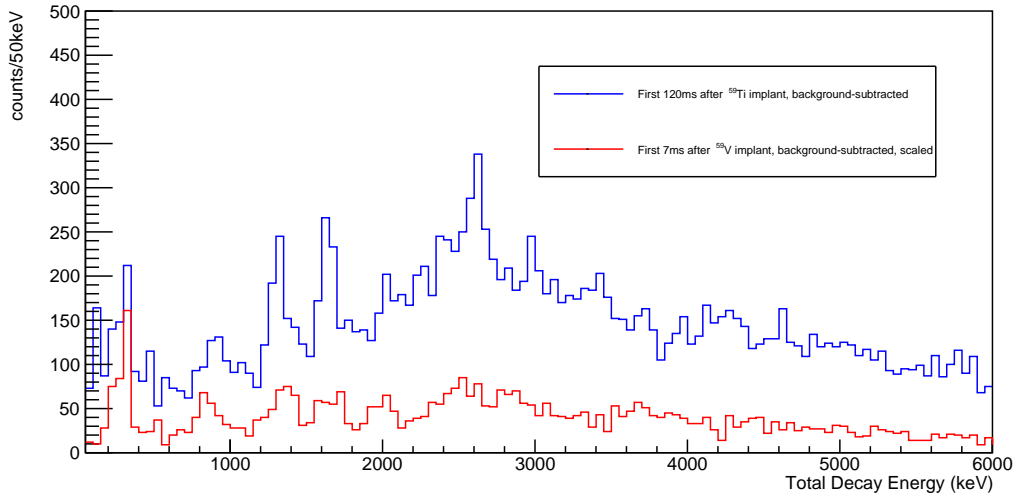


Figure 5.32: Reverse-time background subtracted TAS of the correlated decays within the first 120 ms following ^{59}Ti implants (blue), with the reverse-time background subtracted and scaled TAS of the correlated decays within the first 7 ms following ^{59}V implants (red).

The lack of coincidences assigned to the transition at 115 keV and absolute intensity comparable to the P_n suggest that the state be placed solely in the neutron-daughter ^{58}V rather than included in the ^{59}V level scheme. Though most of the proposed states have very small intensities, the existence of states at 1315, 1645, 2440, and 2610 keV are here established above 5% absolute intensities, as well as a large feeding to higher lying states.

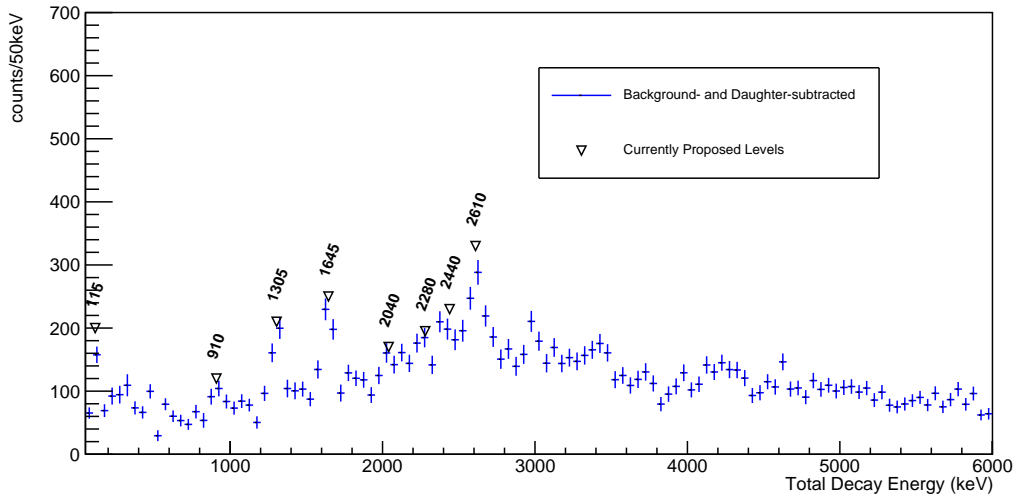


Figure 5.33: Final, background- and daughter-subtracted TAS for the ^{59}Ti decay. Open triangles indicate proposed levels from this work.

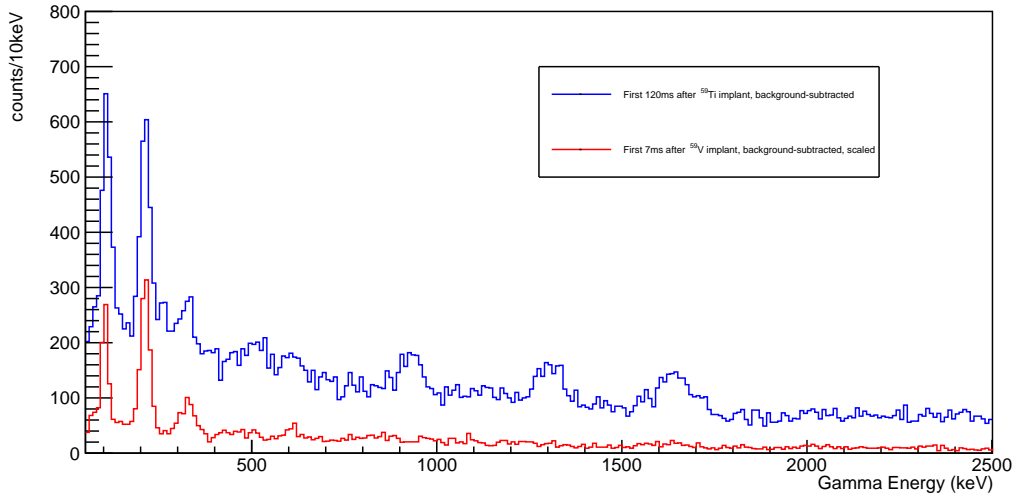


Figure 5.34: Reverse-time background subtracted SS of the correlated decays within the first 120 ms following ^{59}Ti implants (blue), with the reverse-time background subtracted and scaled SS of the correlated decays within the first 7 ms following ^{59}V implants (red).

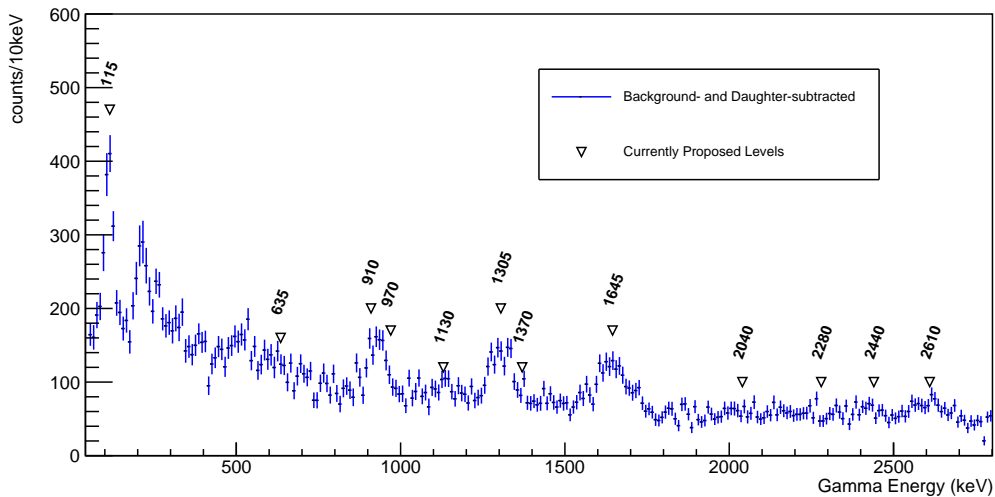


Figure 5.35: Final, background- and daughter-subtracted SS for the ^{59}Ti decay. Open triangles indicate proposed levels from this work. As with ^{57}Ti , the small peak at 511 keV is due to pair production in the detector from high-energy γ -rays. The peak around 210 keV is not labeled as no coincidences were established, nor is a specific TAS level clear. It is likely due to incomplete daughter subtraction.

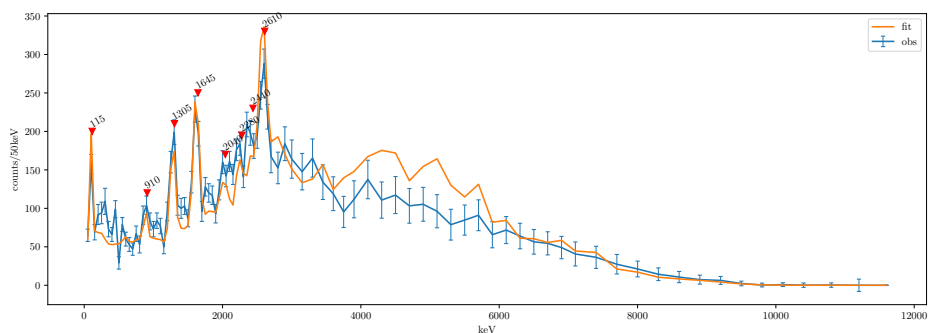


Figure 5.36: TAS for the ^{59}Ti decay

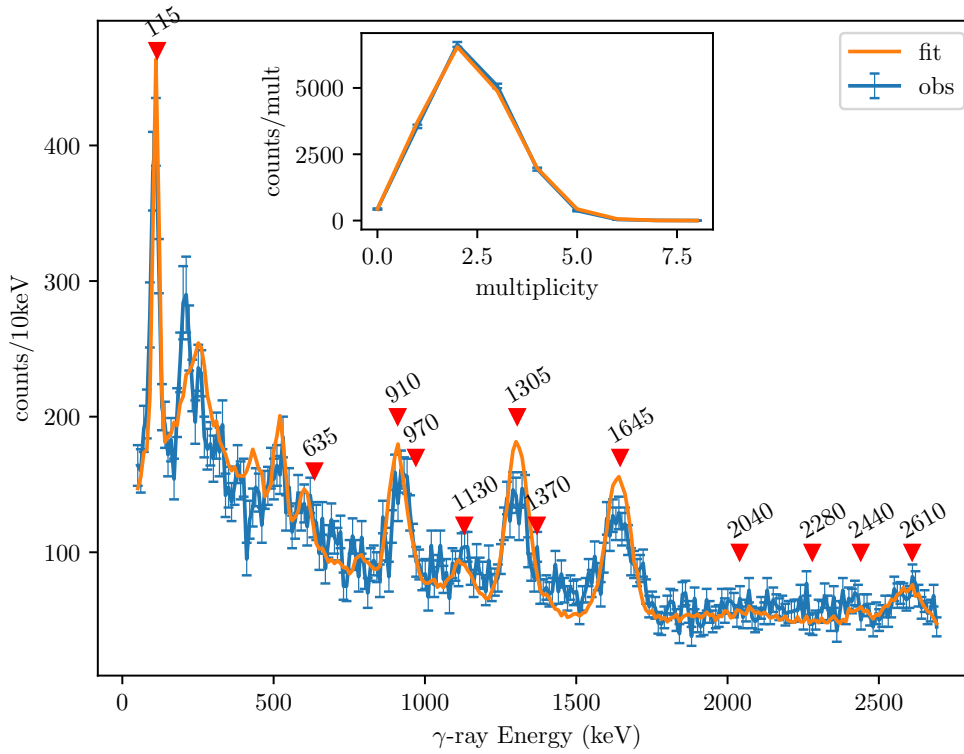


Figure 5.37: SS for the ^{59}Ti decay, the multiplicity fit is inset

Level (keV)	Current Intensity (%)	$\log ft$
0	3(2)	5.80(39)
115	3(1)	5.67(12)
1315	6(2)	5.23(13)
1645	10(2)	4.94(7)
2040	3(2)	5.32(21)
2280	5(2)	5.12(19)
2440	7(2)	4.95(13)
2610	15(5)	4.56(6)
> 2610	46(8)	—
0n	< 1	—
115n	4(1)	—

Table 5.8: Table showing the currently measured intensities, along with $\log ft$ values, to the various energy levels in the decay of ^{59}Ti to ^{59}V .

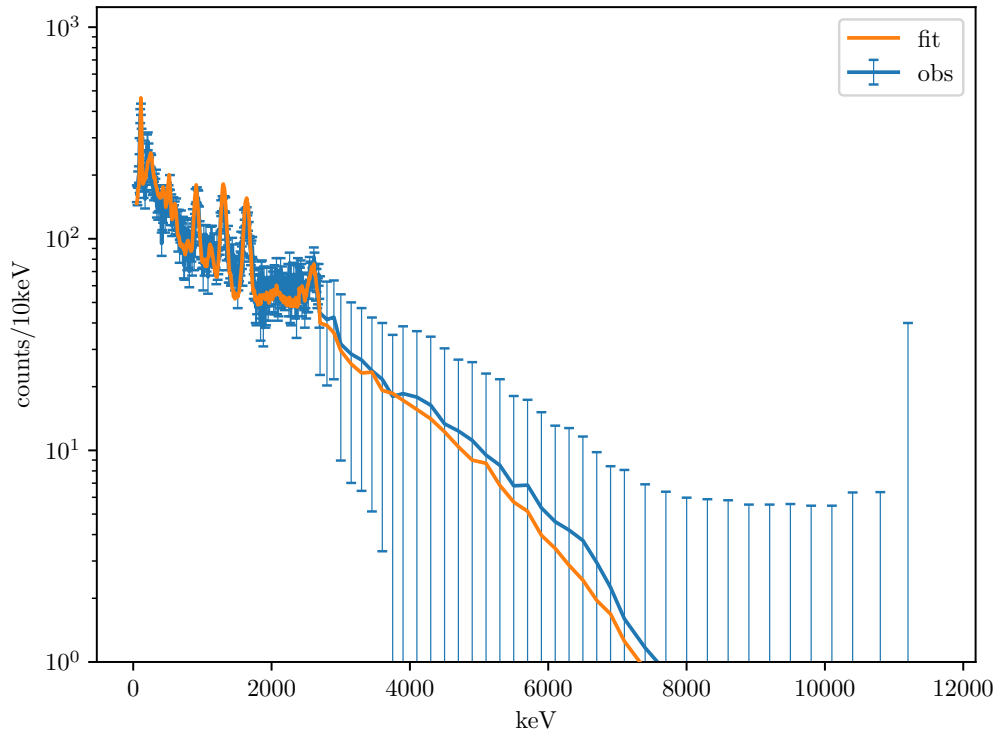


Figure 5.38: Log-scaled SS for the ^{59}Ti decay, including higher energy γ -rays

γ -ray Energy (keV)	Current Intensity (%)
115	6.8
635	5.1
910	5.3
965	4.5
1130	5.6
1305	6.9
1370	3.8
1645	8.9
2040	5.4
2280	5.1
2440	5.1
2610	6.7

Table 5.9: Table showing the previously and currently measured intensities of individual γ -rays in the decay of ^{59}Ti to ^{59}V

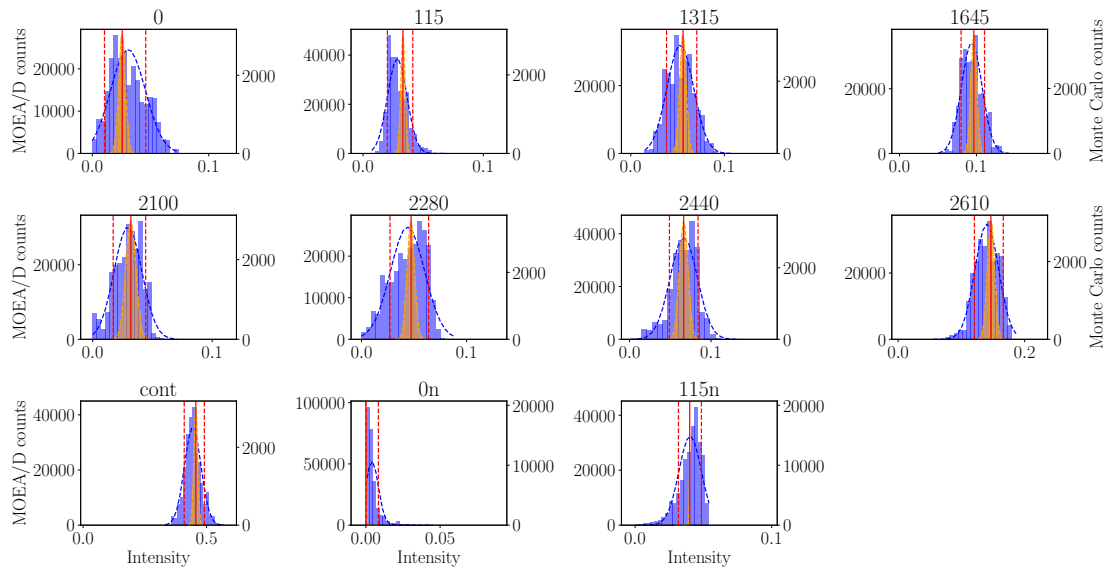


Figure 5.39: Results of the MOEA/D algorithm fit of the templates to the observed spectra (blue histogram) overlaid with the results of the Monte Carlo variation on the observed spectra (green histogram) for the β decay of ^{59}Ti to ^{59}V . Only the eight identified discrete levels are shown, with the summed feedings to the quasi-continuum levels shown in the ninth panel. Two neutron daughter levels are also included. The solid red line indicates the intensity given by the composite fit, and the dashed red lines indicate the upper and lower bounds for each template from the combined MOEA/D and Monte Carlo error estimation.

Chapter 6

Discussion

6.1 Nuclear Physics

6.1.1 ^{57}Ti

Using a folded-Yukawa potential, a Lipkin-Nogami pairing model, and including a residual Gamow-Teller interaction, each of the target nuclei is modeled under a quasi-random phase approximation (QRPA) and the P_n , half-life, and $B(\text{GT})$ transition strength of the decay is calculated [73, 74]. These calculations are subject to deformations in the ground-state energy of the parent nucleus which are approximated by the minimum of the nuclear potential-energy surface versus spheroidal deformation and axial symmetry [75]. For these calculations only spheroidal deformations are considered. A moderate spheroidal deformation of $\epsilon = 0.12$ is used for ^{57}Ti , with a predicted $P_n = 0.21\%$ and $T_{1/2} = 41.83$ ms. The predicted $B(\text{GT})$ transition strength plot is compared to the observed transition strengths in Fig. 6.1. In calculating the observed $B(\text{GT})$ strength from the observed intensities, all the transitions are assumed to be allowed, and the error bars incorporate both uncertainties from the intensities as well as from the Q -value, $Q_{\beta^-} = 10.50(27)$ MeV [32]. Only the intensities—and therefore the $B(\text{GT})$ strengths—of γ -decaying states below the neutron separation energy, S_n , have been experimentally determined. For ^{57}V , $S_n = 6.33(19)$ MeV [32], and transitions above this energy are included in the P_n .

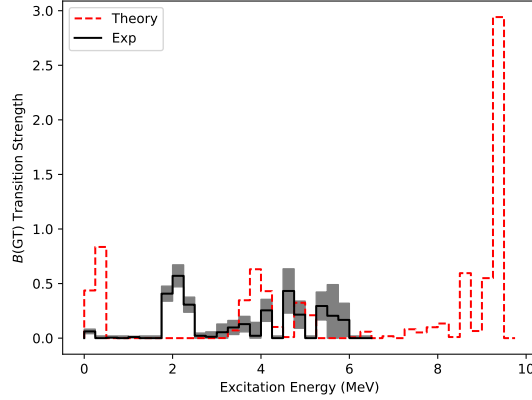


Figure 6.1: Comparison of QRPA predicted (dashed red) and experimentally observed (black, with gray shaded errors) $B(\text{GT})$ transition strengths for the decay of ^{57}Ti to ^{57}V . S_n of ^{57}V is at 6.33 MeV

Although the predicted half-life is less than half the experimentally observed values of $T_{1/2,\text{obs}} = 95(7)$ ms (BCS) and $94(1)$ ms (SuN), the predicted P_n is consistent with the value observed here, $P_{n,\text{obs}} < 3\%$, and the $B(\text{GT})$ matches well for higher-energy excitations. The low-energy spectrum appears to be shifted to higher energies by about 2 MeV with only a small amount of $B(\text{GT})$ strength remaining in the ground state. The QRPA predicted ground state $\log ft$ with this deformation is 4.2, well below both the previous experimental measurement of 4.7(2) and the current measurement of 5.88(37).

6.1.2 ^{57}Sc

The same model and procedure is used to make QRPA predictions about the decay of ^{57}Sc to ^{57}Ti . A moderate spheroidal deformation of $\epsilon = -0.1$ is used, with a predicted $P_n = 20.12\%$ and $T_{1/2} = 21.01$ ms. The predicted $B(\text{GT})$ transition strength plot is compared to the observed transition strengths in Fig. 6.2, where the experimental error bars incorporate both uncertainties from the intensities as well as from the Q -value, $Q_{\beta^-} = 12.92(133)$ MeV [32]. Additionally, the observed $B(\text{GT})$ strengths are only given up to the neutron separation

energy of ^{57}Ti , $S_n = 2.67(28)$ MeV [32].

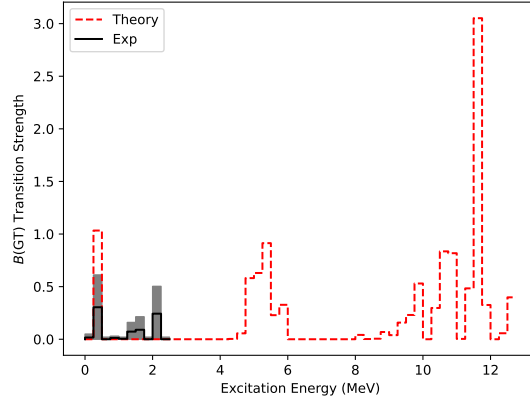


Figure 6.2: Comparison of QRPA predicted (dashed red) and experimentally observed (black, with gray shaded errors) $B(\text{GT})$ transition strengths for the decay of ^{57}Sc to ^{57}Ti . S_n of ^{57}Ti is at 2.67 MeV

The predicted P_n is above the observed, $P_{n,\text{obs}} = 12(4)\%$, though in agreement at 2σ . The predicted half-life also matches well with the values observed, $T_{1/2,\text{obs}} = 21(2)$ ms (BCS) and $T_{1/2,\text{obs}} = 20(1)$ ms (SuN). The $B(\text{GT})$ is difficult to compare, as the large experimental error bars cannot exclude very small transition strengths, nor confirm the large low energy feeding for certain. Additionally, the small S_n means the transition strengths can only be evaluated over a small range of excitation energies. Under these limitations, theory and experiment agree in the critical low-energy region below 1 MeV. Theory predicts low feeding strengths to the ground state, with significant feeding in the range between 250 keV and 500 keV, which is observed in the experiment. The observed feeding strength between 1 MeV and S_n while not predicted by theory, has too large of error bars to be confirmed non-negligible.

6.1.3 ^{59}Ti

The same model and procedure is used to make QRPA predictions about the decay of ^{59}Ti to ^{59}V . A moderate spheroidal deformation of $\epsilon = -0.15$ is used, with a predicted $P_n = 5.08\%$

and $T_{1/2} = 20.11$ ms. The predicted $B(\text{GT})$ transition strength plot is compared to the observed transition strengths in Fig. 6.3, where the experimental error bars incorporate both uncertainties from the intensities as well as from the Q -value, $Q_{\beta^-} = 12.32(26)$ MeV [32]. Additionally, the observed $B(\text{GT})$ strengths are only given up to the neutron separation energy of ^{57}Ti , $S_n = 5.55(18)$ MeV [32].

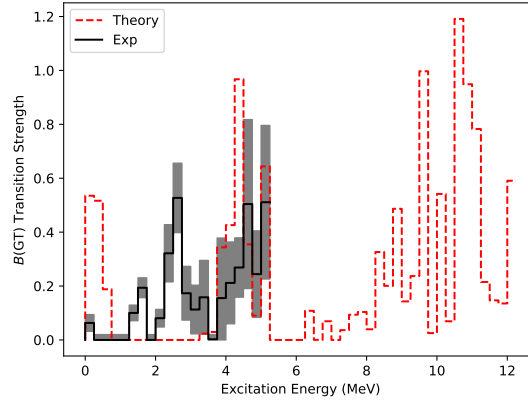


Figure 6.3: Comparison of QRPA predicted (dashed red) and experimentally observed (black, with gray shaded errors) $B(\text{GT})$ transition strengths for the decay of ^{59}Ti to ^{59}V . S_n of ^{57}V is at 5.55 MeV

The predicted P_n matches well with the observed value, $P_{n,\text{obs}} = 4(2)\%$, while the predicted half-life is lower than observed, $T_{1/2,\text{obs}} = 31(2)$ ms (BCS) and $T_{1/2,\text{obs}} = 26(1)$ ms (SuN). The predicted $B(\text{GT})$ is consistent with the observed for higher-energy excitations up to the S_n . For lower energies, the observed transition strengths are much lower, with a higher strength in the middle range of 1–3 MeV. As with ^{57}Ti a moderate energy shift of 2 MeV which leaves a smaller transition strength to the ground state still intact, could resolve the discrepancy at low and medium energies between theory and observed. This difference has large astrophysical implications, as the reduced feeding to the ground state drastically reduces the potential for Urca cooling.

6.2 Nuclear Astrophysics

In order to estimate the impact of the newly reported transition strengths on the potential Urca cooling in neutron star crusts, a calculation is performed by evolving a nuclear network with a composition corresponding to that of superburst ashes through the temperature and density profiles expected from the neutron star crust environment [19]. The β -decay and EC transition strengths are taken from experiment when available and calculated via the finite-range drop model (FRDM) and QRPA otherwise [76].

The superburst ashes are evolved through the outer crust to a depth corresponding to a density of $\rho = 2 \times 10^{12} \text{ g m}^{-3}$. Beyond this depth neutron reactions become favorable and the mass chains are no longer confined to a specific A . This largely suppresses Urca cooling [25].

The total luminosity for each Urca pair is calculated and summed across the entire length of the evolution. The results are compiled and differences between the luminosity before and after updating the ground state to ground state transitions of the three isotopes are plotted (Fig. 6.4). Additionally, the error bars on the updated luminosities are determined by running two additional simulations, one using all three $\log ft$ lower limits, and one using all the upper limits.

These results demonstrate a significant decrease in total expected Urca cooling in these scenarios, as the predicted ^{57}Sc cooling lies at the upper bound of the updated measurement, and as such may longer be the most prominent cooler, surpassed by ^{61}V . Expected cooling from ^{57}Ti drops below ^{57}V to become only the third most prominent in the $A = 57$ chain, while ^{59}Ti cooling is reduced as well.

The evolution of total energy in the system throughout the simulation is shown (Fig.

6.5), as a comparison between the simulations using the previously predicted values to the current updated values. The impacts of the reduced estimated cooling are clear for both ^{57}Ti and ^{57}Sc . Cooling from ^{59}Ti is concurrent with the much larger cooling from ^{61}V , and so the impact is less visually clear.

To fully constrain the Urca cooling from these layers, additional measurements will be needed on the even more neutron-rich isotopes seen here, including: ^{57}Ca , ^{59}Sc , and ^{61}Ti , all of whose experimental data consist of mass measurements [77], with little to no half-life estimates, and no β -decay data. Conducting β -decay studies for these exotic isotopes will be possible at the full reaches of FRIB, whose ultimate secondary beam rates are expected to be 2, 11, and 92 pps, respectively.

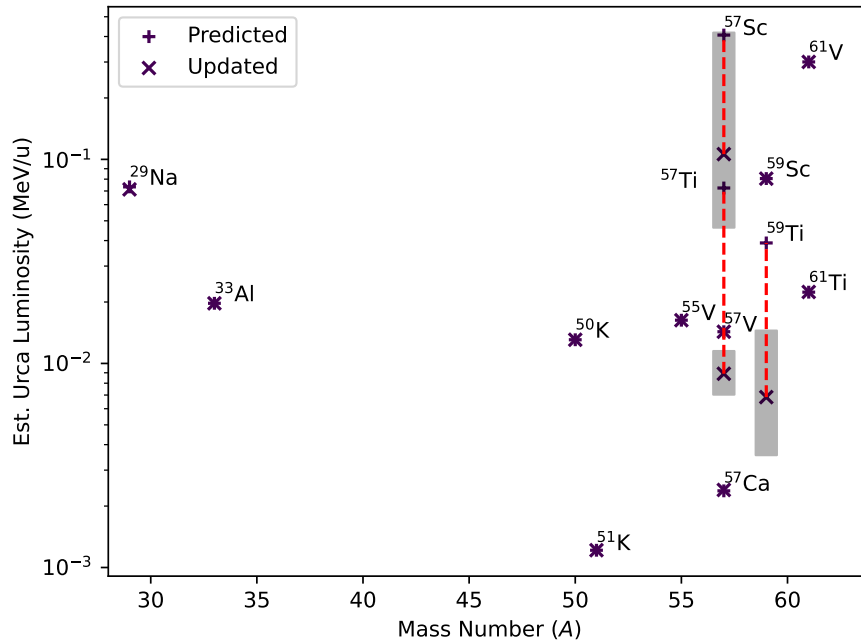


Figure 6.4: Comparison of the estimated Urca luminosity by Urca β -parent. The red dashed line links the results from the previously predicted g.s.-to-g.s. intensities, to the results using the newly constrained values introduced here. The gray shaded region indicates the error bars on the updated values.

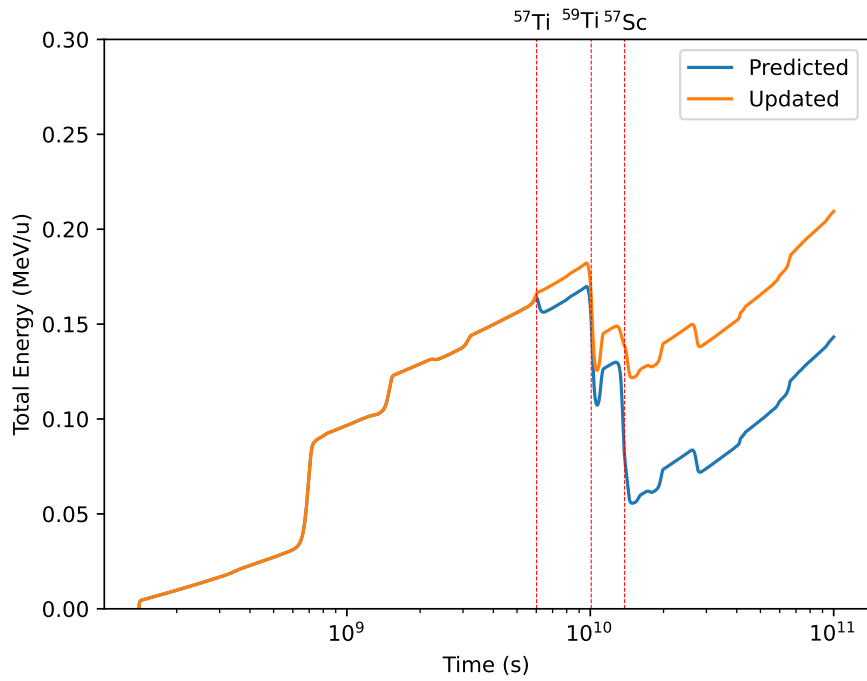


Figure 6.5: Comparison of the evolution of total energy during the simulation using the predicted (blue) and updated (orange) transition values. The vertical red dashed lines are to guide the eye to points in time where the various Urca coolers release energy. The lines are labeled by the β^- parent of the Urca pair. The impact of the change in ^{59}Ti cooling is overshadowed by the much larger ^{61}V cooling, which occurs simultaneously.

Chapter 7

Conclusion

Through the previously established experimental techniques of total absorption spectroscopy combined with a neutron long counter, the ground state to ground state transitions of neutron-rich isotopes ^{57}Ti , ^{57}Sc , and ^{59}Ti are effectively constrained to 3(2)%, 1(1)%, and 3(2)%, respectively. These results mitigate the impact of the Pandemonium effect to which previous experiments were susceptible, and utilize novel methods of evaluating the systematic error on the feeding intensities which may be applied to further TAS studies. The application of the newly constrained transition strengths to Urca cooling in neutron star crusts significantly reduces the total expected cooling of these pairs by 74%, 88%, and 82% respectively.

In addition, new γ -rays are identified in the β -decays of ^{57}Sc and ^{59}Ti , as well as new level schemes proposed for all three isotopes. Further study via HPGe detectors is necessary to verify the observed coincidences and γ -ray energies, but is not expected to impact the observed strong feeding to highly excited energy levels in the daughter nuclei.

While the beam rates at the NSCL were insufficient to apply this method to the even more neutron-rich ^{57}Ca , ^{59}Sc , and ^{61}Ti , the isotopes are expected to be within the range of the newly commissioned Facility for Rare Isotope Beams (FRIB). Already, β -decay studies using the FRIB Decay Station (FDSi) have been published [78], with measurements of β -decays in the region of ^{51}K in analysis. Together with nuclear astrophysics models and

astrophysical observation of quasi-persistent transients, these measurements promise deeper understanding of the inner physics of neutron stars.

BIBLIOGRAPHY

BIBLIOGRAPHY

- [1] Wei Jia Ong. *Quantifying the Urca Cooling Impact of Mass 61 Nuclei in X-Ray Bursting Systems*. PhD thesis, Michigan State University, January 2018.
- [2] S. N. Liddick, P. F. Mantica, R. Broda, B. A. Brown, M. P. Carpenter, A. D. Davies, B. Fornal, T. Glasmacher, D. E. Groh, M. Honma, M. Horoi, R. V. F. Janssens, T. Mizusaki, D. J. Morrissey, A. C. Morton, W. F. Mueller, T. Otsuka, J. Pavan, H. Schatz, A. Stolz, S. L. Tabor, B. E. Tomlin, and M. Wiedeking. Development of shell closures at $n=32,34$ in β decay of neutron-rich *sc* isotopes. *Physical Review C*, 70:064303, 12 2004.
- [3] H L Crawford, R V F Janssens, P F Mantica, J S Berryman, R Broda, M P Carpenter, N Cieplicka, B Fornal, G F Grinyer, N Hoteling, B P Kay, T Lauritsen, K Minamisono, I Stefanescu, J B Stoker, W B Walters, and S Zhu. β decay and isomeric properties of neutron-rich *ca* and *sc* isotopes. *REVIEW C*, 82:14311, 2010.
- [4] María Esther Estévez Aguado. *TAS measurements for neutrino physics and nuclear structure: study of the beta decays of 150Er, 152,156Yb and 188,190,192Pb*. PhD thesis, Universidad de Valencia, 2012.
- [5] A. Stolz, T. Baumann, T.N. Ginter, D.J. Morrissey, M. Portillo, B.M. Sherrill, M. Steiner, and J.W. Stetson. Production of rare isotope beams with the nscl fragment separator. *Nuclear Instruments and Methods in Physics Research Section B: Beam Interactions with Materials and Atoms*, 241(1):858–861, 2005. The Application of Accelerators in Research and Industry.
- [6] D.J. Morrissey, B.M. Sherrill, M. Steiner, A. Stolz, and I. Wiedenhoever. Commissioning the a1900 projectile fragment separator. *Nuclear Instruments and Methods in Physics Research Section B: Beam Interactions with Materials and Atoms*, 204:90–96, 2003. 14th International Conference on Electromagnetic Isotope Separators and Techniques Related to their Applications.
- [7] J. Pereira, P. Hosmer, G. Lorusso, P. Santi, A. Couture, J. Daly, M. Del Santo, T. Elliot, J. Görres, C. Herlitzius, K.-L. Kratz, L.O. Lamm, H.Y. Lee, F. Montes, M. Ouellette, E. Pellegrini, P. Reeder, H. Schatz, F. Schertz, L. Schnorrenberger, K. Smith, E. Stech, E. Strandberg, C. Ugalde, M. Wiescher, and A. Wöhr. The neutron long counter nero for studies of β -delayed neutron emission in the *r*-process. *Nuclear Instruments and Methods in Physics Research Section A: Accelerators, Spectrometers, Detectors and Associated Equipment*, 618(1):275–283, 2010.

- [8] A. Simon, S.J. Quinn, A. Spyrou, A. Battaglia, I. Beskin, A. Best, B. Bucher, M. Couder, P.A. DeYoung, X. Fang, J. Görres, A. Kontos, Q. Li, S.N. Liddick, A. Long, S. Lyons, K. Padmanabhan, J. Peace, A. Roberts, D. Robertson, K. Smith, M.K. Smith, E. Stech, B. Stefanek, W.P. Tan, X.D. Tang, and M. Wiescher. Sun: Summing nai(tl) gamma-ray detector for capture reaction measurements. *Nuclear Instruments and Methods in Physics Research Section A: Accelerators, Spectrometers, Detectors and Associated Equipment*, 703:16–21, 2013.
- [9] CJ Prokop, SN Liddick, BL Abromeit, AT Chemey, NR Larson, S Suchyta, and JR Tompkins. Digital data acquisition system implementation at the national superconducting cyclotron laboratory. *Nuclear Instruments and Methods in Physics Research Section A: Accelerators, Spectrometers, Detectors and Associated Equipment*, 741:163–168, 2014.
- [10] A Schiller, L Bergholt, M Guttormsen, E Melby, J Rekstad, and S Siem. Extraction of level density and γ strength function from primary γ spectra. *Nuclear Instruments and Methods in Physics Research Section A: Accelerators, Spectrometers, Detectors and Associated Equipment*, 447(3):498–511, 2000.
- [11] S N Liddick, P F Mantica, R Broda, B A Brown, M P Carpenter, A D Davies, B Fornal, M Horoi, R V F Janssens, A C Morton, W F Mueller, J Pavan, H Schatz, A Stolz, S L Tabor, B E Tomlin, and M Wiedeking. β -decay of odd-A 57 Ti and 59 V. *PHYSICAL REVIEW C*, 72:54321, 2005.
- [12] Aleksandr Y Potekhin. The physics of neutron stars. *Physics-Uspekhi*, 53(12):1235, dec 2010.
- [13] C. Freiburghaus, S. Rosswog, and F.-K. Thielemann. [CLC][ITAL]r[/ITAL][[/CLC]-process in neutron star mergers. *The Astrophysical Journal*, 525(2):L121–L124, November 1999.
- [14] E. Pian, P. D’Avanzo, S. Benetti, M. Branchesi, E. Brocato, S. Campana, E. Cappellaro, S. Covino, V. D’Elia, J. P. U. Fynbo, F. Getman, G. Ghirlanda, G. Ghisellini, A. Grado, G. Greco, J. Hjorth, C. Kouveliotou, A. Levan, L. Limatola, D. Malesani, P. A. Mazzali, A. Melandri, P. Møller, L. Nicastro, E. Palazzi, S. Piranomonte, A. Rossi, O. S. Salafia, J. Selsing, G. Stratta, M. Tanaka, N. R. Tanvir, L. Tomasella, D. Watson, S. Yang, L. Amati, L. A. Antonelli, S. Ascenzi, M. G. Bernardini, M. Boër, F. Bufano, A. Bulgarelli, M. Capaccioli, P. Casella, A. J. Castro-Tirado, E. Chassande-Mottin, R. Ciolfi, C. M. Copperwheat, M. Dadina, G. De Cesare, A. Di Paola, Y. Z. Fan, B. Gendre, G. Giuffrida, A. Giunta, L. K. Hunt, G. L. Israel, Z.-P. Jin, M. M. Kasliwal, S. Klose, M. Lisi, F. Longo, E. Maiorano, M. Mapelli, N. Masetti, L. Nava, B. Patricelli, D. Perley, A. Pescalli, T. Piran, A. Possenti, L. Pulone, M. Razzano, R. Salvaterra, P. Schipani, M. Spera, A. Stamerra, L. Stella, G. Tagliaferri, V. Testa, E. Troja, M. Turatto, S. D. Vergani, and D. Vergani. Spectroscopic identification of r-process nucleosynthesis in a double neutron-star merger. *Nature*, 551(7678):67–70, October 2017.

- [15] B.P. Abbott, R. Abbott, T.D. Abbott, F. Acernese, K. Ackley, C. Adams, T. Adams, P. Addesso, R.X. Adhikari, V.B. Adya, C. Affeldt, M. Afrough, B. Agarwal, M. Agathos, K. Agatsuma, N. Aggarwal, O.D. Aguiar, L. Aiello, A. Ain, P. Ajith, B. Allen, G. Allen, A. Allocca, P.A. Altin, A. Amato, A. Ananyeva, S.B. Anderson, W.G. Anderson, S.V. Angelova, S. Antier, S. Appert, K. Arai, M.C. Araya, J.S. Areeda, N. Arnaud, K.G. Arun, S. Ascenzi, G. Ashton, M. Ast, S.M. Aston, P. Astone, D.V. Atallah, P. Aufmuth, C. Aulbert, K. AultONeal, C. Austin, A. Avila-Alvarez, S. Babak, P. Bacon, M.K.M. Bader, S. Bae, M. Bailes, P.T. Baker, F. Baldaccini, G. Ballardín, S.W. Ballmer, S. Banagiri, J.C. Barayoga, S.E. Barclay, B.C. Barish, D. Barker, K. Barkett, F. Barone, B. Barr, L. Barsotti, M. Barsuglia, D. Barta, S.D. Barthelmy, J. Bartlett, I. Bartos, R. Bassiri, A. Basti, J.C. Batch, M. Bawaj, J.C. Bayley, M. Bazzan, B. Bécsy, C. Beer, M. Bejger, I. Belahcene, A.S. Bell, B.K. Berger, G. Bergmann, S. Bernuzzi, J.J. Bero, C.P.L. Berry, D. Bersanetti, A. Bertolini, J. Betzwieser, S. Bhagwat, R. Bhandare, I.A. Bilenko, G. Billingsley, C.R. Billman, J. Birch, R. Birney, O. Birnholtz, S. Biscans, S. Biscoveanu, A. Bisht, M. Bitossi, C. Biwer, M.A. Bizouard, J.K. Blackburn, J. Blackman, C.D. Blair, D.G. Blair, R.M. Blair, S. Bloemen, O. Bock, N. Bode, M. Boer, G. Bogaert, A. Bohe, F. Bondu, E. Bonilla, R. Bonnand, B.A. Boom, R. Bork, V. Boschi, S. Bose, K. Bossie, Y. Bouffanais, A. Bozzi, C. Bradaschia, P.R. Brady, M. Branchesi, J.E. Brau, T. Briant, A. Brilliet, M. Brinkmann, V. Brisson, P. Brockill, J.E. Broida, A.F. Brooks, D.A. Brown, D.D. Brown, S. Brunett, C.C. Buchanan, A. Buikema, T. Bulik, H.J. Bulten, A. Buonanno, D. Buskulic, C. Buy, R.L. Byer, M. Cabero, L. Cadonati, G. Cagnoli, C. Cahillane, J. Calderón Bustillo, T.A. Callister, E. Calloni, J.B. Camp, M. Canepa, P. Canizares, K.C. Cannon, H. Cao, J. Cao, C.D. Capano, E. Capocasa, F. Carbognani, S. Caride, M.F. Carney, G. Carullo, J. Casanueva Diaz, C. Casentini, S. Caudill, M. Cavaglià, F. Cavalier, R. Cavalieri, G. Cella, C.B. Cepeda, P. Cerdá-Durán, G. Cerretani, E. Cesarini, S.J. Chamberlin, M. Chan, S. Chao, P. Charlton, E. Chase, E. Chassande-Mottin, D. Chatterjee, K. Chatziioannou, B.D. Cheeseboro, H.Y. Chen, X. Chen, Y. Chen, H.-P. Cheng, H. Chia, A. Chincarini, A. Chiummo, T. Chmiel, H.S. Cho, M. Cho, J.H. Chow, N. Christensen, Q. Chu, A.J.K. Chua, S. Chua, A.K.W. Chung, S. Chung, G. Ciani, R. Ciolfi, C.E. Cirelli, A. Cirone, F. Clara, J.A. Clark, P. Clearwater, F. Cleva, C. Cocchieri, E. Coccia, P.-F. Cohadon, D. Cohen, A. Colla, C.G. Collette, L.R. Cominsky, M. Constancio, L. Conti, S.J. Cooper, P. Corban, T.R. Corbitt, I. Cordero-Carrión, K.R. Corley, N. Cornish, A. Corsi, S. Cortese, C.A. Costa, M.W. Coughlin, S.B. Coughlin, J.-P. Coulon, S.T. Countryman, P. Couvares, P.B. Covas, E.E. Cowan, D.M. Coward, M.J. Cowart, D.C. Coyne, R. Coyne, J.D.E. Creighton, T.D. Creighton, J. Cripe, S.G. Crowder, T.J. Cullen, A. Cumming, L. Cunningham, E. Cuoco, T. Dal Canton, G. Dálya, S.L. Danilishin, S. D'Antonio, K. Danzmann, A. Dasgupta, C.F. Da Silva Costa, V. Dattilo, I. Dave, M. Davier, D. Davis, E.J. Daw, B. Day, S. De, D. DeBra, J. Degallaix, M. De Laurentis, S. Deléglise, W. Del Pozzo, N. Demos, T. Denker, T. Dent, R. De Pietri, V. Dergachev, R. De Rosa, R. T. DeRosa, C. De Rossi, R. DeSalvo, O. de Varona, J. Devenson, S. Dhurandhar, M.C. Díaz, T. Dietrich, L. Di Fiore, M. Di Giovanni, T. Di Girolamo, A. Di Lieto, S. Di Pace, I. Di Palma, F. Di Renzo, Z. Doctor, V. Dolique, F. Donovan, K. L. Dooley, S. Doravari, I. Dorrington, R. Douglas, M. Dovale Álvarez, T.P. Downes,

M. Drago, C. Dreissigacker, J. C. Driggers, Z. Du, M. Ducrot, R. Dudi, P. Dupej, S. E. Dwyer, T. B. Edo, M. C. Edwards, A. Effler, H.-B. Eggenstein, P. Ehrens, J. Eichholz, S. S. Eikenberry, R. A. Eisenstein, R. C. Essick, D. Estevez, Z. B. Etienne, T. Etzel, M. Evans, T. M. Evans, M. Factourovich, V. Fafone, H. Fair, S. Fairhurst, X. Fan, S. Farinon, B. Farr, W. M. Farr, E. J. Fauchon-Jones, M. Favata, M. Fays, C. Fee, H. Fehrmann, J. Feicht, M. M. Fejer, A. Fernandez-Galiana, I. Ferrante, E. C. Ferreira, F. Ferrini, F. Fidecaro, D. Finstad, I. Fiori, D. Fiorucci, M. Fishbach, R. P. Fisher, M. Fitz-Axen, R. Flamini, M. Fletcher, H. Fong, J. A. Font, P. W. F. Forsyth, S. S. Forsyth, J.-D. Fournier, S. Frasca, F. Frasconi, Z. Frei, A. Freise, R. Frey, V. Frey, E. M. Fries, P. Fritschel, V. V. Frolov, P. Fulda, M. Fyffe, H. Gabbard, B. U. Gadre, S. M. Gaebel, J. R. Gair, L. Gammaitoni, M. R. Ganija, S. G. Gaonkar, C. Garcia-Quiros, F. Garufi, B. Gateley, S. Gaudio, G. Gaur, V. Gayathri, N. Gehrels, G. Gemme, E. Genin, A. Gennai, D. George, J. George, L. Gergely, V. Germain, S. Ghonge, Abhirup Ghosh, Archisman Ghosh, S. Ghosh, J. A. Giaime, K. D. Giardino, A. Giazotto, K. Gill, L. Glover, E. Goetz, R. Goetz, S. Gomes, B. Goncharov, G. González, J. M. Gonzalez Castro, A. Gopakumar, M. L. Gorodetsky, S. E. Gossan, M. Gosselin, R. Gouaty, A. Grado, C. Graef, M. Granata, A. Grant, S. Gras, C. Gray, G. Greco, A. C. Green, E. M. Gretarsson, P. Groot, H. Grote, S. Grunewald, P. Gruning, G. M. Guidi, X. Guo, A. Gupta, M. K. Gupta, K. E. Gushwa, E. K. Gustafson, R. Gustafson, O. Halim, B. R. Hall, E. D. Hall, E. Z. Hamilton, G. Hammond, M. Haney, M. M. Hanke, J. Hanks, C. Hanna, M. D. Hannam, O. A. Hannuksela, J. Hanson, T. Hardwick, J. Harms, G. M. Harry, I. W. Harry, M. J. Hart, C.-J. Haster, K. Haughian, J. Healy, A. Heidmann, M. C. Heintze, H. Heitmann, P. Hello, G. Hemming, M. Hendry, I. S. Heng, J. Hennig, A. W. Heptonstall, M. Heurs, S. Hild, T. Hinderer, W. C. G. Ho, D. Hoak, D. Hoffman, K. Holt, D. E. Holz, P. Hopkins, C. Horst, J. Hough, E. A. Houston, E. J. Howell, A. Hreibi, Y. M. Hu, E. A. Huerta, D. Huet, B. Hughey, S. Husa, S. H. Huttner, T. Huynh-Dinh, N. Indik, R. Inta, G. Intini, H. N. Isa, J.-M. Isac, M. Isi, B. R. Iyer, K. Izumi, T. Jacqmin, K. Jani, P. Jaranowski, S. Jawahar, F. Jiménez-Forteza, W. W. Johnson, N. K. Johnson-McDaniel, D. I. Jones, R. Jones, R. J. G. Jonker, L. Ju, J. Junker, C. V. Kalaghatgi, V. Kalogera, B. Kamai, S. Kandhasamy, G. Kang, J. B. Kanner, S. J. Kapadia, S. Karki, K. S. Karvinen, M. Kasprzack, W. Kastaun, M. Katolik, E. Katsavounidis, W. Katzman, S. Kaufer, K. Kawabe, F. Kéfélian, D. Keitel, A. J. Kemball, R. Kennedy, C. Kent, J. S. Key, F. Y. Khalili, I. Khan, S. Khan, Z. Khan, E. A. Khazanov, N. Kijbunchoo, Chunglee Kim, J. C. Kim, K. Kim, W. Kim, W. S. Kim, Y.-M. Kim, S. J. Kimbrell, E. J. King, P. J. King, M. Kinley-Hanlon, R. Kirchhoff, J. S. Kissel, L. Kleybolte, S. Klimentko, T. D. Knowles, P. Koch, S. M. Koehlenbeck, S. Koley, V. Kondrashov, A. Kontos, M. Korobko, W. Z. Korth, I. Kowalska, D. B. Kozak, C. Krämer, V. Kringel, B. Krishnan, A. Królak, G. Kuehn, P. Kumar, R. Kumar, S. Kumar, L. Kuo, A. Kutynia, S. Kwang, B. D. Lackey, K. H. Lai, M. Landry, R. N. Lang, J. Lange, B. Lantz, R. K. Lanza, S. L. Larson, A. Lartaux-Vollard, P. D. Lasky, M. Laxen, A. Lazzarini, C. Lazzaro, P. Leaci, S. Leavey, C. H. Lee, H. K. Lee, H. M. Lee, H. W. Lee, K. Lee, J. Lehmann, A. Lenon, E. Leon, M. Leonardi, N. Leroy, N. Letendre, Y. Levin, T. G. F. Li, S. D. Linker, T. B. Littenberg, J. Liu, X. Liu, R. K. L. Lo, N. A. Lockerbie, L. T. London, J. E. Lord, M. Lorenzini, V. Lorette, M. Lormand, G. Losurdo, J. D. Lough, C. O. Lousto, G. Lovelace, H. Lück, D. Lumaca, A. P. Lundgren, R. Lynch,

Y. Ma, R. Macas, S. Macfoy, B. Machenschalk, M. MacInnis, D. M. Macleod, I. Magaña Hernandez, F. Magaña-Sandoval, L. Magaña Zertuche, R. M. Magee, E. Majorana, I. Maksimovic, N. Man, V. Mandic, V. Mangano, G. L. Mansell, M. Manske, M. Mantovani, F. Marchesoni, F. Marion, S. Márka, Z. Márka, C. Markakis, A. S. Markosyan, A. Markowitz, E. Maros, A. Marquina, P. Marsh, F. Martelli, L. Martellini, I. W. Martin, R. M. Martin, D. V. Martynov, J. N. Marx, K. Mason, E. Massera, A. Masserot, T. J. Massinger, M. Masso-Reid, S. Mastrogiovanni, A. Matas, F. Matichard, L. Matone, N. Mavalvala, N. Mazumder, R. McCarthy, D. E. McClelland, S. McCormick, L. McCuller, S. C. McGuire, G. McIntyre, J. McIver, D. J. McManus, L. McNeill, T. McRae, S. T. McWilliams, D. Meacher, G. D. Meadors, M. Mehmet, J. Meidam, E. Mejuto-Villa, A. Melatos, G. Mendell, R. A. Mercer, E. L. Merilh, M. Merzougui, S. Meshkov, C. Messenger, C. Messick, R. Metzдорff, P. M. Meyers, H. Miao, C. Michel, H. Middleton, E. E. Mikhailov, L. Milano, A. L. Miller, B. B. Miller, J. Miller, M. Millhouse, M. C. Milovich-Goff, O. Minazzoli, Y. Minenkov, J. Ming, C. Mishra, S. Mitra, V. P. Mitrofanov, G. Mitselmakher, R. Mittleman, D. Moffa, A. Moggi, K. Mogushi, M. Mohan, S. R. P. Mohapatra, I. Molina, M. Montani, C. J. Moore, D. Moraru, G. Moreno, S. Morisaki, S. R. Morriss, B. Mours, C. M. Mow-Lowry, G. Mueller, A. W. Muir, Arunava Mukherjee, D. Mukherjee, S. Mukherjee, N. Mukund, A. Mullavey, J. Munch, E. A. Muñoz, M. Muratore, P. G. Murray, A. Nagar, K. Napier, I. Nardecchia, L. Naticchioni, R. K. Nayak, J. Neilson, G. Nelemans, T. J. N. Nelson, M. Nery, A. Neunzert, L. Nevin, J. M. Newport, G. Newton, K. K. Y. Ng, P. Nguyen, T. T. Nguyen, D. Nichols, A. B. Nielsen, S. Nissanke, A. Nitz, A. Noack, F. Nocera, D. Nolting, C. North, L. K. Nuttall, J. Oberling, G. D. O’Dea, G. H. Ogin, J. J. Oh, S. H. Oh, F. Ohme, M. A. Okada, M. Oliver, P. Oppermann, Richard J. Oram, B. O’Reilly, R. Ormiston, L. F. Ortega, R. O’Shaughnessy, S. Ossokine, D. J. Ottaway, H. Overmier, B. J. Owen, A. E. Pace, J. Page, M. A. Page, A. Pai, S. A. Pai, J. R. Palamos, O. Palashov, C. Palomba, A. Pal-Singh, Howard Pan, Huang-Wei Pan, B. Pang, P. T. H. Pang, C. Pankow, F. Pannarale, B. C. Pant, F. Paoletti, A. Paoli, M. A. Papa, A. Parida, W. Parker, D. Pascucci, A. Pasqualetti, R. Passaquieti, D. Passuello, M. Patil, B. Patricelli, B. L. Pearlstone, M. Pedraza, R. Pedurand, L. Pekowsky, A. Pele, S. Penn, C. J. Perez, A. Perreca, L. M. Perri, H. P. Pfeiffer, M. Phelps, O. J. Piccinni, M. Pichot, F. Piergiovanni, V. Pierro, G. Pillant, L. Pinard, I. M. Pinto, M. Pirello, M. Pitkin, M. Poe, R. Poggiani, P. Popolizio, E. K. Porter, A. Post, J. Powell, J. Prasad, J. W. W. Pratt, G. Pratten, V. Predoi, T. Prestegard, M. Prijatelj, M. Principe, S. Privitera, R. Prix, G. A. Prodi, L. G. Prokhorov, O. Puncken, M. Punturo, P. Puppo, M. Pürerer, H. Qi, V. Quetschke, E. A. Quintero, R. Quitzow-James, F. J. Raab, D. S. Rabeling, H. Radkins, P. Raffai, S. Raja, C. Rajan, B. Rajbhandari, M. Rakhmanov, K. E. Ramirez, A. Ramos-Buades, P. Rapagnani, V. Raymond, M. Razzano, J. Read, T. Regimbau, L. Rei, S. Reid, D. H. Reitze, W. Ren, S. D. Reyes, F. Ricci, P. M. Ricker, S. Rieger, K. Riles, M. Rizzo, N. A. Robertson, R. Robie, F. Robinet, A. Rocchi, L. Rolland, J. G. Rollins, V. J. Roma, J. D. Romano, R. Romano, C. L. Romel, J. H. Romie, D. Rosińska, M. P. Ross, S. Rowan, A. Rüdiger, P. Ruggi, G. Rutins, K. Ryan, S. Sachdev, T. Sadecki, L. Sadeghian, M. Sakellariadou, L. Salconi, M. Saleem, F. Salemi, A. Samajdar, L. Sammut, L. M. Sampson, E. J. Sanchez, L. E. Sanchez, N. Sanchis-Gual, V. Sandberg, J. R. Sanders, B. Sassolas, B. S. Sathyaprakash, P. R. Saulson, O. Sauter, R. L. Savage, A. Sawadsky, P. Schale, M. Scheel, J. Scheuer,

J. Schmidt, P. Schmidt, R. Schnabel, R. M. S. Schofield, A. Schönbeck, E. Schreiber, D. Schuette, B. W. Schulte, B. F. Schutz, S. G. Schwalbe, J. Scott, S. M. Scott, E. Seidel, D. Sellers, A. S. Sengupta, D. Sentenac, V. Sequino, A. Sergeev, D. A. Shaddock, T. J. Shaffer, A. A. Shah, M. S. Shahriar, M. B. Shaner, L. Shao, B. Shapiro, P. Shawhan, A. Sheperd, D. H. Shoemaker, D. M. Shoemaker, K. Siellez, X. Siemens, M. Sieniawska, D. Sigg, A. D. Silva, L. P. Singer, A. Singh, A. Singhal, A. M. Sintes, B. J. J. Slagmolen, B. Smith, J. R. Smith, R. J. E. Smith, S. Somala, E. J. Son, J. A. Sonnenberg, B. Sorazu, F. Sorrentino, T. Souradeep, A. P. Spencer, A. K. Srivastava, K. Staats, A. Staley, M. Steinke, J. Steinlechner, S. Steinlechner, D. Steinmeyer, S. P. Stevenson, R. Stone, D. J. Stops, K. A. Strain, G. Stratta, S. E. Strigin, A. Strunk, R. Sturani, A. L. Stuver, T. Z. Summerscales, L. Sun, S. Sunil, J. Suresh, P. J. Sutton, B. L. Swinkels, M. J. Szczepańczyk, M. Tacca, S. C. Tait, C. Talbot, D. Talukder, D. B. Tanner, M. Tápai, A. Taracchini, J. D. Tasson, J. A. Taylor, R. Taylor, S. V. Tewari, T. Theeg, F. Thies, E. G. Thomas, M. Thomas, P. Thomas, K. A. Thorne, K. S. Thorne, E. Thrane, S. Tiwari, V. Tiwari, K. V. Tokmakov, K. Toland, M. Tonelli, Z. Tornasi, A. Torres-Forné, C. I. Torrie, D. Töyrä, F. Travasso, G. Traylor, J. Trinastic, M. C. Tringali, L. Trozzo, K. W. Tsang, M. Tse, R. Tso, L. Tsukada, D. Tsuna, D. Tuyenbayev, K. Ueno, D. Ugolini, C. S. Unnikrishnan, A. L. Urban, S. A. Usman, H. Vahlbruch, G. Vajente, G. Valdes, M. Vallisneri, N. van Bakel, M. van Beuzekom, J. F. J. van den Brand, C. Van Den Broeck, D. C. Vander-Hyde, L. van der Schaaf, J. V. van Heijningen, A. A. van Veggel, M. Vardaro, V. Varma, S. Vass, M. Vasúth, A. Vecchio, G. Vedovato, J. Veitch, P. J. Veitch, K. Venkateswara, G. Venugopalan, D. Verkindt, F. Vetrano, A. Viceré, A. D. Viets, S. Vinciguerra, D. J. Vine, J.-Y. Vinet, S. Vitale, T. Vo, H. Vocca, C. Vorvick, S. P. Vyatchanin, A. R. Wade, L. E. Wade, M. Wade, R. Walet, M. Walker, L. Wallace, S. Walsh, G. Wang, H. Wang, J. Z. Wang, W. H. Wang, Y. F. Wang, R. L. Ward, J. Warner, M. Was, J. Watchi, B. Weaver, L.-W. Wei, M. Weinert, A. J. Weinstein, R. Weiss, L. Wen, E. K. Wessel, P. Weßels, J. Westerweck, T. Westphal, K. Wette, J. T. Whelan, S. E. Whitcomb, B. F. Whiting, C. Whittle, D. Wilken, D. Williams, R. D. Williams, A. R. Williamson, J. L. Willis, B. Willke, M. H. Wimmer, W. Winkler, C. C. Wipf, H. Wittel, G. Woan, J. Woehler, J. Wofford, K. W. K. Wong, J. Worden, J. L. Wright, D. S. Wu, D. M. Wysocki, S. Xiao, H. Yamamoto, C. C. Yancey, L. Yang, M. J. Yap, M. Yazback, Hang Yu, Haocun Yu, M. Yvert, A. Zadrożny, M. Zanolin, T. Zelenova, J.-P. Zendri, M. Zevin, L. Zhang, M. Zhang, T. Zhang, Y.-H. Zhang, C. Zhao, M. Zhou, Z. Zhou, S. J. Zhu, X. J. Zhu, A. B. Zimmerman, M. E. Zucker, and J. Zweizig and. GW170817: Observation of gravitational waves from a binary neutron star inspiral. *Physical Review Letters*, 119(16), October 2017.

- [16] A. Parikh, J. José, G. Sala, and C. Iliadis. Nucleosynthesis in type i X-ray bursts. *Progress in Particle and Nuclear Physics*, 69(1):225–253, 2013. Publisher: Elsevier B.V.
- [17] Edward F. Brown and Lars Bildsten. The ocean and crust of a rapidly accreting neutron star: Implications for magnetic field evolution and thermonuclear flashes. *The Astrophysical Journal*, 496(2):915–933, April 1998.

- [18] A. Turlione, D. N. Aguilera, and J. A. Pons. Quiescent thermal emission from neutron stars in low-mass X-ray binaries. *Astronomy & Astrophysics*, 577:A5, May 2015.
- [19] H. Schatz, S. Gupta, P. Möller, M. Beard, E. F. Brown, A. T. Deibel, L. R. Gasques, W. R. Hix, L. Keek, R. Lau, A. W. Steiner, and M. Wiescher. Strong neutrino cooling by cycles of electron capture and β -decay in neutron star crusts. *Nature* 2013 505:7481, 505(7481):62–65, December 2013. Publisher: Nature Publishing Group.
- [20] Tod E. Strohmayer and Edward F. Brown. A remarkable 3 hour thermonuclear burst from 4u 1820–30. *The Astrophysical Journal*, 566(2):1045, feb 2002.
- [21] F. Haberl, L. Stella, N. E. White, M. Gottwald, and W. C. Priedhorsky. EXOSAT observations of double-peaked bursts with radius expansion from 4u/MXB 1820-30. *The Astrophysical Journal*, 314:266, March 1987.
- [22] JJM In’t Zand, E Kuulkers, F Verbunt, J Heise, and R Cornelisse. A superburst from 4u 1254-69. *Astronomy and astrophysics*, 411(3):L487–L491, 2003.
- [23] Alex Deibel, Zach Meisel, Hendrik Schatz, Edward F. Brown, and Andrew Cumming. URCA COOLING PAIRS IN THE NEUTRON STAR OCEAN AND THEIR EFFECT ON SUPERBURSTS. *The Astrophysical Journal*, 831(1):13, October 2016.
- [24] G. J. Neary. The β -ray spectrum of radium e. *Proceedings of the Royal Society of London. Series A. Mathematical and Physical Sciences*, 175(960):71–87, March 1940.
- [25] R. Lau, M. Beard, S. S. Gupta, H. Schatz, A. V. Afanasjev, E. F. Brown, A. Deibel, L. R. Gasques, G. W. Hitt, W. R. Hix, L. Keek, P. Möller, P. S. Shternin, A. W. Steiner, M. Wiescher, and Y. Xu. Nuclear reactions in the crusts of accreting neutron stars. *The Astrophysical Journal*, 859(1):62, May 2018.
- [26] W.-J Ong, E F Brown, J Browne, S Ahn, K Childers, B P Crider, A C Dombos, S S Gupta, G W Hitt, C Langer, R Lewis, S N Liddick, S Lyons, Z Meisel, P Möller, F Montes, F Naqvi, J Pereira, C Prokop, D Richman, H Schatz, K Schmidt, and A Spyrou. β decay of ^{61}v and its role in cooling accreted neutron star crusts. *Physical Review Letters*, 125, 2020.
- [27] K Langanke, G Martínez-Pinedo, and R G T Zegers. Electron capture in stars. *Reports on Progress in Physics*, 84(6):066301, May 2021.
- [28] L Gaudefroy, O Sorlin, C Donzaud, J C Angélique, F Azaiez, C Bourgeois, V Chiste, Z Dlouhy, S Grévy, D Guillemaud-Mueller, F Ibrahim, K.-L Kratz, M Lewitowicz, S M Lukyanov, I Matea, J Mrasek, F Nowacki, F De, Oliveira Santos, Yu.-E Penionzhkevich, B Pfeiffer, F Pougheon, M G Saint-Laurent, and M Stanoiu. Beta-decay studies of neutron-rich sc-cr nuclei. *Eur. Phys. J. A*, 23:41–48, 2005.

- [29] J. M. Daugas, I. Matea, J.-P. Delaroche, M. Pfützner, M. Sawicka, F. Becker, G. Bélier, C. R. Bingham, R. Borcea, E. Bouchez, A. Buta, E. Dragulescu, G. Georgiev, J. Giovannazzo, M. Girod, H. Grawe, R. Grzywacz, F. Hammache, F. Ibrahim, M. Lewitowicz, J. Libert, P. Mayet, V. Méot, F. Negoita, F. De Oliveira Santos, O. Perru, O. Roig, K. Rykaczewski, M. G. Saint-Laurent, J. E. Sauvestre, O. Sorlin, M. Stanoiu, I. Stefan, Ch. Stodel, Ch. Theisen, D. Verney, and J. Żylicz. β -decay measurements for $N > 40$ Mn nuclei and inference of collectivity for neutron-rich Fe isotopes. *Physical Review C*, 83(5):054312, May 2011.
- [30] K. Wimmer, F. Recchia, S. M. Lenzi, S. Riccetto, T. Davinson, A. Estrade, C. J. Griffin, S. Nishimura, F. Nowacki, V. Phong, A. Poves, P. A. Söderström, O. Aktas, M. Al-Aqeel, T. Ando, H. Baba, S. Bae, S. Choi, P. Doornenbal, J. Ha, L. Harkness-Brennan, T. Isobe, P. R. John, D. Kahl, G. Kiss, I. Kojouharov, N. Kurz, M. Labiche, K. Matsui, S. Momiyama, D. R. Napoli, M. Niikura, C. Nita, Y. Saito, H. Sakurai, H. Schaffner, P. Schrock, C. Stahl, T. Sumikama, V. Werner, W. Witt, and P. J. Woods. First spectroscopy of ^{61}Ti and the transition to the island of inversion at $n = 40$. *Physics Letters, Section B: Nuclear, Elementary Particle and High-Energy Physics*, 792:16–20, 5 2019.
- [31] J. C. Hardy, L. C. Carraz, B. Jonson, and P. G. Hansen. The essential decay of pandemonium: A demonstration of errors in complex beta-decay schemes. *Physics Letters B*, 71:307–310, 11 1977.
- [32] Meng Wang, G. Audi, F. G. Kondev, W.J. Huang, S. Naimi, and Xing Xu. The AME2016 atomic mass evaluation (II). tables, graphs and references. *Chinese Physics C*, 41(3):030003, March 2017.
- [33] J.I. Prisciandaro, A.C. Morton, and P.F. Mantica. Beta counting system for fast fragmentation beams. *Nuclear Instruments and Methods in Physics Research Section A: Accelerators, Spectrometers, Detectors and Associated Equipment*, 505(1):140–143, 2003. Proceedings of the tenth Symposium on Radiation Measurements and Applications.
- [34] O.B. Tarasov and D. Bazin. Lise++: Exotic beam production with fragment separators and their design. *Nuclear Instruments and Methods in Physics Research Section B: Beam Interactions with Materials and Atoms*, 376:185–187, 2016. Proceedings of the XVIIth International Conference on Electromagnetic Isotope Separators and Related Topics (EMIS2015), Grand Rapids, MI, U.S.A., 11-15 May 2015.
- [35] Hans A Bethe, Julius Ashkin, et al. Experimental nuclear physics. *Wiley, New York*, 1953.
- [36] K.-H. Schmidt, E. Hanelt, H. Geissel, G. Münzenberg, and J.P. Dufour. The momentum-loss achromat — a new method for the isotopical separation of relativistic heavy ions. *Nuclear Instruments and Methods in Physics Research Section A: Accelerators, Spectrometers, Detectors and Associated Equipment*, 260(2):287–303, 1987.

- [37] Fred S Goulding and Bernard G Harvey. Identification of nuclear particles. *Annual Review of Nuclear Science*, 25(1):167–240, 1975.
- [38] J. Pereira, S. Hennrich, A. Aprahamian, O. Arndt, A. Becerril, T. Elliot, A. Estrade, D. Galaviz, R. Kessler, K.-L. Kratz, G. Lorusso, P. F. Mantica, M. Matos, P. Möller, F. Montes, B. Pfeiffer, H. Schatz, F. Schertz, L. Schnorrenberger, E. Smith, A. Stolz, M. Quinn, W. B. Walters, and A. Wöhr. β -decay half-lives and β -delayed neutron emission probabilities of nuclei in the region $a \lesssim 110$, relevant for the r process. *Phys. Rev. C*, 79:035806, Mar 2009.
- [39] K-L Kratz, W Rudolph, H Ohm, H Franz, M Zendel, G Herrmann, SG Prussin, FM Nuh, AA Shihab-Eldin, DR Slaughter, et al. Investigation of beta strength functions by neutron and gamma-ray spectroscopy:(i). the decay of 87br, 137i, 85as and 135sb. *Nuclear Physics A*, 317(2-3):335–362, 1979.
- [40] K L Kratz, A Schröder, H Ohm, M Zendel, H Gabelmann, W Ziegert, P Peuser, G Jung, B Pfeiffer, KD Wünsch, et al. Beta-delayed neutron emission from 93–100 rb to excited states in the residual sr isotopes. *Zeitschrift für Physik A Atoms and Nuclei*, 306:239–257, 1982.
- [41] Alexander C. Dombos. *β -Decay Total Absorption Spectroscopy around $A = 100$ -110 Relevant to Nuclear Structure and the Astrophysical r Process*. PhD thesis, Michigan State University, 2018. Copyright - Database copyright ProQuest LLC; ProQuest does not claim copyright in the individual underlying works; Last updated - 2022-11-03.
- [42] K. Starosta, C. Vaman, D. Miller, P. Voss, D. Bazin, T. Glasmacher, H. Crawford, P. Mantica, H. Tan, W. Hennig, M. Walby, A. Fallu-Labruyere, J. Harris, D. Breus, P. Grudberg, and W.K. Warburton. Digital data acquisition system for experiments with segmented detectors at national superconducting cyclotron laboratory. *Nuclear Instruments and Methods in Physics Research Section A: Accelerators, Spectrometers, Detectors and Associated Equipment*, 610(3):700–709, 2009.
- [43] GEANT Collaboration, S Agostinelli, et al. Geant4—a simulation toolkit. *Nucl. Instrum. Meth. A*, 506(25):0, 2003.
- [44] M. Karny, K.P. Rykaczewski, A. Fijałkowska, B.C. Rasco, M. Wolińska-Cichočka, R.K. Grzywacz, K.C. Goetz, D. Miller, and E.F. Zganjar. Modular total absorption spectrometer. *Nuclear Instruments and Methods in Physics Research Section A: Accelerators, Spectrometers, Detectors and Associated Equipment*, 836:83–90, 2016.
- [45] Artemis Spyrou. Personal conversation, November 2022.
- [46] G. A. Bartholomew, E. D. Earle, A. J. Ferguson, J. W. Knowles, and M. A. Lone. Gamma-ray strength functions. In *Advances in Nuclear Physics*, pages 229–324. Springer US, 1973.

- [47] L. E. Kirsch and L. A. Bernstein. Rainier: A simulation tool for distributions of excited nuclear states and cascade fluctuations. *Nuclear Instruments and Methods in Physics Research, Section A: Accelerators, Spectrometers, Detectors and Associated Equipment*, 892:30–40, 6 2018.
- [48] Arjan J Koning, Stephane Hilaire, and Marieke C Duijvestijn. Talys-1.0. In *International Conference on Nuclear Data for Science and Technology*, pages 211–214. EDP Sciences, 2007.
- [49] A. Voinov, E. Algin, U. Agvaanluvsan, T. Belgya, R. Chankova, M. Guttormsen, G. E. Mitchell, J. Rekestad, A. Schiller, and S. Siem. Large enhancement of radiative strength for soft transitions in the quasicontinuum. *Phys. Rev. Lett.*, 93:142504, Sep 2004.
- [50] S. Goriely, S. Hilaire, S. Péru, and K. Sieja. Gogny-hfb+qrpa dipole strength function and its application to radiative nucleon capture cross section. *Phys. Rev. C*, 98:014327, Jul 2018.
- [51] A. Spyrou, S. N. Liddick, A. C. Larsen, M. Guttormsen, K. Cooper, A. C. Dombos, D. J. Morrissey, F. Naqvi, G. Perdikakis, S. J. Quinn, T. Renstrøm, J. A. Rodriguez, A. Simon, C. S. Sumithrarachchi, and R. G. T. Zegers. Novel technique for Constraining r -Process (n, γ) Reaction Rates. *Physical Review Letters*, 113(23):232502, December 2014.
- [52] Qingfu Zhang and Hui Li. Moea/d: A multiobjective evolutionary algorithm based on decomposition. *IEEE Transactions on Evolutionary Computation*, 11(6):712–731, 2007.
- [53] A.K. Pandey, R.C. Sharma, P.C. Kalsi, and R.H. Iyer. Measurement of alpha to fission branching ratios of heavy actinides by sequential etching of alpha and fission tracks in cr-39. *Nuclear Instruments and Methods in Physics Research Section B: Beam Interactions with Materials and Atoms*, 82(1):151–155, 1993.
- [54] Y.A. AKOVALI. Nuclear data sheets for $a = 250, 254, 258, 262, 266$. *Nuclear Data Sheets*, 94(1):131–225, 2001.
- [55] J. Pereira, P. Hosmer, G. Lorusso, P. Santi, A. Couture, J. Daly, M. Del Santo, T. Elliot, J. Görres, C. Herlitzius, K.-L. Kratz, L.O. Lamm, H.Y. Lee, F. Montes, M. Ouellette, E. Pellegrini, P. Reeder, H. Schatz, F. Schertz, L. Schnorrenberger, K. Smith, E. Stech, E. Strandberg, C. Ugalde, M. Wiescher, and A. Wöhr. The neutron long counter NERO for studies of neutron emission in the r -process. *Nuclear Instruments and Methods in Physics Research Section A: Accelerators, Spectrometers, Detectors and Associated Equipment*, 618(1-3):275–283, June 2010.
- [56] J.D. King, N. Neff, and H.W. Taylor. The energy of the 40k gamma ray and its use as a calibration standard. *Nuclear Instruments and Methods*, 52(2):349–350, 1967.

- [57] H. BATEMAN. The solution of a system of differential equations occurring in the theory of radioactive transformations. *Proc. Cambridge Philos. Soc.*, 15:423–427, 1910.
- [58] Jerzy Cetnar. General solution of bateman equations for nuclear transmutations. *Annals of Nuclear Energy*, 33(7):640–645, 2006.
- [59] T. Kurtukian-Nieto, J. Benlliure, and K.-H. Schmidt. A new analysis method to determine β -decay half-lives in experiments with complex background. *Nuclear Instruments and Methods in Physics Research Section A: Accelerators, Spectrometers, Detectors and Associated Equipment*, 589(3):472–483, 2008.
- [60] O. Sorlin, C. Donzaud, F. Azaiez, C. Bourgeois, L. Gaudefroy, F. Ibrahim, D. Guillemaud-Mueller, F. Pougheon, M. Lewitowicz, F. de Oliveira Santos, M. G. Saint-Laurent, M. Stanoiu, S. M. Lukyanov, Yu E. Penionzhkevich, J. C. Angélique, S. Grévy, K. L. Kratz, B. Pfeiffer, F. Nowacki, Z. Dlouhy, and J. Mrasek. Beta decay studies of neutron-rich 21sc-27co nuclei at ganil. *Nuclear Physics A*, 719:C193–C200, 5 2003.
- [61] P. F. Mantica, B. A. Brown, A. D. Davies, T. Glasmacher, D. E. Groh, M. Horoi, S. N. Liddick, D. J. Morrissey, A. C. Morton, W. F. Mueller, H. Schatz, A. Stolz, and S. L. Tabor. β -decay properties of $^{55,56}\text{Ti}$. *Phys. Rev. C*, 68:044311, Oct 2003.
- [62] U. Bosch, W.-D. Schmidt-Ott, E. Runte, P. Tidemand-Petersson, P. Koschel, F. Meissner, R. Kirchner, O. Klepper, E. Roeckl, K. Rykaczewski, and D. Schardt. Beta- and gamma-decay studies of neutron-rich chromium, manganese, cobalt and nickel isotopes including the new isotopes 60cr and 60gmn. *Nuclear Physics A*, 477(1):89–104, 1988.
- [63] S. N. Liddick, P. F. Mantica, B. A. Brown, M. P. Carpenter, A. D. Davies, M. Horoi, R. V. F. Janssens, A. C. Morton, W. F. Mueller, J. Pavan, H. Schatz, A. Stolz, S. L. Tabor, B. E. Tomlin, and M. Wiedeking. Half-life and spin of $^{60}\text{mn}^g$. *Phys. Rev. C*, 73:044322, Apr 2006.
- [64] A. M. Nathan, D. E. Alburger, J. W. Olness, and E. K. Warburton. Beta decay of $^{54-55}\text{V}$ and the mass of ^{55}V . *Phys. Rev. C*, 16:1566–1575, Oct 1977.
- [65] H. L. Crawford, P. F. Mantica, J. S. Berryman, R. Broda, B. Fornal, C. R. Hoffman, N. Hoteling, R. V. F. Janssens, S. M. Lenzi, J. Pereira, J. B. Stoker, S. L. Tabor, W. B. Walters, X. Wang, and S. Zhu. Low-energy structure of ^{61}Mn populated following β decay of ^{61}Cr . *Phys. Rev. C*, 79:054320, May 2009.
- [66] P. F. Mantica, A. C. Morton, B. A. Brown, A. D. Davies, T. Glasmacher, D. E. Groh, S. N. Liddick, D. J. Morrissey, W. F. Mueller, H. Schatz, A. Stolz, S. L. Tabor, M. Honma, M. Horoi, and T. Otsuka. β decay studies of the neutron-rich $^{56-58}\text{V}$ isotopes. *Phys. Rev. C*, 67:014311, Jan 2003.

- [67] M. Oinonen, U. Köster, J. Äystö, V. Fedoseyev, V. Mishin, J. Huikari, A. Jokinen, A. Nieminen, K. Peräjärvi, A. Knipper, G. Walter, and the ISOLDE Collaboration. Ground-state spin of ^{59}mn . *The European Physical Journal A - Hadrons and Nuclei*, 10(2):123–127, Apr 2001.
- [68] D. Radulov, C. J. Chiara, I. G. Darby, H. De Witte, J. Diriken, D. V. Fedorov, V. N. Fedosseev, L. M. Fraile, M. Huyse, U. Köster, B. A. Marsh, D. Pauwels, L. Popescu, M. D. Seliverstov, A. M. Sjödin, P. Van den Bergh, P. Van Duppen, M. Venhart, W. B. Walters, and K. Wimmer. β decay of ^{61}mn to levels in ^{61}fe . *Phys. Rev. C*, 88:014307, Jul 2013.
- [69] B.J. Dropesky, A.W. Schardt, and T.T. Shull. Note on the decay of the new nucleide $\text{cr}56$. *Nuclear Physics*, 16(2):357–359, 1960.
- [70] C. N. Davids, D. F. Geesaman, S. L. Tabor, M. J. Murphy, E. B. Norman, and R. C. Pardo. Mass and β decay of the new isotope ^{57}Cr . *Phys. Rev. C*, 17:1815–1821, May 1978.
- [71] R.D. Evans. *The Atomic Nucleus*. International series in pure and applied physics. McGraw-Hill, 1972.
- [72] W.F. Mueller, J.A. Church, T. Glasmacher, D. Gutknecht, G. Hackman, P.G. Hansen, Z. Hu, K.L. Miller, and P. Quirin. Thirty-two-fold segmented germanium detectors to identify γ -rays from intermediate-energy exotic beams. *Nuclear Instruments and Methods in Physics Research Section A: Accelerators, Spectrometers, Detectors and Associated Equipment*, 466(3):492–498, 2001.
- [73] Peter Möller and Jørgen Randrup. New developments in the calculation of β -strength functions. *Nuclear Physics A*, 514(1):1–48, 1990.
- [74] P. Moller, J.R. Nix, W.D. Myers, and W.J. Swiatecki. Nuclear ground-state masses and deformations. *Atomic Data and Nuclear Data Tables*, 59(2):185–381, 1995.
- [75] P. Möller, A.J. Sierk, R. Bengtsson, H. Sagawa, and T. Ichikawa. Nuclear shape isomers. *Atomic Data and Nuclear Data Tables*, 98(2):149–300, 2012.
- [76] P. Möller, A.J. Sierk, T. Ichikawa, and H. Sagawa. Nuclear ground-state masses and deformations: Frdm(2012). *Atomic Data and Nuclear Data Tables*, 109-110:1–204, 2016.
- [77] S. Michimasa, M. Kobayashi, Y. Kiyokawa, S. Ota, R. Yokoyama, D. Nishimura, D. S. Ahn, H. Baba, G. P. A. Berg, M. Dozono, N. Fukuda, T. Furuno, E. Ideguchi, N. Inabe, T. Kawabata, S. Kawase, K. Kisamori, K. Kobayashi, T. Kubo, Y. Kubota, C. S. Lee, M. Matsushita, H. Miya, A. Mizukami, H. Nagakura, H. Oikawa, H. Sakai, Y. Shimizu, A. Stolz, H. Suzuki, M. Takaki, H. Takeda, S. Takeuchi, H. Tokieda, T. Uesaka, K. Yako,

Y. Yamaguchi, Y. Yanagisawa, K. Yoshida, and S. Shimoura. Mapping of a new deformation region around ^{62}Ti . *Phys. Rev. Lett.*, 125:122501, Sep 2020.

- [78] H. L. Crawford, V. Tripathi, J. M. Allmond, B. P. Crider, R. Grzywacz, S. N. Liddick, A. Andalib, E. Argo, C. Benetti, S. Bhattacharya, C. M. Campbell, M. P. Carpenter, J. Chan, A. Chester, J. Christie, B. R. Clark, I. Cox, A. A. Doetsch, J. Dopfer, J. G. Duarte, P. Fallon, A. Frotscher, T. Gaballah, T. J. Gray, J. T. Harke, J. Heideman, H. Heugen, R. Jain, T. T. King, N. Kitamura, K. Kolos, F. G. Kondev, A. Laminack, B. Longfellow, R. S. Lubna, S. Luitel, M. Madurga, R. Mahajan, M. J. Mogannam, C. Morse, S. Neupane, A. Nowicki, T. H. Ogunbeku, W.-J. Ong, C. Porzio, C. J. Prokop, B. C. Rasco, E. K. Ronning, E. Rubino, T. J. Ruland, K. P. Rykaczewski, L. Schaedig, D. Seweryniak, K. Siegl, M. Singh, S. L. Tabor, T. L. Tang, T. Wheeler, J. A. Winger, and Z. Xu. Crossing $n=28$ toward the neutron drip line: First measurement of half-lives at FRIB. *Physical Review Letters*, 129(21), November 2022.